Measurement of the $Z \to \tau_\ell \tau_h$ Cross-section and Search for the Standard Model Vector Boson Fusion Produced Higgs $\to \tau_\ell \tau_h$ at ATLAS

Aimee Larner

Hertford College, Oxford

Thesis submitted in partial fulfilment of the requirements for the degree of

Doctor of Philosophy at the University of Oxford

Michaelmas Term, 2011

Measurement of the $Z \to \tau_\ell \tau_h$ Cross-section and Search for the Standard Model Vector Boson Fusion Produced Higgs $\to \tau_\ell \tau_h$ at ATLAS

Aimee Larner, Hertford College, Oxford

Thesis submitted in partial fulfilment of the requirements for the degree of Doctor of Philosophy at the University of Oxford. Michaelmas Term, 2011

Abstract

This thesis presents a cross-section measurement of the $Z \to \tau_\ell \tau_h$ process performed using the ATLAS detector at the Large Hadron Collider at CERN. The data used were collected at a centre-of-mass energy of 7 TeV during 2010 and corresponds to an integrated luminosity of 36 pb^{-1}. This measurement uses the final state where one τ lepton decays leptonically, to an electron or muon, plus neutrinos, and the other τ lepton decays hadronically. The $\gamma^*/Z \to \ell\ell$, $\bar{t}t$ and di-boson background processes are estimated using Monte Carlo simulation, the $W \to \tau\nu$ Monte Carlo background prediction is estimated using a semi data-driven method. The multijet background is estimated with a fully data-driven 'ABCD' method using three exclusive control regions built by inverting uncorrelated requirements on the isolation of the electron or muon and the product of the electric charge of the identified electron or muon and hadronically decayed τ lepton.

The measured cross-sections in each channel are corrected for the individual branching ratios and yield the total cross-section $\sigma(Z \to \tau\tau, m_{inv}$ 66 - 116 GeV) = 1142 $\pm$ 135.5(stat.) $\pm$ 206.2(syst.) $\pm$ 40.19(lumi.) $\pm$ 3.6(theo.) pb for the electron channel and $\sigma(Z \to \tau\tau, m_{inv}$ 66 - 116 GeV) = 857.6 $\pm$ 81.4(stat.) $\pm$ 132.5(syst.) $\pm$ 30.19(lumi.) $\pm$ 2.8(theo.) pb for the muon channel, where the invariant mass of the Z boson is between 66 and 116 GeV. These are in good agreement with the theoretical prediction of 960 $\pm$ 49.5 pb.

Performing a measurement of a well-known Standard Model process using the ATLAS detector in this new high energy regime is essential for validating the τ lepton identification in particular, which is essential for any new physics search such as $H \to \tau_\ell \tau_h$.

A cut-based analysis for the Vector Boson Fusion produced Higgs boson decaying to two τ leptons channel is introduced and the possibility of using the more complex analysis technique, the Matrix Element method, to increase sensitivity is discussed.

Acknowledgements

I would like to begin by thanking my supervisor Sinead Farrington for her help throughout my PhD, for all the time invested and her patience in helping me to get started and for challenging and supporting me right through to proof-reading this thesis.

I am also grateful to all the researchers and professors in the Oxford High Energy Physics group for the teaching and for providing an intellectually stimulating environment in which to undertake my studies as well as to the secretarial staff and IT support. Particular thanks are extended to Christopher Hays and Elias Coniavitis for their guidance and assistance over the past two years and for many interesting discussions.

I would like to thank my fellow Oxford Particle Physics graduate students not only for answering many questions and helping with coding problems but also for providing stress relief when most needed. In particular thanks go to Gemma Wooden for her patience in sharing her experience with the Matrix Element method with me.

During my PhD I spent a considerable amount of time at CERN and I would like to thank the UK liaison staff at CERN who helped make life much easier. I would like to give mention to all the people I collaborated with at CERN who helped me to integrate into the collaboration and get the most out of studying at a large international laboratory, I have learned a great deal from you all. It is only fair to also thank all my fellow students and friends I met at CERN, too many to mention by name, as you helped make living abroad an enjoyable experience.

I would like to thank the Science and Technologies Facilities Council (STFC) in the UK and the University of Oxford Physics Department for the financial support which has made this work possible.

Finally, last but not least, I thank my whole family for their unwavering support throughout the entire four years.

Contents

Chapter 1

Introduction

The Standard Model was developed to explain the experimental results of subatomic physics experiments. The theory includes three forces, the electromagnetic, weak and strong and describes their interactions with the observed fundamental particles. It has been tested to high degrees of accuracy by a variety of experiments and measurements [1]. However the Standard Model is not complete, one of the questions left unanswered by the Standard Model is how the particles acquire the masses seen in nature. The Higgs mechanism is a possible solution, however the Higgs mechanism gives rise to an additional scalar particle which has not yet been discovered, the elusive Higgs boson.

In March 2010 the Large Hadron Collider (LHC) at CERN produced its first collisions at a centre-of-mass energy of 7 TeV, the world record for the highest energy. The LHC has been surpassing expectations of performance ever since, along with the ATLAS detector, one of the experiments stationed around the LHC ring. One of the primary physics goals of the two general purpose experiments at the LHC, ATLAS and CMS, is to reach an understanding of this mass mechanism, either by discovering the Higgs boson or new physics beyond the Standard Model.

Before the ATLAS detector could be employed to search for new physics it was necessary to ensure the performance was understood and that the reconstructed output matched expectations from Monte Carlo. To this end a wide range of performance studies were undertaken alongside many rediscoveries of Standard Model particles, including the W and Z bosons. This thesis is concerned with the measurement of the cross-section of the $Z \to \tau_\ell \tau_h$ process. To perform this measurement, Monte Carlo simulation was used to estimate the $Z \to \ell\ell$, $\bar{t}t$ and di-boson backgrounds; a semi data-driven method was used to estimate the contribution to the background from the $W \to \ell\nu$ process. To estimate one of the most significant backgrounds to this process,

the multijet background, a data-driven technique was developed. It was thoroughly tested and the systematic uncertainties on this method of background estimation as well as on the Monte Carlo were ascertained. The measured cross-section agreed within uncertainties with the theoretical prediction, as well as with a measurement of the $Z \to \ell\ell$ (where $\ell = e^{\pm}, \mu^{\pm}$) process by the ATLAS experiment and with the CMS measurement of the $Z \to \tau\tau$ cross-section.

At the LHC an important Higgs boson search channel is the Vector Boson Fusion Higgs production mode, with the Higgs boson decaying to a pair of τ leptons, due to the unique signature afforded by Vector Boson Fusion. As the production cross-section is lower for the Vector Boson Fusion mode than the dominant gluon-gluon fusion mode, this analysis has a longer timeline and therefore it is important to consider possible strategies for using a multivariate technique to get the most power from the analysis. In this thesis the work has been completed by the author to introduce the Matrix Element technique and illustrate that the tools are already available which could be used to implement this method in this channel.

The contents of this thesis are laid out with an overview of the Standard Model of Particle Physics in chapter two followed by a description of the LHC and the ATLAS detector in chapter three. Chapter four describes a study of the ATLAS trigger for hadronically decaying τ leptons and its performance in an environment approximating the high luminosity conditions expected at the design luminosity running of the LHC. The event selection of the cross-section of the $Z \to \tau_\ell\tau_h$ process and a description of the data-driven background estimation method are detailed in chapter five, followed by an evaluation of the systematic uncertainties and the calculation and interpretation of the results in chapter six. The full analysis has been included for completeness however the parts worked on by the author include the event selection optimisation, the development of the Same Sign background estimation method and calculation of its systematic uncertainties and the measurement of the electron isolation efficiency. In chapter seven an introduction to a Vector Boson Fusion Higgs analysis is given and the possibility of using a Matrix Element method for a search in this channel is discussed. Finally chapter eight summarises and discusses the results presented in this thesis.

Chapter 2

The Standard Model and the Higgs Boson

2.1 Particle Physics

The Standard Model (SM) of Particle Physics is a relativistic, renormalisable, gauge theory containing all known elementary particles and describing the form of the interactions between them. There are four fundamental forces in nature, the electromagnetic, the weak, the strong and gravity. Of these, the first three have so far been unified into the Standard Model; the fourth, gravity, has not yet been successfully described by a renormalisable quantum field theory and incorporated. At the subatomic scale of the Standard Model the effect of the gravitational force is negligible.

2.1.1 The Particles

The particles in nature fall into two types: fermions and bosons; fermions have half-integer spin (s) and bosons have integer s, the Higgs being $s = 0$. The fermions can be further divided into leptons and quarks, where quarks feel the strong force directly but leptons do not. Both leptons and quarks can be divided into three generations, each mirroring the earlier generations in properties but increasing in mass and decreasing in stability.

Lepton	Mass [MeV]
ν_e	$< 2 \times 10^{-6}$
e	0.511
ν_μ	< 0.19
μ	105.66
ν_τ	< 18.2
τ	1776.82

Table 2.1: Masses of the leptons [1].

Quark Flavour	Mass [MeV]
u	$2.5^{+0.6}_{-0.8}$
d	$5.0^{+0.7}_{-0.9}$
c	$1.29^{+0.05}_{-0.11} \times 10^3$
s	100^{+30}_{-20}
t	$172.9 \pm 0.6 \pm 0.9 \times 10^3$
b	$4.19^{+0.18}_{-0.06} \times 10^3$

Table 2.2: Quark masses [1].

Decay Mode	Branching Fraction Γ_i/Γ
Leptonic:	
$e^-\bar{\nu_e}\nu_\tau$	17.85 ± 0.05 %
$\mu^-\bar{\nu_\mu}\nu_\tau$	17.36 ± 0.05 %
Hadronic:	
$h^\pm + \geq 0\, neutrals$	50.16 ± 0.11 %
$h^\pm h^\mp h^\pm + \geq 0\, neutrals$	14.56 ± 0.08 %
$h^\pm h^\mp h^\pm h^\mp h^\pm + \geq 0\, neutrals$	$1.02 \pm 0.04 \times 10^{-3}$

Table 2.3: Branching fractions of the most common decay categories for the τ lepton [1]. These decays account for more than 99.9 % of the τ lepton decay width. $h^\pm$ represents $\pi^\pm$ or $K^\pm$ and neutrals represents γ's or π^0's.

The leptons consist of single charged particles and electrically neutral neutrinos. There are three generations, each a different flavour, the electron (e), the muon (μ) and the tau lepton (τ) all of electrical charge $(Q) = -1$. Each has a corresponding flavour neutrino, respectively the electron neutrino (ν_e), muon neutrino (ν_μ) and tau neutrino (ν_τ). The masses of the leptons can be found in table 2.1.

As the generations increase in mass, it becomes possible for the leptons to decay. The μ lepton can decay to $e\bar{\nu_e}\nu_\mu$; the additional mass of the τ lepton means it is heavy enough to decay to hadrons, constituted of quarks, as well as the lighter leptons. A summary of the branching fractions of the most common decays of the τ leptons is given in table 2.3.

In the original formulation of the SM, neutrinos were assumed to be massless, however the observation of neutrino oscillations between flavour states indicates that this is not the reality [2, 3]; how to incorporate these neutrino masses is still being determined. In this document the neutrinos will be treated as massless.

Each generation of quarks contains an up-type quark of charge $+\,{}^2/_3$ and a down-type quark of charge $-\,{}^1/_3$, the generations are: up (u) and down (d), charm (c) and strange (s), and top (t) and bottom (b). The quarks do not exist in a free state due to the nature of the strong interactions , discussed further in section 2.1.2. The bound states are called hadrons and come in two types: mesons, composed of a quark and an anti-quark, and baryons, of three quarks or three anti-quarks, of which the most common examples are the proton and the neutron, the

Name	Spin	Baryon Number (B)	Lepton Number (L)	Charge (Q)
Quarks				
u (up)	$1/2$	$1/3$	0	$+2/3$
d (down)	$1/2$	$1/3$	0	$-1/3$
Leptons				
e (electron)	$1/2$	0	1	-1
ν (neutrino)	$1/2$	0	1	0
Gauge bosons				
γ (photon)	1	0	0	0
$W^{\pm}, Z$ (weak bosons)	1	0	0	$\pm 1, 0$
g_i (8 gluons)	1	0	0	0

Table 2.4: L, B and Q quantum number values of fundamental particles [4].

Interaction	Boson	Coupling constants	Range [m]	Typical Reaction Times [s]
Electromagnetic	γ	$\alpha \approx \frac{1}{137}$	∞	$\sim < 10^{-16}$
Weak	$W^{\pm}$,Z^0	$\alpha_W \approx 4\alpha$	10^{-18}	$\sim > 10^{-12}$
Strong	g_i	$\alpha_S \approx 100\alpha$	10^{-15}	$\sim 10^{-23}$

Table 2.5: Boson properties and the ranges of the interactions they mediate

building blocks of everyday matter. The masses of the quarks are listed in table 2.2.

To explain the allowed and dis-allowed reactions, certain quantum numbers were introduced; they are additive and conserved. The three used to classify the fundamental particles are Baryon number (B), Lepton number (L) and electrical charge (Q). The values for the fundamental particles obey are given in table 2.4.

All fermions have anti-particles; the anti-particles have identical masses to their particles but the flavour and the B, L and Q quantum numbers are inverted.

The second type of particle, the bosons, are the force mediators. The electromagnetic interaction is mediated by the photon, which is electrically neutral, massless and observed daily; the massive $W^{\pm}$ and Z^0 bosons are mediators of the weak interaction, and the eight coloured gluons mediate the strong force. A summary of these bosons, and the range of the interactions and lifetimes of the decays they govern is given in table 2.5.

2.1.2 The Interactions

Electromagnetic Charged leptons and quarks couple to the electromagnetic field with a strength of coupling equal to their charges which in turn are proportional to the charge on the electron.

The coupling constant α is relatively weak at $\alpha = \frac{e^2}{4\pi\epsilon_0\hbar c} \approx \frac{1}{137}$. Following the Yukawa hypothesis based on the Heisenberg uncertainty principle it is possible to calculate the range of the interaction based on the mass of the force propagator. As the photon is massless (the current measured upper limit on the mass is $< 10^{-18}$ eV [5]) the range is infinite.

Weak Both quarks and leptons can couple to the weak gauge bosons. The strength of the interaction is given by α_W by analogy with the electromagnetic field; based on a mass of the gauge boson of order 100 GeV, the range of the force is short ranged at order 10^{-18} m. The weak current can be charged or neutral, whereas the electromagnetic current has only a neutral component. The charged current violates parity (the symmetry of spatial inversion) and couples only to left-handed particles (and right-handed anti-particles) however the neutral current will couple to left and right handed particles.

Strong Quarks have an additional charge of colour; conventionally the colour can be red, green or blue. The force mediator for the strong force is the gluon, of which there are eight unique types, and in contrast to the electromagnetic force the gluons themselves carry colour charge, which enables the quarks and gluons to self-interact as do the weak bosons, leading to a non-Abelian field theory. The gluons carry a colour and an anti-colour, allowing colour to be conserved at each interaction vertex, and the interactions of the force occur between quarks and gluons. Since the gluon is massless one would expect the range of the interaction to be infinite; this is not the case. The potential between the quarks is given by:

$$V(r) \propto \frac{\alpha_s}{r} + kr \tag{2.1}$$

where k is known as the "string tension".

The strength of coupling constant α_s increases proportionally with distance to ~ 1 at energies approximately equal to the masses of light hadrons, causing confinement. However due to gluon-gluon vertices an anti-screening effect is produced, causing α_s to tend to 0 at very small distances, causing asymptotic freedom.

2.1.3 Towards Unification

All three coupling constants α, α_W and α_s are dependent on the energy scale of the interaction and are therefore known as running coupling constants. Since the electromagnetic coupling increases at smaller distances and the weak and strong couplings decrease with distance it is conceivable that there could be a distance where these couplings take the same value. If this were the case, at that necessarily very high energy scale it is possible that there is a unified field which contains the three interactions and quarks or leptons would be the source.

2.2 The Standard Model

The Standard Model which unifies the theories of electromagnetic, weak and strong interactions is a gauge theory based on the underlying symmetry $\mathrm{SU(3)}_C \times \mathrm{SU(2)}_L \times \mathrm{U(1)}_Y$. It is necessary to build a Lagrangian density, $\mathscr{L}$, which is invariant under the transformation of these symmetries. The Lagrangian is a function summarising the dynamics of a system, it is obtained by integrating the Lagrangian density over space. The Lagrangian density, which from now on will be referred to as the Lagrangian, is a function only of the fields and their first derivatives. For a given field the equations of motion can be determined from the Lagrangian using the Hamiltonian principle of least action; this states that the transition between two states t_1 and t_2 in a physical system is described by the stationary point of the action, so the variation of the

action, S, should be zero. The action is related to the Lagrangian as:

$$S = \int_{t_1}^{t_2} \mathscr{L}(\partial_\mu \Psi, \Psi) d^4x \tag{2.2}$$

where μ = 0, 1, 2, 3 and Ψ represents a field. This leads to the Euler-Lagrange equation which gives the equation of motion for Ψ:

$$\frac{\partial \mathscr{L}}{\partial \Psi} - \partial_\mu \frac{\partial \mathscr{L}}{\partial(\partial_\mu \Psi)} = 0 \tag{2.3}$$

An example would be to take a Lagrangian for a free fermion field (ψ) with a mass (m):

$$\mathscr{L}_f = i\bar{\psi}\gamma^\mu \partial_\mu \psi - m\bar{\psi}\psi \tag{2.4}$$

Evaluating the Euler-Lagrange equation for this Lagrangian gives the Dirac equation, which describes the equation of motion of the free fermion:

$$(i\gamma^\mu \partial_\mu - m)\psi = 0 \tag{2.5}$$

Noether's theorem states that if a Lagrangian is invariant under a symmetry transformation of the fields then a conserved quantity is determined by the Lagrangian. One example is that a Lagrangian which is invariant under space-time translations leads to four-momentum conservation. This relationship between symmetries and conserved quantities can also be used to investigate the consequences of charge conservation; charge conservation is related to the symmetry of phase transformations [4].

Let us consider the symmetry group of phase transformations, the U(1) group. Using the Lagrangian for a free spinor, eq. 2.4, for a local transformation, where the parameter Λ depends

on the position in space-time, the field transforms under U(1) as:

$$\psi \rightarrow \psi' = exp[iq\Lambda(x)]\psi(x) \tag{2.6}$$

where q is charge.

The Lagrangian given in eq. 2.4 is not invariant: while the mass term is, the derivative term destroys the invariance due to the dependence of Λ on x. Thus it is necessary to introduce a covariant derivative term which transforms in such a way as to cancel this new term by transforming in the same manner as the fields themselves:

$$\mathscr{D}_\mu\psi \rightarrow exp[iq\Lambda(x)]\mathscr{D}_\mu\psi \tag{2.7}$$

where the gauge covariant derivative is given by:

$$\mathscr{D}_\mu \equiv \partial_\mu + iqA_\mu(x) \tag{2.8}$$

where A_μ is a vector field introduced to ensure the exact cancellation under this transformation. It transforms as:

$$A_\mu(x) \rightarrow A_\mu(x) - \partial_\mu\Lambda(x) \tag{2.9}$$

A_μ can be directly associated with the physical photon field. Introducing a kinetic term for the photon, the Lagrangian now takes the form of the Quantum ElectroDynamics (QED) Lagrangian:

$$\mathscr{L}_{QED} = \bar{\psi}(i\gamma^\mu\partial_\mu - m)\psi - qA_\mu\bar{\psi}\gamma^\mu\psi - \frac{1}{4}F_{\mu\nu}F^{\mu\nu} \tag{2.10}$$

where $F_{\mu\nu}$ is given by:

$$F_{\mu\nu} = \partial_\mu A_\nu - \partial_\nu A_\mu \tag{2.11}$$

There is no mass term present in this Lagrangian for the photon. To introduce a mass term,

which would be of the form:

$$\mathscr{L}_\gamma = \frac{1}{2} m_\gamma^2 A_\mu A^\mu \tag{2.12}$$

would break the invariance of the system. Imposing local gauge invariance here has thus necessitated the introduction of a new vector boson field with a massless boson, which interacts with the fermion field.

In a similar manner to that used to build the local gauge theory of the electromagnetic interaction, QED, the strong interaction can be constructed as the local gauge theory Quantum ChromoDynamics (QCD) [6].

To form a local gauge theory of the weak interactions however is trickier. The requirement of local gauge invariance leads to massless bosons, which is suitable for the photon and the gluons, but experimentally the weak bosons have been shown to be massive [7–10]. A local gauge theory of the weak interactions with massive bosons is achieved by unifying the electromagnetic and weak interactions, as in the Glashow-Weinberg-Salam model [11–13] , an example of a Yang-Mills theory [14]. The symmetry must be broken spontaneously to give mass to the bosons; this can be done using the Higgs mechanism [15–19]. Masses can then also be given to the fermions through the Yukawa interaction.

Let us follow the same procedure used to develop the QED formalism to construct the local gauge theory of the strong interaction. The underlying symmetry group is SU(3)$_C$. Beginning from the Lagrangian for a free quark:

$$\mathscr{L}_q = \bar{q_i}(i\gamma^\mu \partial_\mu - m) q_i \tag{2.13}$$

where q_i is a quark with one of the three colours, red (R), green (G) or blue (B). The quark fields transform under the colour symmetry transformation as:

$$q_i(x) \rightarrow (e^{i\alpha_a(x)T^a})_{ij} q_j(x) \tag{2.14}$$

where α_a are the group parameters and T^a are the eight group generator matrices. As in QED, to ensure invariance it is necessary to introduce a covariant derivative:

$$\mathscr{D}_\mu = \partial_\mu + ig_S T^a G^a_\mu \tag{2.15}$$

where g_S is the coupling strength of the strong interaction. This derivative includes the eight gauge fields G^a_μ which transform as follows:

$$G^a_\mu \rightarrow G^a_\mu - \frac{1}{g_S}\partial_\mu \alpha_a - f_{abc}\alpha_b G^c_\mu \tag{2.16}$$

where f_{abc} are the structure constants of the SU(3)$_c$ group.

To finish let us add a gauge invariant kinetic term for the gauge fields, which yields the gauge invariant Lagrangian:

$$\mathscr{L}_{QCD} = \bar{q}_i(i\gamma^\mu \partial_\mu - m)q_i - g_S(\bar{q}_i \gamma^\mu T^a_{ij} q_j)G^a_\mu - \frac{1}{4}G^a_{\mu\nu}G^{\mu\nu}_a \tag{2.17}$$

The final term describes the self interactions between the gluons and $G^a_{\mu\nu}$ is the field strength tensor given by:

$$G^a_{\mu\nu} = \partial_\mu G^a_\nu - \partial_\nu G^a_\mu - g_S f_{abc} G^b_\mu G^c_\nu \tag{2.18}$$

The underlying symmetry group of the electroweak gauge theory is SU(2)$_L$ $\times$ U(1)$_Y$, weak isospin (I) $\times$ weak hypercharge (Y), the L subscript indicates that the weak isospin only couples with left handed fermions and right handed anti-fermions. Due to this, the fermions transform as left-handed doublets (χ_L) and right-handed singlets (ψ_R).

$$\begin{aligned} \chi_L &= \begin{pmatrix} \nu_e \\ e^- \end{pmatrix}_L \quad or \quad \begin{pmatrix} u \\ d \end{pmatrix}_L \\ \psi_R &= e^-_R \quad or \quad u_R \quad or \quad d_R \end{aligned} \tag{2.19}$$

Fermion	Q	I	I^3	Y
e_L^-,μ_L^-,τ_L^-	-1	$1/2$	$-1/2$	-1
ν_{e_L},ν_{μ_L},ν_{τ_L}	0	$1/2$	$1/2$	-1
u_L,c_L,t_L	$2/3$	$1/2$	$1/2$	$1/3$
d_L,s_L,b_L	$-1/3$	$1/2$	$-1/2$	$1/2$
e_R^-,μ_R^-,τ_R^-	-1	0	0	-2
u_R,c_R,t_R	$2/3$	0	0	$4/3$
d_R,s_R,b_R	$-1/3$	0	0	$-2/3$

Table 2.6: Quantum numbers for fermions.

The electromagnetic charge is related to weak isospin and weak hypercharge through the Gell-Mann–Nishijima relation [20]:

$$Q = I^3 + \frac{Y}{2} \tag{2.20}$$

where I^3 is the third component of isospin. In table 2.6 a summary of the values of these quantum numbers for each fermion can be found.

In nature the charged weak interaction only affects left-handed particles (and right-handed anti-particles) however the neutral weak interaction and the electromagnetic interaction both act on left and right-handed particles. The electroweak interaction introduces four gauge vector fields $W_\mu^{1,2,3}$ and B_μ. The interaction term with the left-handed doublet under SU(2)$_L$ is given by:

$$-ig\bar{\chi_L}\gamma_\mu T^a W_\mu^a \chi_L \tag{2.21}$$

where $a = 1, 2, 3$ and T^a are the generators of the SU(2) group. The interaction term with the fermion field under U(1)$_Y$ is given by:

$$-g'\bar{\chi}_L\gamma_\mu\frac{Y}{2}\chi_L B^\mu - g'\bar{\psi}_R\gamma_\mu\frac{Y}{2}\psi_R B^\mu \tag{2.22}$$

The actual vector bosons seen in nature are linear combinations of these four vector fields, where the relations after symmetry breaking (described later in this section) and mixing are

given by:

$$\begin{aligned} W_\mu^\pm &= \tfrac{1}{\sqrt{2}}(W_\mu^1 \pm iW_\mu^2) \\ Z_\mu &= cos\theta_W W_\mu^3 - sin\theta_W B_\mu \\ A_\mu &= sin\theta_W W_\mu^3 + cos\theta_W B_\mu \end{aligned} \tag{2.23}$$

where θ_W is the weak mixing angle, also known as the Weinberg angle. The components of the B_μ field in each vector boson enables the right-handed interactions for the neutral Z_μ and A_μ bosons.

Thus by requiring local gauge invariance under the symmetry transformations of the product of the groups SU(2)$_L$ × U(1)$_Y$ the following Lagrangian is obtained:

$$\begin{aligned} &\mathscr{L}_{EW} = \bar{\chi}_L \gamma^\mu [i\partial_\mu - igT^a W_\mu^a - g'\tfrac{Y}{2} B_\mu]\chi_L \\ &+\bar{\psi}_R \gamma^\mu [i\partial_\mu - g'\tfrac{Y}{2} B_\mu]\psi_R \\ &-\tfrac{1}{4} W_{\mu\nu} W^{\mu\nu} - \tfrac{1}{4} B_{\mu\nu} B^{\mu\nu} \end{aligned} \tag{2.24}$$

for massless fermions and bosons.

In order to address the issue of the massive gauge bosons in a gauge invariant manner let us begin by introducing four real scalar fields ϕ_i. These must be invariant under SU(2)$_L$ × U(1)$_Y$ symmetry so we introduce them as a weak isospin doublet with weak hypercharge $Y = 1$, and weak isospin $I = {}^1/_2$.

$$\phi = \begin{pmatrix} \phi^+ \\ \phi^0 \end{pmatrix} = \begin{pmatrix} \phi_1 + i\phi_2 \\ \phi_3 + i\phi_4 \end{pmatrix} \tag{2.25}$$

Having weak isospin charge and weak hypercharge allows these fields to couple to the weak bosons. We can now introduce the gauge invariant Lagrangian piece for these fields as:

$$\mathscr{L}_{Higgs} = |(i\partial_\mu - gT^a W_\mu^a - g'\frac{Y}{2} B_\mu)\phi|^2 - V(\phi) \tag{2.26}$$

where $V(\phi)$ is the Higgs potential which takes the form:

$$V(\phi) = \mu^2\phi^\dagger\phi + \lambda(\phi^\dagger\phi)^2 \tag{2.27}$$

where μ^2 is the mass term and λ is the self-coupling constant for the Higgs field. The choice of constraints upon these parameters is very important, $\lambda > 0$ ensures that the potential is bounded below. If we select $\mu^2 > 0$ the potential is u-shaped with a single minimum at 0 as illustrated on the left in figure 2.1. However requiring $\mu^2 < 0$ creates a "Mexican-hat" potential, as illustrated on the right in figure 2.1. This potential now has an infinite number of ground states at non-zero values, which are no longer symmetrically invariant. Therefore the act of selecting a ground state "breaks" or rather hides the symmetry.

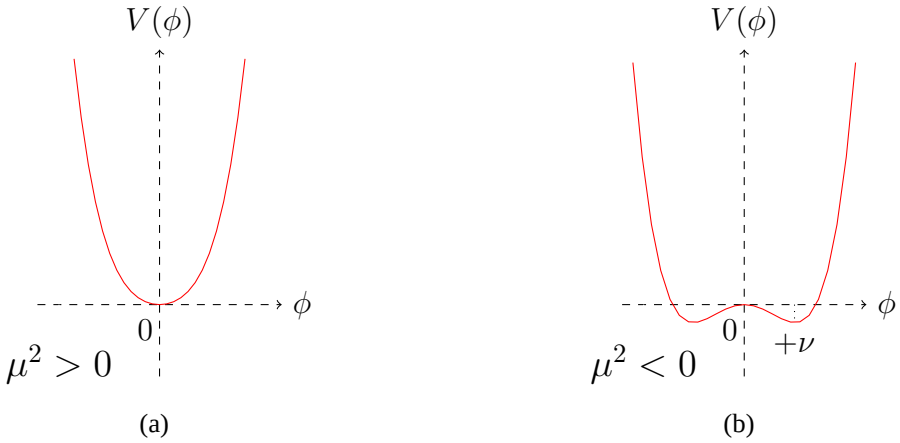

Figure 2.1: The Higgs potential where $\mu^2 > 0$ on the left and $\mu^2 < 0$ on the right.

Let us select our ground state as:

$$\phi_0 = \frac{1}{\sqrt{2}}\begin{pmatrix} 0 \\ v \end{pmatrix} \tag{2.28}$$

where v is the vacuum expectation value and can also be represented as:

$$v = -\left(\frac{\mu^2}{\lambda}\right)^{\frac{1}{2}} \tag{2.29}$$

This choice is specific, choosing an electrically neutral ground state will leave the U(1)$_{EM}$ symmetry intact. Since this is in an exact symmetry it will have a massless boson, therefore the photon remains massless. The way in which to select the ground state is by a rotation of the field ϕ to ϕ_0. Let us parametrise the field ϕ and the fluctuations around the minimum in terms of the four fields $\theta^{1,2,3}$ and $H(x)$ as

$$\phi(x) = \begin{pmatrix} \theta_2 + i\theta_1 \\ \frac{1}{\sqrt{2}}(v + H(x)) - i\theta_3 \end{pmatrix} = e^{i\theta_a(x)\tau^a(x)/v} \begin{pmatrix} 0 \\ \frac{1}{\sqrt{2}}(v + H(x)) \end{pmatrix} \tag{2.30}$$

then rotate; the three degrees of freedom of the fields, representing three massless Goldstone bosons [21–25] , $\theta_{1,2,3}$, are absorbed by the weak gauge bosons as third degrees of freedom. This third degree is a longitudinal one in addition to the two transverse degrees and gives the masses to the weak bosons. Let us now insert ϕ_0:

$$\phi_0(x) = \frac{1}{\sqrt{2}} \begin{pmatrix} 0 \\ v + H(x) \end{pmatrix} \tag{2.31}$$

where $H(x)$ represents the Higgs boson, into the Lagrangian in equation 2.26 and the masses of the bosons appear. Evaluating the first term of the Lagrangian gives the couplings of the vector bosons to the Higgs field and the vector boson masses; the W^3_μ and B_μ fields are coupled by a 2×2 mass matrix which must be diagonalised to give M_A and M_Z, the masses are given as:

$$\begin{aligned} M_W &= \tfrac{1}{2} v g \\ M_Z &= \tfrac{1}{2} v \sqrt{g^2 + g'^2} \\ M_A &= 0 \end{aligned} \tag{2.32}$$

where M_A was deliberately engineered. The masses M_W and M_Z are related by the Weinberg angle:

$$\frac{M_W}{M_Z} = \cos\theta_W \tag{2.33}$$

Evaluating the second term gives the Higgs field self-coupling and the Higgs boson mass term:

$$M_H = \sqrt{2v^2\lambda} = \sqrt{2}\mu \tag{2.34}$$

The masses of the fermions arise through Yukawa interactions with the scalar field. The gauge invariant Yukawa couplings are required by renormalisability, for the electron the term is:

$$\mathscr{L}_e = -\lambda_e[\bar{\chi}_L\phi(x)e_R + \bar{e}_R\bar{\phi(x)}\chi_L] \tag{2.35}$$

where λ_e is the coupling constant of the electron. For the quark masses, it is necessary to introduce an additional Higgs doublet, to give masses to the up-type quarks, which when broken takes the form:

$$\phi_C = \frac{1}{\sqrt{2}}\begin{pmatrix} v+H \\ 0 \end{pmatrix} \tag{2.36}$$

It enables us to construct the gauge invariant Lagrangian piece for the quark masses, for the first generation quarks this is:

$$\begin{aligned}\mathscr{L}_{ud} &= -\lambda_d\bar{\chi}_L\phi d_R - \lambda_u\bar{\chi}_L\phi_C u_R \\ &-\lambda_d\bar{d}_R\bar{\phi}\chi_L - \lambda_u\bar{u}_R\bar{\phi}_C\chi_L\end{aligned} \tag{2.37}$$

No predictions for the fermion masses are given by the theory as the couplings are added manually and the mass terms are proportional to the couplings, in the form:

$$M_f = \lambda_f\frac{v}{\sqrt{2}} \tag{2.38}$$

Here for simplicity the left-handed doublets and right-handed singlets of quarks are as defined in eq. 2.19 however the weak interaction actually acts on a doublet of quarks which are linear combinations of mass eigenstates. These mass eigenstates are related to the flavour eigenstates by the CKM matrix [26, 27].

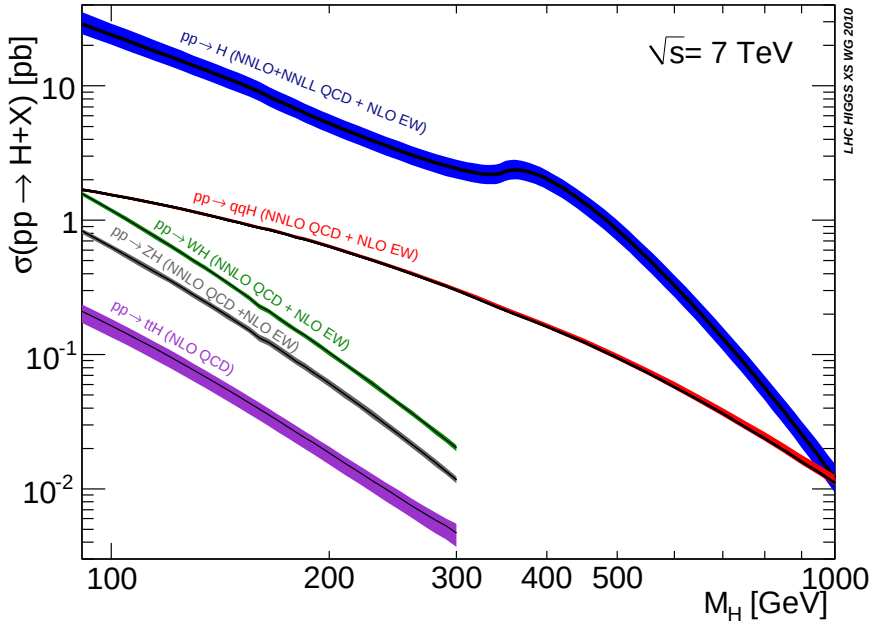

Figure 2.2: The production cross-sections for each production mechanism as a function of the Higgs boson mass at a centre of mass energy of 7 TeV [28]; in order of decreasing cross-section these are gluon-gluon fusion, vector boson fusion, associated production with a W boson, with a Z boson and associated production with top quarks.

2.3 The Higgs Boson

2.3.1 Higgs Boson Production at the LHC

The Higgs boson production cross-section for each mode at a centre of mass energy 7 TeV is shown in figure 2.2 as a function of Higgs boson mass (M_H). These show that at the LHC gluon-gluon fusion is the dominant production mechanism for the Standard Model Higgs boson across the whole mass spectrum. These theoretical predictions were derived using the latest tools at either NNLO or NLO for each production mode, they are the product of collaboration between the theoretical and the experimental communities (ATLAS and CMS) [28]. The four dominant production mechanisms at the LHC are illustrated in figure 2.3.

In figure 2.3 (top-left), the associated production of a Higgs boson with a W or Z weak boson is shown in which the Higgs is radiated from the vector boson (Higgstrahlung). This process has a rapidly falling cross-section with M_H, as illustrated in figure 2.2.

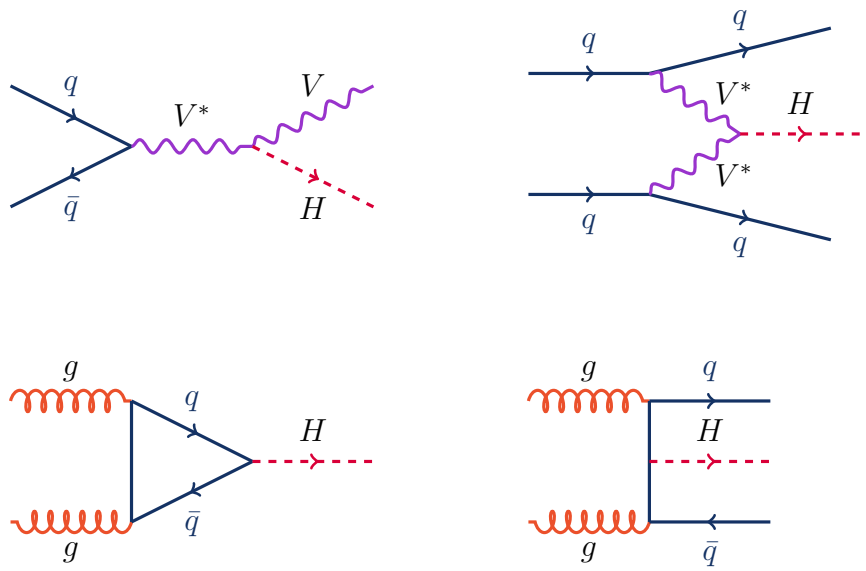

Figure 2.3: The dominant production processes of the Standard Model Higgs boson [29]; (top-left) associated production with a W or Z boson, (top-right) vector boson fusion, (bottom-left) gluon-gluon fusion, (bottom-right) associated production with heavy quarks.

Figure 2.3 (top-right) illustrates vector boson fusion (VBF) from W^+W^- or Z^0Z^0 bosons; the W or Z bosons are radiated from quarks; they fuse to form a Higgs boson. The quarks then hadronise to form very high momentum forward jets. As there is no colour connection between them, there is a lack of hadronic activity between them. This leaves a clear signature for discrimination against a background of multijets (often known as QCD background). This production process has the second highest cross-section at the LHC.

In figure 2.3 (bottom-left), gluon-gluon fusion (ggF) is shown; this process has the highest production cross-section at the LHC by a significant margin. The two gluons fuse via a heavy quark (top or bottom) loop. Since there are large QCD backgrounds, it is necessary to rely on striking signatures from the Higgs decay to provide the discrimination. Examples are given in section 2.3.2.

In figure 2.3 (bottom-right), associated production with heavy top or bottom quarks is depicted; with such a small production cross-section this channel is often combined with the $b\bar{b}$ decay channel as it has the largest branching ratio. However this is very challenging, once again due to the overwhelming QCD background.

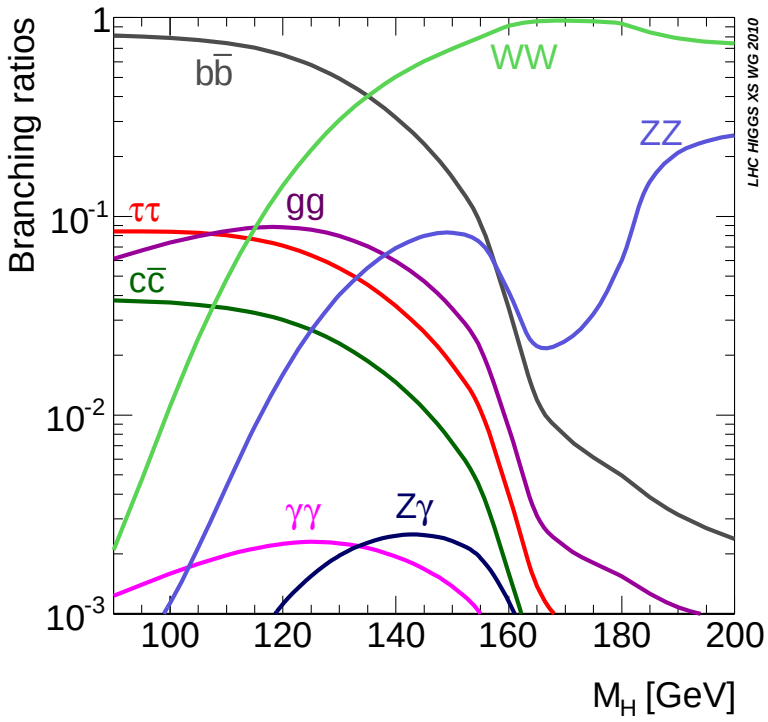

Figure 2.4: The Higgs boson branching ratios as a function of the Higgs boson mass [28].

2.3.2 Higgs Boson Decays at the LHC

The branching ratios for the main Standard Model Higgs boson decays are shown in figure 2.4 as a function of Higgs mass. Certain combinations of production and decay modes are chosen as points of focus due to the differing difficulties in discriminating backgrounds. In the low mass region, $M_H < 130$ GeV, the decays to $\tau^+\tau^-$ (from VBF production) and $\gamma\gamma$ are the most important. The $b\bar{b}$ decay channel is very challenging to distinguish from the QCD background; the $\tau^+\tau^-$ channel has the next-largest branching ratio and the two forward jets from VBF are the signature which provide the discrimination against the QCD background therefore this is an important channel in this mass range. The $\gamma\gamma$ decay mode has a very clear signature but a very small cross-section. At $M_H > 130$ GeV the $H \to WW$ channel is crucial because of the high branching ratio, this is the most sensitive channel in the early data searches at the LHC. At these and higher masses of $M_H > 200$ GeV the $H \to ZZ$ channel, particularly if the ZZ pair decay to four leptons, is very promising due to its unique signature.

2.3.3 Higgs Boson Mass Constraints

The mass of the Higgs boson is the only unmeasured parameter of the Standard Model. As the Higgs boson itself is still currently unobserved we can only place constraints on its mass. The constraints that exist so far fall into three categories, theoretical, indirect experimental and direct experimental.

2.3.3.1 Mass Constraints from Theory

The theoretical constraints on the mass of the Higgs boson derive from the considerations of the energy range in which the perturbative calculations of the Standard Model are valid. These constraints come from unitarity, the perturbativity of the Higgs self-coupling, the stability of the electroweak vacuum and fine tuning. These constraints are documented in detail elsewhere [29], but can be summarised as 70 GeV $< M_H <$ 1 TeV.

2.3.3.2 Mass Constraints from Experiment

The indirect experimental constraints are provided from high precision measurements of electroweak data. Due to the contributions that the Higgs boson makes to radiative corrections to a number of electroweak observables, fitting these observables can provide us with limits on the Higgs mass. The most recent iteration of this fit is shown in figure 2.5, where the direct experimental search results are not included and the Higgs mass is estimated to be $M_H = 96^{+31}_{-24}$ GeV [30]. Also on figure 2.5 are the results of the most recent direct search experimental exclusion limits available from LEP [31] and the Tevatron [32] when the fit was made. When these direct experimental limits, and those obtained from the ATLAS [33] and CMS [34] collaborations during 2010, are included in the fit, the estimation is $M_H = 120^{+12}_{-5}$ GeV [30].

There are three experimental constraints from direct searches at the three particle accelerators: LEP, Tevatron and LHC.

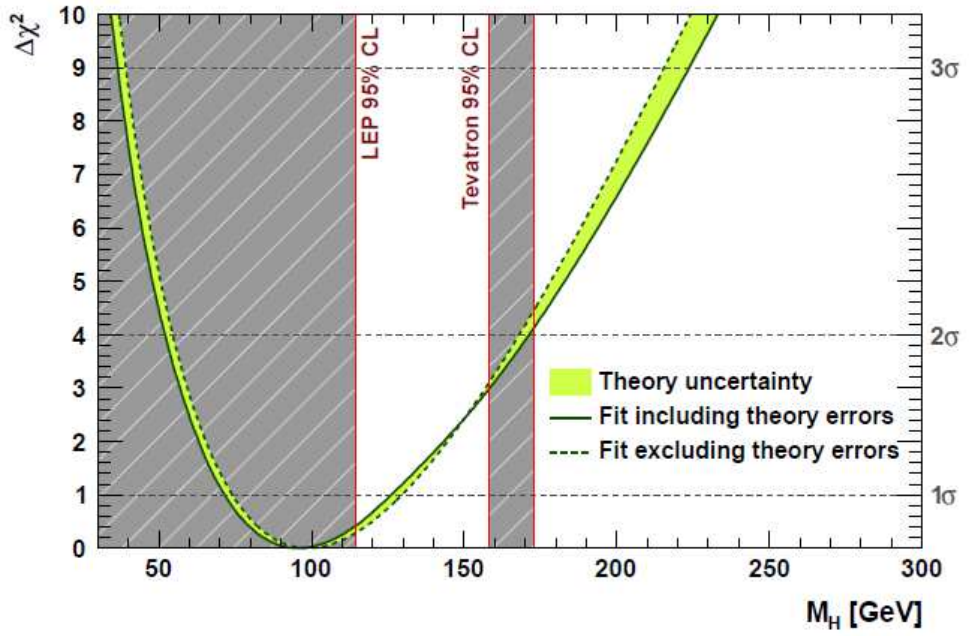

Figure 2.5: Indirect determination of the Higgs boson mass: $\Delta\chi^2$ as a function of M_H [30]. The direct experimental limits are not included in the fit and the best fit value of $M_H = 96^{+31}_{-24}$ GeV.

Mass Constraints from LEP A direct search at LEP was performed at centre-of-mass energies up to $\sqrt{s} = 209$ GeV. The combined results of the four collaborations did not observe a signal and set an exclusion limit of $M_H > 114.4$ GeV at 95% Confidence Level (C.L.) [31].

Mass Constraints from Tevatron The CDF and D0 collaborations at the Tevatron have performed a wide range of direct Higgs searches in $p\bar{p}$ collisions at a centre-of-mass energy of $\sqrt{s} = 1.96$ TeV. The results from both collaborations were combined with up to 8.2 fb^{-1} of analysed data from CDF and up to 8.6 fb^{-1} from D0. The most recently released limits at the time of writing set the exclusion limit range of $156 < M_H < 177$ GeV at 95% C.L. [35] as shown in figure 2.6.

Mass Constraints from LHC Since the beginning of the operation of the LHC at the centre-of-mass energy $\sqrt{s} = 7$ TeV, the ATLAS and CMS collaborations have been fervently searching for the Higgs. As the LHC records data at an almost daily-increasing rate currently, the experimental limits are updated very rapidly.

At the time of writing the most recent limit set by the ATLAS experiment excludes three

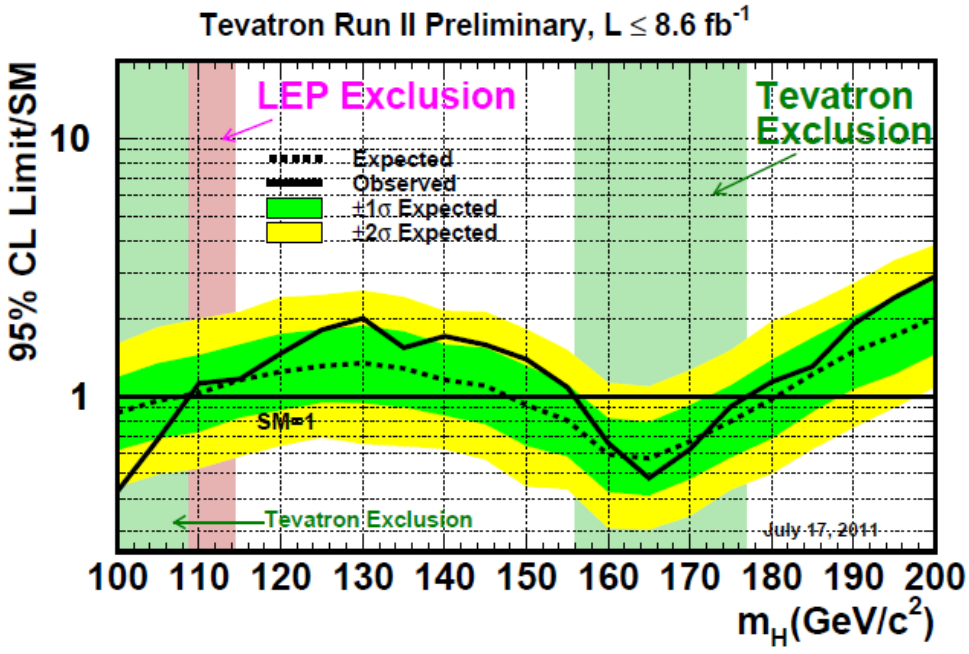

Figure 2.6: Observed and expected 95% C.L. upper limits on the ratios to the SM cross-section, as functions of the Higgs boson mass for the combined CDF and D0 analyses [35].

mass ranges for the Standard Model Higgs boson at 95 % C.L., these excluded regions are 146 - 230 GeV, 256 - 282 GeV and 296 - 459 GeV [36] by combining numerous analyses in different decay channels using 1.0 to 2.3 fb^{-1} of proton-proton collision data.

The most recent limit set by the CMS experiment also excludes three mass ranges at 95 % C.L., 145 - 216 GeV, 226 - 288 GeV and 310 - 400 GeV [37].

These results from the ATLAS and CMS collaborations have been combined [38] and together the full mass range 141 - 476 GeV has been excluded at 95% C.L. and the range 146 - 443 GeV has been excluded at 99% C.L. except for three small regions between 220 and 320 GeV. This combined exclusion is shown in figure 2.7, with shaded areas representing the mass regions excluded by LEP and the Tevatron to highlight how little of the mass range remains to be excluded.

2.3.3.3 Looking Forward

As the Tevatron continues to analyse its recorded data and the LHC continues to record data at an impressive rate the immediate future is an exciting time. The mass range in which the Higgs

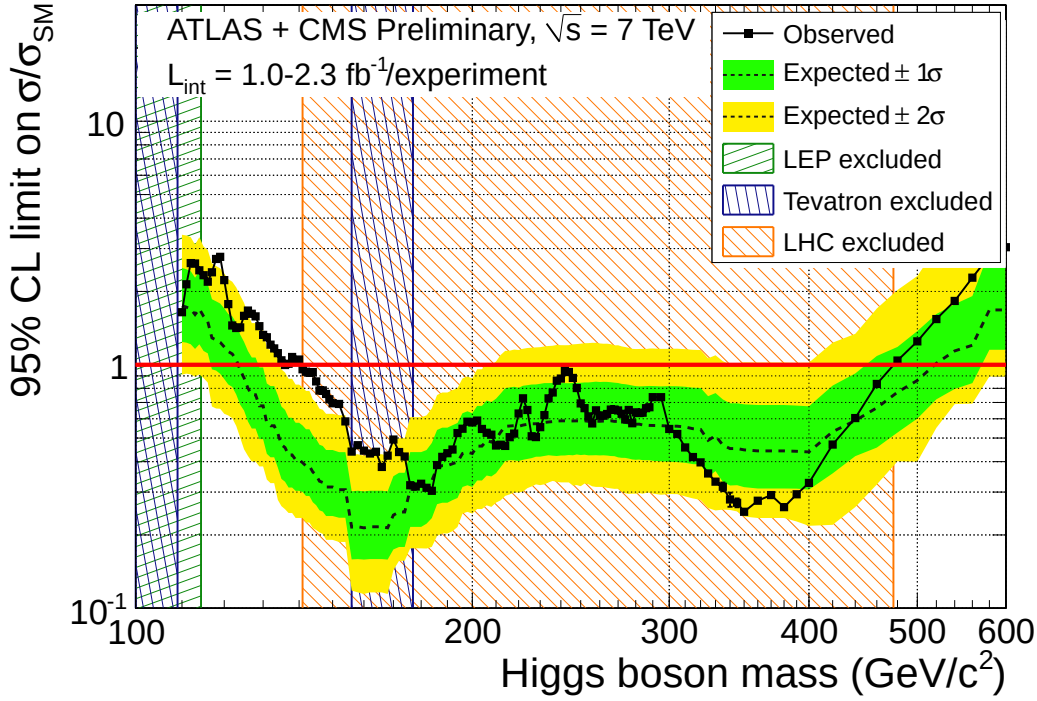

Figure 2.7: Observed and expected 95% C.L. upper limits on the ratios to the SM cross-section, as functions of the Higgs boson mass of the combined results from the ATLAS and CMS experiments [38].

boson could be discovered is rapidly shrinking. If the SM Higgs boson exists it will surely not be long before it is experimentally observed; on the other hand if the SM Higgs boson is excluded then the search will continue for new physics to explain the how the particles in the SM acquire their masses.

Chapter 3

ATLAS Experiment

3.1 The Large Hadron Collider

The Large Hadron Collider (LHC) [39] at CERN was designed to accelerate and collide two beams of 2808 bunches of protons to a design centre-of-mass energy of 14 TeV with a nominal luminosity of 10^{34} cm^{-2} s^{-1}. Each bunch consists of 1.15×10^{11} protons and circulates at a frequency of 11 kHz, leading to a bunch spacing of 25 ns and a bunch-crossing frequency of 40 MHz.

It is also capable of colliding two beams of bunches of lead nuclei at an energy of 2.76 TeV per nucleon, giving rise to a centre-of-mass energy of 1.15 PeV and a design luminosity of 10^{27} cm^{-2} s^{-1}.

In order to reach such high energies the particles go through a series of systems to incrementally increase their energy prior to injection into the main LHC ring. These systems are illustrated in figure 3.1; the protons are generated at 50 MeV in the Linac2, then accelerated to 1.4 GeV by the Proton Synchrotron Booster (PSB); then the protons are injected into the Proton Synchrotron (PS) where they reach energies of 25 GeV and the final stage before injection into the main LHC ring is the Super Proton Synchroton (SPS) where the protons are accelerated to 450 GeV.

At the four points where the two beams interact there are four experiments stationed:

- ALICE: A Large Ion Collider Experiment is specially designed to study nucleus-nucleus interactions during the heavy ion collisions [40]
- ATLAS: A Toroidal LHC ApparatuS is designed as a general purpose detector to search for the Higgs boson and beyond the Standard Model physics [41]

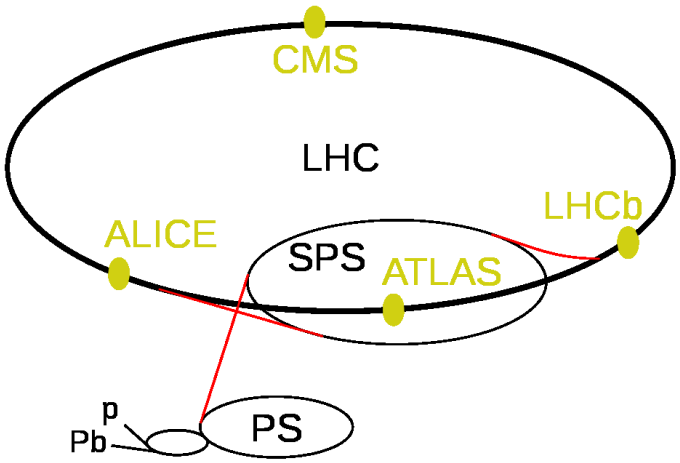

Figure 3.1: A diagram illustrating the layout of the four experiments: ALICE, ATLAS, CMS, and LHCb on the LHC ring as well as the injection system, where p is the Linac2, Pb is the Linac3 for heavy ions, PS is the Proton Synchrotron and SPS the Super Proton Synchrotron.

- CMS: Compact Muon Solenoid is another general purpose detector with the same aims but a different design [42]
- LHCb: Large Hadron Collider beauty experiment is purpose built to measure *CP* violation and rare *B* meson decays [43]

The positions of all four experiments are shown in figure 3.1.

During 2010 when the data were collected for the analysis described in this thesis the LHC was operating at a centre of mass energy of 7 TeV and a peak instantaneous luminosity during the data taking period of 2.1 x 10^{32} cm^{-2} s^{-1} was achieved with 348 colliding bunches [44].

3.2 The ATLAS Detector

The ATLAS detector is one one of two general purpose detectors at the LHC. Due to the wide and varied physics program the detector has a large range of design considerations to meet. These are as follows:

- Efficient tracking in a high luminosity environment, for identification of electrons, photons and τ leptons and for precision measurements of lepton transverse momentum

- Accurate vertexing to allow for secondary vertex reconstruction and b-tagging and for use in τ lepton identification [45]
- Precise electromagnetic calorimetry for measurement and identification of electrons, photons and τ leptons
- Full coverage with the hadronic calorimeters for accurate jet and E_T^{miss} measurements
- High precision in the muon momentum measurements
- A fast and efficient triggering system to deal with the high event rates

A schematic of the ATLAS detector demonstrating the relative positions of each of the subsystems can be seen in figure 3.2; the two people on the left hand side illustrate the scale. From the centre outwards the ATLAS detector consists of the Inner Detector, including the pixel detector, the semiconductor tracker and the transition radiation tracker, then the Liquid Argon electromagnetic and Tile hadronic calorimeters followed by the muon spectrometer system.

3.2.1 The ATLAS Coordinate System

The coordinate system is defined taking the origin to be the interaction point; the z axis runs along the direction of the beam and the $x-y$ plane transverse to it. The x axis is positive, pointing towards the centre of the LHC ring, and the y axis is positive when pointing up. The azimuthal angle ϕ is defined around the ring in the $x-z$ plane and the polar angle θ is defined from the beam line, in the $y-z$ plane.

Pseudorapidity (η) is defined as:

$$\eta = -\ln\left[\tan\left(\frac{\theta}{2}\right)\right] \tag{3.1}$$

The distance ΔR is defined as:

$$\Delta R = \sqrt{\Delta\eta^2 + \Delta\phi^2} \tag{3.2}$$

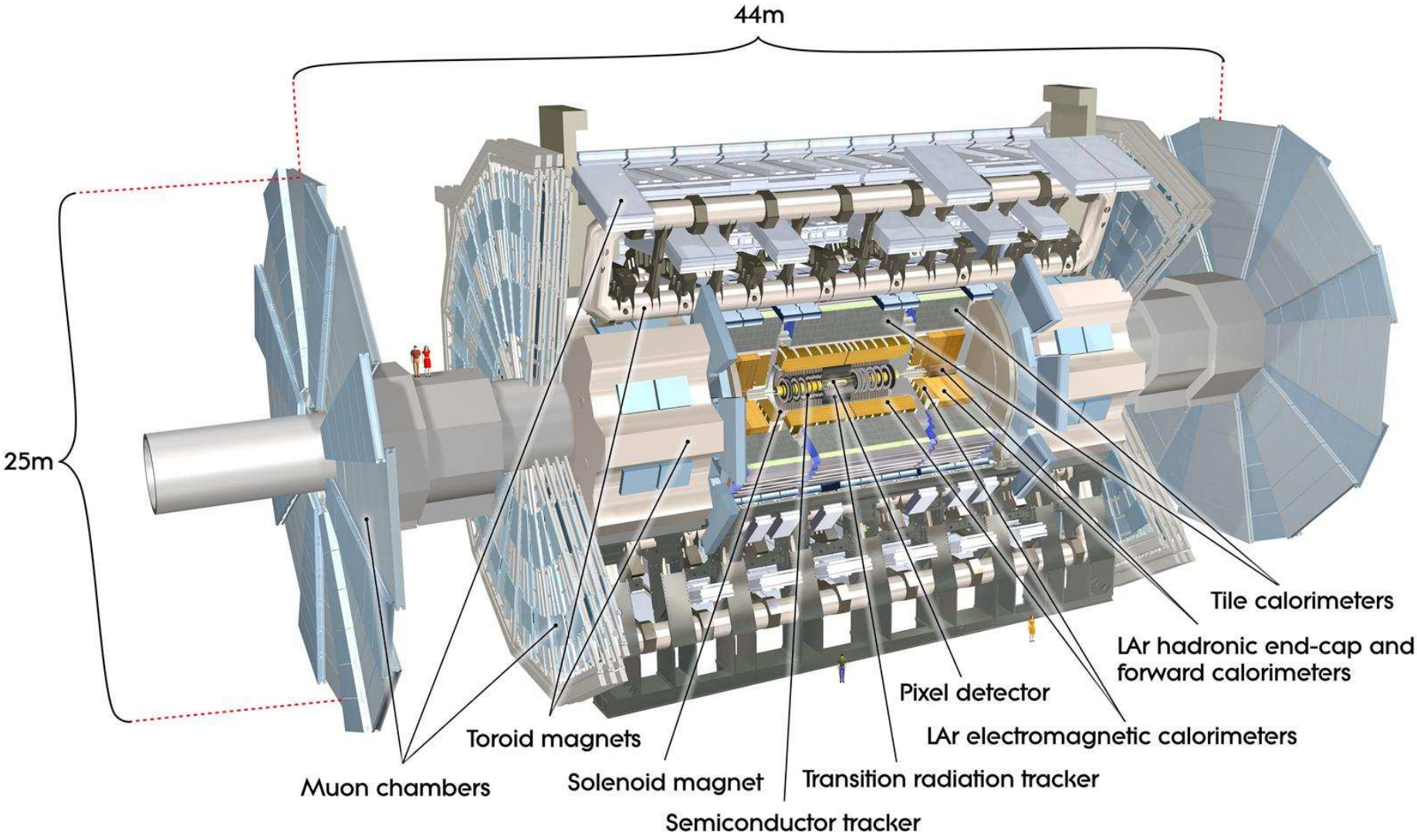

Figure 3.2: A schematic diagram showing the layout of the individual subdetectors of the ATLAS detector and total size.

The quantities transverse momentum p_T, transverse energy E_T and missing transverse energy E_T^{miss} are defined in the $x - y$ plane.

3.2.2 Performance in 2010

During 2010 the LHC collided proton beams at a centre of mass energy of 7 TeV. The increase in instantaneous luminosity over the period of running in 2010 is shown in figure 3.3(a) [46], and the total integrated luminosity delivered by the LHC during this period is shown in figure 3.3(b) [46] compared to the amount of luminosity recorded by the ATLAS detector. Taking the ratio of the recorded luminosity to the delivered gives a data-taking efficiency of 93.6 %, weighted by luminosity. The luminosity determination is measured using the luminosity detectors and calibrated using Van-Der-Meer scans [47] and the most recent measurement has a systematic uncertainty of 3.4 % [48].

During this period all subdetectors performed well; a summary of the percentage of the data taking period when each subdetector was running and collecting data can be seen in table 3.1 [49], an excellent achievement for the first year of running at this record breaking energy. The number of channels in each subdetector is shown in table 3.2 along with the approximate operational fraction which shows the scale of the task [50].

Inner Detector			Calorimeters				Muon Spectrometers			
Pixel	SCT	TRT	LAr EM	LAr HAD	LAr FWD	Tile	MDT	RPC	CSC	TGC
99.1	99.9	100	90.7	96.6	97.8	100	99.9	99.8	96.2	99.8

Table 3.1: A table summarising the luminosity weighted relative fraction of good quality data delivered by the ATLAS subsystems during all LHC runs with stable beam conditions and collisions at a centre of mass energy of 7 TeV after the turn-on of the tracking detectors, taken between March 30^{th} and October 31^{st} 2010. The subsystems are Pixel, Silicon Tracker (SCT), Transition Radiation Tracker (TRT), Liquid Argon Electromagnetic Calorimeter (LAr EM), Liquid Argon Hadronic Calorimeter (LAr HAD), Liquid Argon Forward Calorimeter (LAr FWD), Tile Hadronic Calorimeter (Tile), Monitored Drift Tube Chambers (MDT), Resistive Plate Chambers (RPC), Cathode Strip Chambers (CSC) and Thin Gap Chambers (TGC).

Inner Detector			Calorimeters				Muon Spectrometers			
Pixel	SCT	TRT	LAr EM	LAr HAD	LAr FWD	Tile	MDT	RPC	CSC	TGC
80M	6.3M	350K	170K	5600	3500	9800	350K	370K	31K	320K
96.4	99.2	97.5	99.8	9.6	99.8	96.2	99.7	97.0	97.7	97.9

Table 3.2: A table giving the number of channels for each ATLAS subsystem and the approximate operational fraction. Current on May 13^{th} 2011.

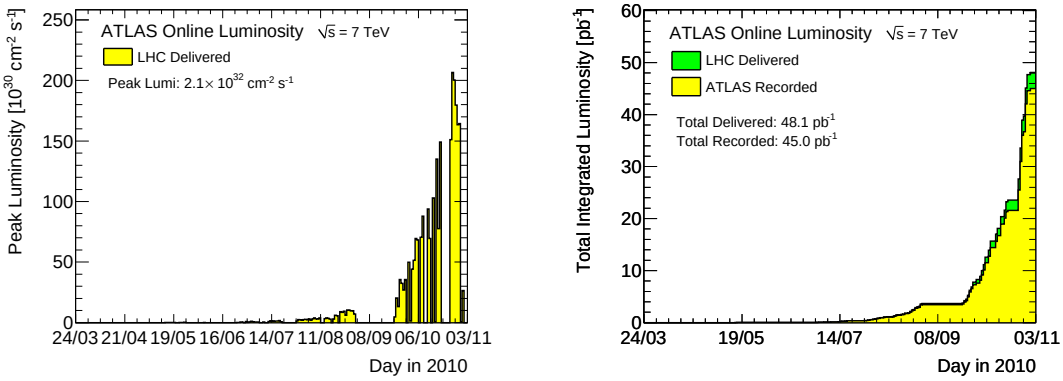

(a) Peak Luminosity (b) Sum Luminosity

Figure 3.3: Peak luminosity(left) delivered by the LHC(yellow) and cumulative sum of luminosity(right) both delivered by the LHC(green) and recorded by ATLAS(yellow) for stable beam conditions and proton-proton collisions at a centre of mass energy of 7 TeV plotted versus day.

3.2.3 Magnet Systems

The ATLAS detector magnet system consists of four magnets: one barrel solenoid provides a 2 T axial field for the Inner Detector tracking, the other three are a barrel and two end-cap toroids, providing 0.5 T and 1.0 T toroidal magnetic fields for the barrel and end-cap muon detector spectrometers respectively. The layout of these magnet systems can be seen in figure 3.4. The detailed design specifications for the ATLAS magnet systems and a description of the mapping and careful calculations required in order to model the magnetic field are detailed elsewhere [41].

3.2.3.1 Solenoid

The central solenoid [51] measures 5.8 m in length and the inner and outer radii are 2.46 m and 2.56 m respectively. The solenoid is required to provide a 2 T magnetic field for the Inner

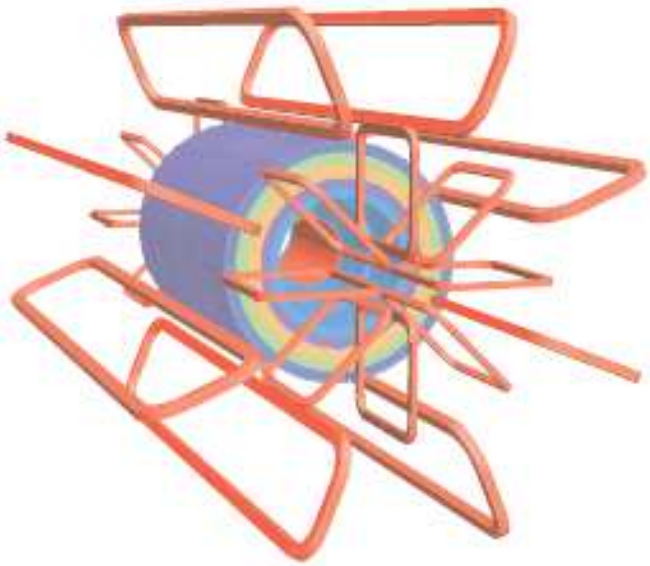

Figure 3.4: An illustration of the layout of the solenoid magnet within the calorimeter and the position of the eight toroid coils in the barrel and the eight toroid coils in each end-cap slid in between those of the barrel.

Detector while minimising the amount of material which is placed in front of the calorimeters. This is achieved by using a lightweight structure support and specially optimised material to provide a high strength magnetic field from minimal material. The solenoid also shares a vacuum chamber with the Liquid Argon calorimeter to further reduce the amount of material by eliminating an extra vacuum wall. The total solenoid and support structure reaches $\sim$0.66 interaction lengths [52].

3.2.3.2 Toroids

The toroidal magnet system is designed to provide strong bending power for the muon systems while remaining open and light to reduce multiple scattering effects and give better resolution in the precision muon chambers. The barrel toroid consists of eight coils, each inside an individual vacuum vessel, they are azimuthally symmetric. The end-caps slide inside the ends of the barrel and again each have eight coils positioned at equal spacing between those coils of the barrel toroid, as shown in figure 3.4. The barrel toroid is 25.3 m long, and the inner diameter of the coils is 9.4 m and the outer 20.1 m. The end-cap toroids are both 5 m long, with inner and outer

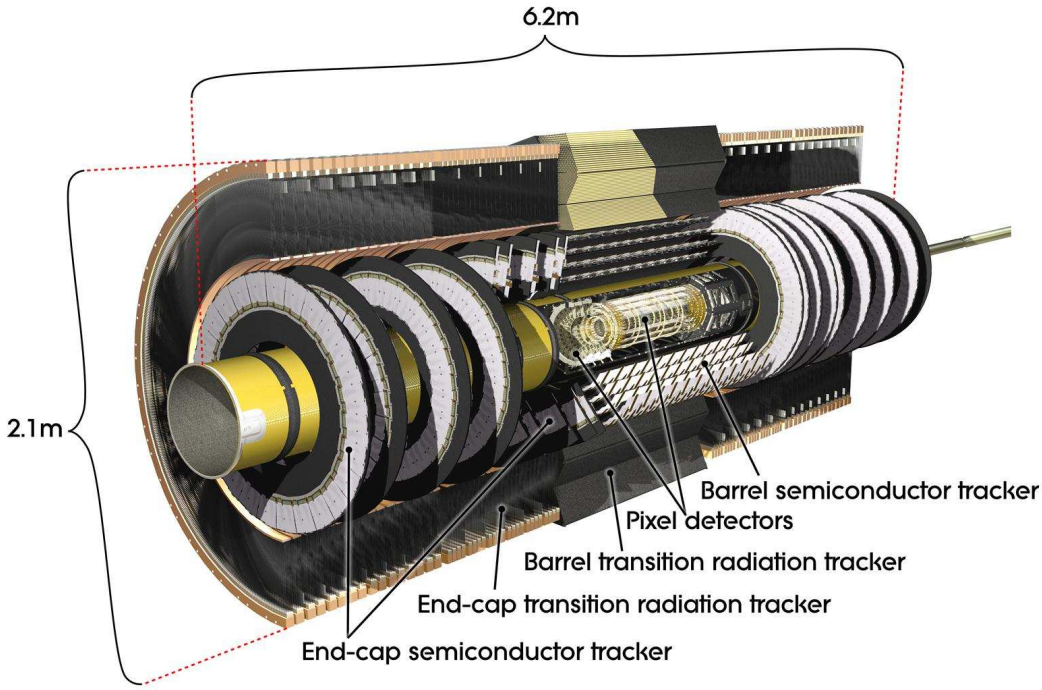

Figure 3.5: A schematic showing the relative positions of the three independent subsystems which comprise the ATLAS Inner Detector in the barrel and end-caps.

diameters of 1.65 m and 10.7 m.

3.2.4 Inner Detector

The Inner Detector consists of three complementary subdetectors. The silicon pixel detector [53] is closest to the beam pipe and affords the best momentum resolution; it is invaluable for secondary vertexing. The silicon microstrip tracker [54], along with the pixel detector offers high resolution pattern recognition. Covering the largest area is the transition radiation tracker [55], offering continued tracking and further options for electron identification. A schematic of the layout of the Inner Detector is shown in figure 3.5. The Inner Detector has a momentum resolution of $\sigma/p_T \sim 0.04\%\ p_T$ (GeV) $\oplus$ 1.5%. The primary vertex can be resolved using the Inner Detector with a resolution of 30μm in the transverse plane and 50μm in the longitudinal directional for events with greater than 70 tracks [56].

Both the pixel and silicon tracker detectors are built from silicon semiconductors, of n-type bulk, doped with p-type strips, with an electric-field applied across the chip. When an

electrically charged particle traverses a silicon detector, it produces pairs of electron-hole charge carriers along its trajectory. The electrons drift to the positively-charged backplane and the holes to the negatively-charged p-type strips; this induces an electrical current which can be detected and measured.

When a relativistic particle crosses a boundary between two materials with different dielectric constants it will produce transition radiation. The amount it produces depends on the γ factor of the particle, where $\gamma = {}^{E}/_{mc^2}$, therefore an electron will produce significantly more than any hadron, hence providing additional discrimination between the two via the use of low and high thresholds. As such a small amount of transition radiation is produced it is necessary to maximise the signal with many layers.The transition radiation is detected by the straw tubes.

3.2.4.1 Pixel Detector

The pixel detector is designed to have the highest granularity in both the $R - \phi$ and z directions; there are three layers in the barrel which will be traversed by each track giving three spacepoints, and three disks in each end-cap. There are approximately 80.4 million readout channels in total. The first layer is only 5cm from the beampipe and is essential for secondary vertexing, it is known as the b-layer.

The nominal size for each pixel is 50 $\times$ 400 μm^2 and the pixels are arranged in modules, of which there are 1744, where each module contains 47232 pixels corresponding to 46080 readout channels. Due to the high levels of irradiation expected over the lifetime of the detector the design of the pixel modules has to account for the radiation damage predicted. The pixel sensors are oxygenated n-type silicon wafers of thickness 250 μm^2, which when exposed to radiation over time will become p-type and the leakage current will increase, in a time-dependent manner. Therefore the pixel sensors are designed to be operated between -5°C and -10°C to reduce this leakage current and provide continued performance. The pixel detector has a resolution of $\sigma_{r\phi} \approx 10\mu$m in the $r - \phi$ direction and $\sigma_z \approx 115\mu$m in the z direction.

3.2.4.2 Silicon Tracking Detector

The Silicon Tracking detector (SCT) consists of four layers of silicon modules in the barrel and nine disks in each end-cap. There are a total of 4088 modules, each module containing four sensors of 770 microstrips of 12 cm length, two pairs of sensors are mounted at small stereo angles of 40 mrad in order to give accurate precision in both position coordinates. In the barrel one set of strips is oriented parallel to the beamline and the other at a small rotation, in the end-cap one set is oriented radially and the second at a small rotation; each pair of sensors comprises one spacepoint and therefore each charged track is expected to pass four spacepoints in any direction through the SCT detector. The SCT has a total of 6.3 million readout channels. The SCT detector has a resolution of $\sigma_{r\phi} \approx 17\mu$m in the $r-\phi$ direction.

3.2.4.3 Transition Radiation Tracking Detector

The Transition Radiation Tracker (TRT) detector in the barrel region is composed of three layers of modules. Each module is built from straws interspersed with plastic fibres which produce the transition radiation, absorbed by the Xenon-gas mixture in the straws. In the end-caps there are twenty independent wheels, each containing eight layers of straws layered between transition-radiation-producing plastic foils. Each straw contains a wire anode, of length 1.44 m in the barrel region and 0.37 m in the end caps. The 4 mm diameter casing surrounding each wire forms the cathode and the straws are filled with a Xenon-gas mixture. In the barrel region, the straws are all oriented along the beamline and can therefore only offer spatial resolution in the $R-\phi$ plane; only a loose determination of η is available for tracking. In the end-caps the straws are arranged radially and so offer resolution in the $z-\phi$ plane. In both the barrel and end-caps a charged track is expected to traverse 36 spacepoints, however in the transition region between the barrel and end-caps, $0.8 < |\eta| < 1.0$, the expectation drops to 22 spacepoints. The TRT detector has a resolution of $\sigma_{\perp} \approx 130\mu$m in the transverse direction.

3.2.5 Calorimeters

To measure jets and E_T^{miss} accurately, full coverage by the calorimeters is required. The ATLAS calorimeter system extends up to $|\eta| < 4.9$. To fulfil the varying requirements across the η range different components are used, these are shown in figure 3.6. In the $|\eta| < 2.5$ region matching the Inner Detector region, where tracking is available, precise measurements of electron and photon momenta are necessary along with accurate shower shape measurements. Both are required for the electron and photon identification as well as for accurate discrimination between the two. Outside this η range, the measurements can be made with a coarser granularity for the jet and E_T^{miss} reconstruction. The entire calorimeter had to be designed to be an appropriate depth to contain the electromagnetic and hadronic showers and reduce the punch through into the muon detectors, this had an important impact on the material choices. To meet these needs there is an electromagnetic calorimeter covering the barrel and end-cap regions, described in section 3.2.5.1, surrounded by a hadronic barrel calorimeter and two extended hadronic barrel calorimeters, two end-cap hadronic calorimeters and two hadronic forward calorimeters, described in section 3.2.5.2.

3.2.5.1 Liquid Argon Electromagnetic Calorimeters

The electromagnetic calorimeters are divided into a barrel calorimeter, composed of two halves with a small gap at $z = 0$, covering the range $|\eta| < 1.475$, and two end-cap calorimeters, each with an inner and outer wheel, where the the inner wheel covers $2.5 < |\eta| < 3.2$ and the outer wheel $1.375 < |\eta| < 2.5$. The electromagnetic calorimeters use liquid argon as the active material, chosen for its radiation hardness and speed, interleaved with layers of lead as the absorber. The geometry is accordion in shape as can be seen in figure 3.7, this ensures complete azimuthal coverage with no gaps and allows for three layers of active material in the region $0 < |\eta| < 2.5$ and two layers in the region not matching the tracking $2.5 < |\eta| < 3.2$, corresponding to the inner wheel. An additional layer of pre-sampler is placed in front of the

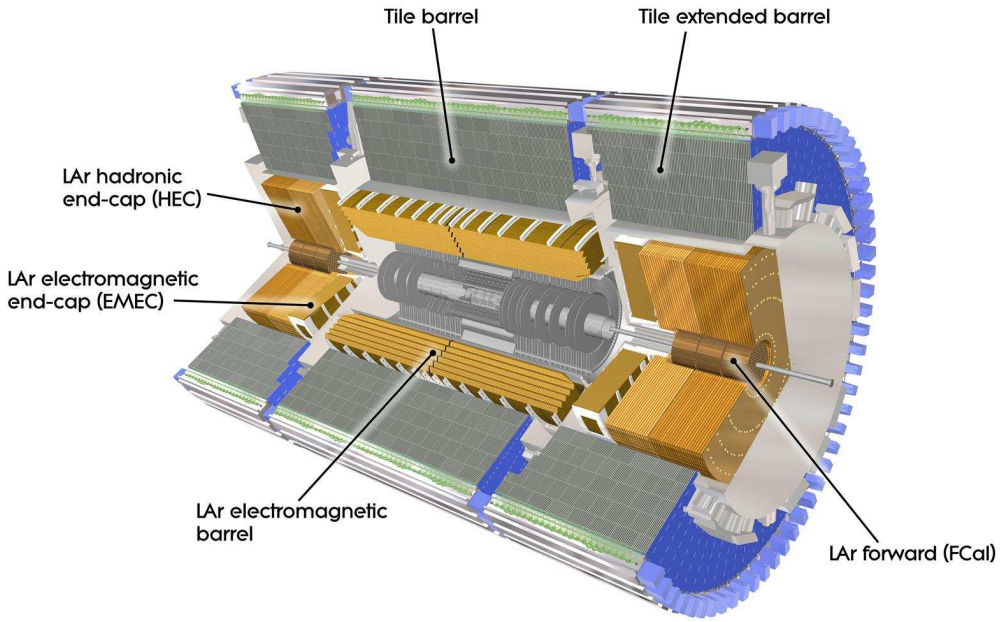

Figure 3.6: A view showing the various components which comprise the ATLAS calorimeter system for the barrel and end-caps.

calorimeter in the region $0 < |\eta| < 1.8$ to enable accurate measurements of the energy lost in the material in front of the calorimeters. The first layer is very finely granulated in the η direction, to give excellent resolution to complement the precision tracking; this is shown in figure 3.7. The electromagnetic calorimeter has an energy resolution of $\sigma/E \sim 10\%/\sqrt{E} \oplus 0.7\%$.

3.2.5.2 Hadronic Calorimeters

The hadronic calorimeter system is composed of one central barrel and two extended barrels covering the regions $|\eta| < 1.0$ and $0.8 < |\eta| < 1.7$ respectively, and two end-caps, each with two wheels, two layers in depth, covering the region $1.5 < |\eta| < 3.2$.

The barrel calorimeters use steel as the absorber and scintillating tiles as the active material, this was chosen to maximise the depth available while minimising the cost. Radially the hadronic calorimeter extends from 2.28 m to 4.25 m. The end-caps use copper plates as the absorber and liquid argon as the active material. The hadronic calorimeter has an energy resolution of $\sigma/E \sim 50\%/\sqrt{E} \oplus 3\%$.

Finally the full coverage over η is achieved using the forward calorimeters, these by neces-

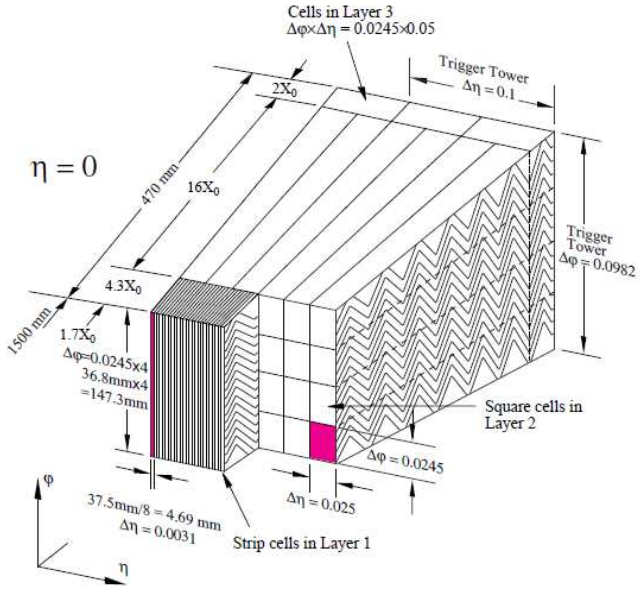

Figure 3.7: A figure showing the granularity of each layer of the electromagnetic calorimeter and the accordion geometry.

sity should be dense and so while using liquid argon as the active material, in the first layer copper plates are used for absorption, but in the second two layers tungsten is chosen. The copper is chosen to aid in heat removal and optimise resolution while the tungsten which is much heavier provides the required containment for the hadronic showering. The positioning of these forward calorimeters is pictured in figure 3.6. The forward calorimeters have an energy resolution of $\sigma/E \sim 90\%/\sqrt{E} \oplus 7\%$.

3.2.6 Muon Spectrometers

The muon spectrometers include chambers for accurate position and momentum measurement as well as dedicated triggering mechanisms. The muon trigger and measurement can achieve a momentum resolution of $< 10\%$ up to $E_\mu = 1$ TeV. The trigger can return a decision in tens of nanoseconds. The Monitored Drift Tubes (MDTs) are able to provide precision measurements of track position and momentum in the plane perpendicular to the bending induced by the toroidal magnet systems, described in section 3.2.3, for the region $0 < |\eta| < 2.7$. For the forward region in the innermost layer only, this capability is supplied by the Cathode Strip

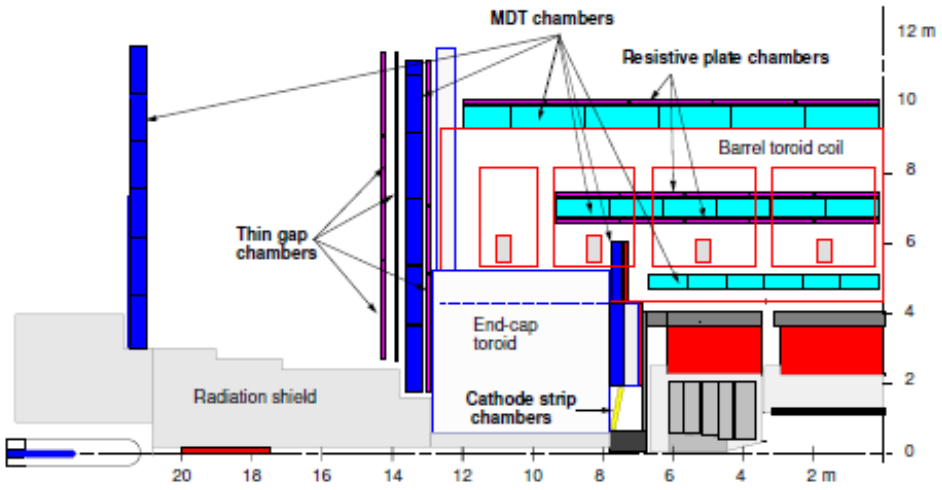

Figure 3.8: A diagram illustrating the layout of the ATLAS Muon Spectrometers.

Chambers (CSCs), because they are better able to cope with the higher rate, between $2.0 < |\eta| < 2.7$. The triggering is provided in the barrel region by the Resistive Plate Chambers (RPCs) for $|\eta| < 1.05$ and in the end-caps by the Thin Gap Chambers (TGCs) for $1.05 < |\eta| < 2.4$. The summary of this layout is shown in figure 3.8.

3.2.6.1 Monitored Drift Tube Chambers

The MDT chambers are designed primarily to achieve high precision tracking, they are capable of accurately measuring the momentum of muons and giving a position measurement in η the bending plane. In order to get the position in ϕ, the non bending plane, the track position in η is matched to the trigger chamber measurement, and then the position in ϕ is taken from the trigger chamber. Each of the 1088 MDT chambers is built from individual tubes for additional robustness and operational stability, these tubes are oriented along the ϕ direction, at a tangent to the beamline, in both the barrel and end-cap chambers. There are 18 different configurations of chamber, depending on location within the detector.

3.2.6.2 Cathode Strip Chambers

In the forward region $2.0 < |\eta| < 2.7$ the precision tracking in the innermost layer is much more challenging due to the higher rates and backgrounds and a different type of chamber is required to cope with this. The CSCs are multi-wire proportional chambers with wires oriented in the radial direction. The cathode strips are arranged in two layers, the first perpendicular to the anode wires and the second parallel to them in order to provide both directional components of the measurement. These chambers have better time and spatial resolution relative to the MDT chambers, and thanks to the 2D measurements they can also reliably resolve between two tracks, hence their suitability for this environment.

3.2.6.3 Trigger Chambers

The muon trigger chambers need fast time resolution to effectively tag bunch crossings and fast read out times of the order of tens of nanoseconds to enable use of the information in the trigger algorithms. They also have accurate spatial resolution, particularly in the non-bending plane, to complement the precision measurements made by the MDT chambers in the bending plane. The barrel and end-caps represent significantly different environments for the trigger system, the end-cap regions will receive a much higher flux of muons and be subject to higher backgrounds. In addition to this at higher values of $|\eta|$ the muons will have a higher momentum for a given p_T and the chambers will be outside of the magnetic field so the end-caps will require higher granularity for a similar precision to the barrel. The two different types of technology chosen for these applications are RPCs for the barrel and TGCs for the end-caps.

3.2.6.4 Resistive Plate Chambers

The barrel muon trigger system is divided into three layers at different radii, each layer contains two detectors and therefore a possibility of six position measurements. The chambers are built from two parallel electrode plates and no wires and can adequately deal with the expected rate

and provide the necessary spatial and temporal resolution for effective triggering.

3.2.6.5 Thin Gap Chambers

The trigger system in the end-caps uses four layers, three outside the toroid, and a fourth inside. Each layer is built of TGCs which are multi-wire proportional chambers, offering very good time resolution.

3.2.7 Trigger

The ATLAS trigger system is essential to reduce the high volume of data to a manageable rate which can be stored at CERN for data analysis; this is done by a wide range of different triggers designed to select a variety of interesting physics signatures.

A three-tier system is in use where each successive level refines the selection and further reduces the rate of data. The first level (L1) is realised using dedicated electronics and uses reduced granularity detector information. The decision must be made and passed to a central trigger processor (CTP) [57] within 2.5 μs, it reduces the rate from 40 MHz to 75 kHz.

The two higher levels, level 2 (L2) and the event filter level (EF), known collectively as the high level trigger (HLT), are software based triggers. L2 uses custom algorithms and EF uses algorithms similar to those used in offline reconstruction.

L2 uses Regions-of-Interest (RoIs), detector areas identified during the L1 selection, to seed its algorithms using reduced granularity detector information within these RoIs; this reduces the amount of data to be processed significantly and helps to keep the processing time to $\sim$40 ms/event. The rate input to the EF is kept under 3.5 kHz.

The EF is then able to use the full detector information and improved calibration, it can make much tighter selections due to the lower number of events to process, taking approximately 4 s per event; this final reduction brings the rate down to only 200 Hz and events passing this level are written to disk, with a size of $\sim$1.3 Mbyte.

Due to a wide range of physics needs many different trigger options are required; it is not

possible to meet the tight restrictions of rate for all possible triggers. Therefore a menu is devised, granting an allowed amount of bandwidth to each trigger. One available tool to reduce the rate for a particular trigger is to implement a pre-scale; a pre-scale is a scale factor which determines the percentage of events passing the trigger that are written to disk, it can be set independently at each level. As for a physics search it is undesirable to lose events in this manner, other possibilities to cope with the bandwidth problem are to raise the p_T threshold of the trigger, to use a combined trigger, where instead of triggering on an electron, for example, the trigger could fire when an electron and a muon are identified or to derive better trigger strategies with new cuts.

3.2.7.1 Level 1

The L1 trigger selects events containing high transverse momentum (p_T) physics objects: electrons, muons, photons, jets and hadronically decaying τ leptons, in addition to events with high total transverse energy (E_T) or missing energy (E_T^{miss}). This is achieved through two types of triggers: the L1 muon and the L1 calorimeter triggers.

L1 Muon The L1 muon trigger uses the trigger chambers described in section 3.2.6.3. For the end-cap these are the RPCs and for the barrel the TGCs. They are specially designed for high speed as well as accurate position and momentum resolution because the triggers need to be able to identify the bunch crossing the muon originated from; the timing for this is < 25 ns.

The trigger algorithm searches for high-p_T muons originating from the interaction point using coincidence techniques. There are 6 programmable p_T thresholds possible, three for the low-p_T region (< 10 GeV) and three for the higher-p_T region (> 10 GeV). For both the end-cap and barrel triggers, in the low-p_T region, 2 hits are required, in 2 different layers of trigger chambers, all of which must lie in one path, where the width of the path is proportional to the p_T threshold; for the higher-p_T region 3 hits in 3 layers are required.

L1 Calo The L1 calo triggers can be subdivided further into jet and energy, electron and photon, and τ lepton. All work with reduced granularity trigger towers; a sum of the energy in all calorimeter cells in a window measuring $\Delta\eta \times \Delta\phi = 0.1 \times 0.1$. These trigger towers are subjected to a sliding window algorithm to identify the highest energy clusters. For the electron and photon triggers the region used corresponds to $\Delta\eta \times \Delta\phi = 0.2 \times 0.2$. Once identified the cluster energies are then required to pass a pre-programmed E_T threshold. For the τ triggers the region is the same size but uses the hadronic calorimeters as well as the electromagnetic; for the jet triggers the size can be programmed to be $\Delta\eta \times \Delta\phi = 0.4 \times 0.4, 0.6 \times 0.6$ or 0.8×0.8.

For the electron, photon and τ triggers it is also possible to use a veto on isolation criteria, this is calculated using an annulus around the central high energy deposit within the Region-of-Interest. The highest energy window of towers of size 2×2 form the core, the RoI will be 4×4, so the isolation annulus is formed from the towers surrounding the core. This isolation veto affords much greater rejection against jets.

The L1 calo triggers count only the number of objects passing each threshold, however the geometric information of the object which passed the trigger becomes the RoI which is passed to the L2 trigger for further processing.

3.2.7.2 High Level Trigger

At the HLT, additional algorithms are run which provide information to multiple trigger types, such as tracking, calorimeter clustering and muon identification.

Since each trigger type, e.g. electron, muon, τ lepton, is designed to resemble offline selection as closely as possible within the time limit, they vary greatly. It is beyond the scope of this thesis to discuss the details of every trigger, which are documented elsewhere [58], with the exception of the trigger for hadronically decaying τ leptons which is discussed further in section 4.2.

3.3 Object Reconstruction and Identification

3.3.1 Tracking

In 25 ns at the LHC at 10^{34} cm^{-2} s^{-1}, ATLAS can expect to see as many as 1000 charged tracks. The challenge for the tracking algorithms is to accurately reconstruct the real tracks corresponding to the particle trajectories. For the Inner Detector the tracking process can be broken down into three steps:

3.3.1.1 Spacepoint Formation

The output from the pixel and SCT detectors is formed into clusters. One cluster from the pixel detector gives information on the $r-\phi-z$ direction, as each pixel gives two dimensions locally and this can be transformed to give three, creating a spacepoint. Each strip on the SCT detector will give a precise measurement in the strip direction only, it is for this reason that the strips are mounted back to back at a stereo angle as described in section 3.2.4.2, when these two hits are combined they give a two dimensional measurement locally and thus form a spacepoint. The timing information from the TRT detector is transformed into calibrated drift circles.

3.3.1.2 Trackfinding

Track seeds are formed from combinations of spacepoints, three in the three pixel barrel layers and one in the first SCT layer, clusters in the track seed are refitted as each SCT hit is added. This trackfinding seeded by spacepoints yields a very high number of track candidates, which must be resolved before the track can be extended into the TRT to include the calibrated drift circles. Tracks are subjected to quality scoring cuts to resolve ambiguities and a lower number of higher quality tracks result which can be extended into the TRT detector. The extended tracks are refitted and the quality scores re-evaluated. If they score lower than the original track, the original track is kept and the TRT hits added as outliers to the track. This is known as inside-

out tracking, a complementary track searching algorithm is used, known as outside-in tracking. This begins with the unused TRT track segments and extends these into the SCT and pixel detectors, this is specifically useful for tracks arising from conversions and secondary vertices, which are likely to fail the inside-out quality requirements due to a lack of hits in the inner layers.

3.3.1.3 Post-processing

There are many possible algorithms which follow on from the tracking, these involve finding the primary vertex, secondary vertexing and reconstruction of photon conversions.

3.3.2 Electrons

3.3.2.1 Reconstruction

The ATLAS reconstruction algorithm for electrons and photons is based on finding clusters of energy in the calorimeter and for electrons associating these clusters with tracks in the Inner Detector where possible. The clusters are formed using a sliding window algorithm [59] and are required to have energies > 2.5 GeV. The clusters are formed from 3×5 second layer cell units, where one unit is $\eta \times \phi = 0.025 \times 0.025$ [60].

The matching of the track to the cluster is done by extrapolating the track from its last measured point in the Inner Detector to the second layer of the calorimeter where the majority of the energy is expected to be deposited. The difference between the expected impact parameter on the calorimeter in η and ϕ is compared to the cluster position and the track with the lowest ΔR (equation 3.2) is chosen as the selected track. All the other tracks are ordered according to the quality of the track match and stored, as are all variables calculated during the track to cluster matching process. Track segments only in the TRT, with no matching silicon track (known as TRT-only tracks), have a lower priority than those built from silicon hits as TRT-only tracks have a higher likelihood of being electrons from photon conversions.

At the reconstruction level the electrons from conversions will look identical to isolated electrons, a track pointing to a cluster of energy, hence at this stage to preserve the efficiency of reconstructing isolated electrons, the electrons from conversions are stored and treated as electrons and instead can be distinguished using the electron identification algorithm, in particular at the "tight" level, see section 3.3.2.2.

For the track matching, care is taken to account for Bremsstrahlung losses by the electrons by enlarging the size of the $\Delta\phi$ window on the side that the track bends as it passes through the magnetic field. If the track contains only TRT hits the matching can only be performed in $\Delta\phi$ due to the limited precision the TRT affords in the measurement of the η direction.

3.3.2.2 Identification

The ATLAS electron identification algorithm is designed to discriminate real isolated electrons from hadrons in jets from QCD processes, photons from electron conversions and non-isolated electrons from heavy flavour decays. It uses a combination of calorimeter, tracking and combined calorimeter and tracking variables to achieve this. Three levels are defined which correspond to the level of background rejection in order to accommodate the needs of different analyses, "loose", "medium" and "tight" [60].

For the "loose" selection, shower shape variables and hadronic leakage variables are used. At the "medium" level calorimeter cuts, track quality requirements and track-cluster matching criteria are used in addition to the "loose" selection requirements. For the "tight" level, cuts on E/p, a requirement of a hit in the b-layer and cuts based on TRT particle discrimination between electrons and photons are added to the "medium" level.

The variables used in "loose" level identification are: R_{had1}, R_{had}, ω_{η^2} and R_{η}. These are defined in table 3.3.

The variables used in the "medium" level also include the calorimeter variables ω_{tot} and E_{ratio}, also defined in table 3.3. The tracking variables added at this level were optimised on the first data. These are: Minimum numbers of hits in the pixel and SCT detectors and a

maximum value of the transverse impact parameter of the electron with respect to the beam spot d_0. The track-cluster matching is subject to the quality requirement of a maximum cut on $\Delta\eta_1$, the $\Delta\eta$ between the cluster and extrapolated track. All of these variables are defined and summarised in table 3.3.

The "tight" level identification adds the requirement of at least one hit in the b-layer as well as a dedicated algorithm for rejecting conversions. The track quality is improved by a tighter cut on the transverse impact parameter and more stringent requirements on the track-cluster matching are added, including additional cuts on $\Delta\phi$ between the track and cluster and a cut on the cluster energy E upon the track momentum p, and a tighter cut on $\Delta\eta_1$. The TRT cuts used are: total number of hits in the TRT detector and the ratio of high-threshold hits to total hits. These variables are defined and summarised in table 3.3.

3.3.3 Muons

There are four types of muon candidates reconstructed at ATLAS: Standalone, Combined, Segment Tagged and Calorimeter Tagged. The tracking algorithms used by the Muon Spectrometer are common to the Inner Detector and are described in section 3.3.1. For the types of candidates which use tracks from the Muon Spectrometer there are two different chains of algorithms available, they use different pattern recognition and different techniques to combine the tracks between the Inner Detector and Muon Spectrometer, these are Staco [61] and Muid [62].

Standalone Standalone muons are formed from tracks reconstructed in the Muon Spectrometer, extrapolated back to the beampipe, correcting for the expected energy losses in the calorimeter. As these standalone muons use no Inner Detector information, they are available up to $|\eta| < 2.7$. However they are missing in the η region around zero, where an accurate momentum measurement cannot be made due to the gap in muon detector coverage owing to the services access, such as for power supplies, cabling and cooling pipes. Standalone muons require track segments in at least two layers in order to calculate an accurate momentum measurement, there-

Type	Description	Variable Name
	"Loose" cuts	
Acceptance of the Detector	• $\|\eta\| < 2.47$	
Hadronic Leakage	• Ratio of E_T in the first layer of the hadronic calorimeter to E_T of the EM cluster (used over the range $\|\eta\| > 0.8$ and $\|\eta\| < 1.37$) • Ratio of E_T in the hadronic calorimeter to E_T of the EM cluster (used over the range $\|\eta\| > 0.8$ and $\|\eta\| < 1.37$)	• R_{had1} • R_{had}
Second Layer of EM Calorimeter	• Ratio of η of cell energies in 3 x 7 versus 7 x 7 cells • Lateral width of shower	• R_η • ω_{η^2}
	"Medium" cuts (includes "Loose")	
First Layer of Calorimeter	• Total shower width • Ratio of the energy difference associated with the largest and second largest energy deposit of the sum of these energies	• ω_{stot} • E_{ratio}
Track Quality	• Number of hits in the pixel detector (≥ 1) • Number of hits in the pixels and SCT (≥ 7) • Transverse impact parameter (< 5 mm)	• d_0
Track Matching	• $\Delta\eta$ between the cluster and the track (< 0.01)	• $\Delta\eta_1$
	"Tight" cuts (includes "Medium")	
b-Layer	• Number of hits in the b-layer (≥ 1)	
Track Matching	• $\Delta\phi$ between the cluster and the track (< 0.02) • Ratio of the cluster energy to the track momentum • Tighter $\Delta\eta$ cut (< 0.005)	• $\Delta\phi_2$ • E/p • $\Delta\eta_1$
Track Quality	• Tighter transverse impact parameter cut (< 1 mm)	• d_0
TRT	• Total number of hits in the TRT • Ratio of the number of high-threshold hits in the TRT	
Conversions	• Electron candidates matching to reconstructed photon conversions are rejected	

Table 3.3: This is a summary of the variables used for each level of electron identification and their definitions for the central region of the detector $|\eta| < 2.47$ [60].

fore losses can occur at lower momentum, ∼6 GeV, where muons do not pass more than the innermost layer of muon chambers.

Combined Combined muons are computed using tracks reconstructed in the Inner Detector and Muon Spectrometer, combined using one of the two chains to produce a quality matched track. This can provide a more accurate measurement of momentum thanks to the information from the Inner Detector, however they are only available up to $|\eta| < 2.5$.

Segment Tagged Segment tagged muons begin from an Inner Detector track and are extrapolated to the first muon layer, where the track is matched with straight sections from inside a MDT or CSC chamber. This is particularly useful for recovering low-p_T muons, which may not extend past the first layer and be reconstructed as a full Muon Spectrometer track.

Calorimeter Tagged Calorimeter tagged muons also start from an Inner Detector track and search for matching energy deposits in the calorimeter which agree with those expected by a minimum ionising particle. This can be useful for covering the region $|\eta| = 0$ where there is a gap in coverage with all candidates requiring any Muon Spectrometer segments.

3.3.4 Hadronically Decaying τ Leptons

The τ leptons decay leptonically to an electron $\sim$17.8 $\%$ ($\sim$17.4 $\%$) (muon) of the time, and hadronically $\sim$64.7 $\%$ of the time, therefore it is very important to develop techniques for reconstructing and identifying the hadronic decays. This is very challenging in an environment such as is produced at the LHC due to the multijet background which has a cross-section many times larger than the signal processes (for example the jet production cross-section is $\sim 4 \times 10^3$ nb for inclusive jets with $p_T > 60$ GeV and $|\eta| < 2.8$ at $\sqrt{s} = 7$ TeV [63] and the production cross-section for $Z \to \tau\tau$ is just 0.96 nb at $\sqrt{s} = 7$ TeV [64]). The branching ratio for decays to "1-prong" τ leptons (one charged track) is 49.5 $\%$ and to "3-prong" (three charged tracks) τ leptons is 15.2 $\%$. While "5-prong" decays will also occur these are typically too difficult to distinguish from the multijet background. This signature of low track multiplicity is a key feature for identifying hadronically decaying τ leptons. Another is that the visible decay products of

the τ leptons will be collimated due to the boost the τ leptons typically receive when produced; this results in narrow, isolated deposits of energy in the calorimeter.

3.3.4.1 Hadronically Decaying τ Lepton Reconstruction

The reconstruction for hadronically decaying τ leptons is seeded by jets reconstructed in the calorimeter using the Anti-k_T algorithm [65, 66] (see section 3.3.5.1) using a distance parameter of $\Delta R = 0.4$, built from topoclusters [59] (see section 3.3.5.1) in the calorimeter. These seeds are then matched to tracks identified using the Inner Detector. As the τ decay products are expected to be collimated the tracks must be in a core cone of $\Delta R < 0.2$ and pass the following quality requirements:

- $p_T > 1$ GeV
- Number of hits in pixel b-layer ≥ 1
- Number of pixel hits ≥ 2
- Number of pixel + SCT hits ≥ 7
- Transverse impact parameter, $|d_0| < 1.0$ mm
- Longitudinal impact parameter multiplied by $\sin\theta$, $|z_0 \sin\theta| < 1.5$ mm

An annulus surrounding the core cone of $0.2 < \Delta R < 0.4$ is defined as the isolation annulus; tracks which fall in this region are stored and used for the identification, but the definition of a τ candidate as being single or multi-prong depends only on the number of tracks in the core cone.

The directional components η and ϕ of the reconstructed τ candidate are taken from the seed jet, the mass is assumed to be zero, therefore the transverse momentum and transverse energy are equal. The energy of the reconstructed τ candidate is not taken from the seed jet as this has been calibrated to non-τ jets [67]. Instead, all cells which contribute to the topoclusters

within $\Delta R < 0.4$ are summed at the electromagnetic scale and then this sum is calibrated to the tau energy scale [45]. The τ candidates are calibrated based on calorimeter response functions measured in Monte Carlo for hadronically decaying τ leptons.

3.3.4.2 Hadronically Decaying τ Lepton Identification

There are three types of identification available, a simple cuts-based selection, a projective likelihood and one using boosted decision trees. In this thesis only the cuts-based selection is applied, so a brief introduction to this is included here and the details for the two multi-variate identifications are documented elsewhere [45].

The cuts-based selection described here was optimised using Monte Carlo simulation of both $W \to \tau\nu$ and $Z \to \tau\tau$ generated with PYTHIA, and the background was taken from ATLAS data collected in 2010 at $\sqrt{s} = 7$ TeV. The identification is optimised for signal efficiency against the background efficiency of a di-jet sample, the rejection of electron type candidates is dealt with separately using a dedicated electron veto [58], described in section 3.3.4.3. As the p_T of the τ lepton increases and it becomes more boosted the decay products become more collimated and the efficiencies of those variables which describe the shower width, in particular R_{EM} (equation 3.3), illustrate dependence on p_T. Therefore in addition to optimisation in bins of single or multi-prong candidates, the identification is also optimised in bins of p_T to attempt to flatten this dependence. The optimisation of the τ identification defines different levels for the identification, for example where "tight" defines the highest rejection against the multijet background and refers to $\sim$30 % signal efficiency. The three variables used for the cut-based identification are:

1. The *EM-radius* is the E_T-weighted average ΔR among all calorimeter cells,

$$R_{\mathrm{EM}} = \frac{\sum E_T \, \Delta R}{\sum E_T} \tag{3.3}$$

The sums are over calorimeter cells in the presampler and first two layers of the EM

calorimeter within $\Delta R < 0.4$ of the axis of the seed jet. *EM-radius* quantifies the spatial narrowness of the τ candidate and is p_T-dependent.

2. The *track-radius* is the p_T-weighted average ΔR among tracks associated to the τ candidate,

$$R_{\text{trk}} = \frac{\sum p_T \, \Delta R}{\sum p_T} \tag{3.4}$$

The sums are over tracks associated to the τ lepton candidate within $\Delta R < 0.4$ of the axis of the seed jet. *track-radius* quantifies the spatial narrowness of the τ candidate and is dependent on the p_T of the τ lepton.

3. The *leading track momentum fraction*,

$$f_{\text{trk},1} = \frac{p_T(\text{leading track})}{p_T(\tau_{\text{h}})} \tag{3.5}$$

is the ratio of the transverse momentum of the highest p_T track to the total reconstructed transverse momentum of the τ candidate, calibrated at EM-scale (see section 3.3.5.1).

3.3.4.3 Hadronically Decaying τ Lepton Electron Veto

Many backgrounds to τ lepton final states contain electrons, these can be falsely reconstructed as τ lepton candidates. To ensure efficient rejection of these backgrounds, for example from $W \to e\nu$ or $Z \to ee$ processes, tracks which would pass identification requirements as electrons are vetoed. The algorithm designed to do this is known as the τ-electron veto [58]; it uses the following variables:

- Energy deposited in the hadronic calorimeter
- Energy in the first layer of the electromagnetic calorimeter not associated with the charged track
- Ratio of the E_T in the electromagnetic calorimeter to the p_T of the track
- Ratio of high-threshold to low-threshold TRT hits

3.3.5 Jets and E_T^{miss}

3.3.5.1 Jet Reconstruction

The default jet finding algorithm was chosen based on a set of guidelines [58] produced between the experimental and theoretical communities to ensure good comparability between different results. At the ATLAS experiment the recommended jet reconstruction algorithm is Anti-k_T [65, 66], using a distance parameter of either $\Delta R = 0.4$ or 0.6.

The Anti-k_T algorithm is a fast sequential recombination algorithm which is infrared and collinear safe and includes the property of regular shaped jets.

The inputs to this jet algorithm are 3D topological clusters (topoclusters) [59]. Topoclusters are built from a clustering algorithm which iteratively adds neighbouring cells which pass an energy threshold and therefore inherently includes noise suppression.

The default calibration for anti-k_T jets is currently at the electromagnetic scale, this means the calibration used was determined from the response of the calorimeters to electrons and photons in test-beam data. It is at this stage that these jets reconstructed with a distance parameter of $\Delta R = 0.4$ are taken as inputs to the reconstruction of hadronically decaying τ leptons, as described in section 3.3.4.1. For jets there is an additional correction available to calibrate the jets on a jet-by-jet basis to the hadronic scale, for which the calibration is derived from Monte Carlo simulations of the calorimeter response to hadrons; it is parametrised in terms of jet p_T and η [67].

3.3.5.2 E_T^{miss} Reconstruction

E_T^{miss} stands for missing transverse energy; in any collision energy should be conserved according to the conservation of energy principle. It is not possible to measure total energy, as the contribution lost longitudinally along the beampipe cannot be measured; so instead the energy is measured in the transverse direction. The E_T^{miss} is then the imbalance of energy in the transverse direction.

The hard process and all other background components which will contribute to the E_T^{miss} in an event such as multiple interactions, pile-up and noise are characterised as energy deposits in the calorimeter and muon tracks. The E_T^{miss} is reconstructed from the calorimeter cells and muon tracks using a cell-based algorithm. All cells in the event which are included in topoclusters and therefore have already passed noise suppression are summed. The topoclusters are classified into types of reconstructed objects, and then can be calibrated to the appropriate energy scale, electromagnetic or hadronic. Once the calorimeter deposits are summed, the contributions from muon tracks are included and the calorimeter deposits are corrected for the energy arising from muons traversing the calorimeter [68].

Chapter 4

Tau Trigger Studies

4.1 Tau Trigger Performance

At the LHC, where the rate of collision data is 40 MHz, it is essential to select only events of interest to record and analyse. Hadronically decaying τ leptons are an interesting key signal for many new physics processes, such as Higgs boson decays or Supersymmetry. Having the ability to trigger on an event containing a hadronically decaying τ lepton as well as one containing a leptonically decaying τ lepton greatly increases the potential sample of new physics events thanks to the higher branching ratio of the τ lepton to hadrons, discussed in section 2.1.1.

The task of triggering events is further complicated by the presence of additional collisions in every bunch crossing; at the design luminosity of 10^{34} cm^{-2} s^{-1}, 23 minimum bias events are expected per bunch crossing, of which only one is likely to be a hard collision resulting in a process of interest, the rest are known as "in-time" pile-up; where "out-of-time" pile-up refers to collision data from nearby bunch crossings. An example of the difficulty posed for triggering is shown in figure 4.1 where a $Z \rightarrow \mu\mu$ event recorded on September 14^{th} 2011 is pictured with 20 reconstructed vertices.

The ATLAS trigger system is described in section 3.2.7 and further details specific to the design and implementation of the Tau Trigger can be found in section 4.2.

This study was a first look at the potential degradation of the trigger performance in pile-up conditions. It was undertaken prior to collisions at the LHC and therefore before the successful commissioning of the ATLAS Tau Trigger with collision data at $\sqrt{s} = 900$ GeV [69] and $\sqrt{s} = 7$ TeV [70]. Therefore it is performed entirely using Monte Carlo.

The performance of the Tau Trigger is assessed by measuring its efficiency. In order to eval-

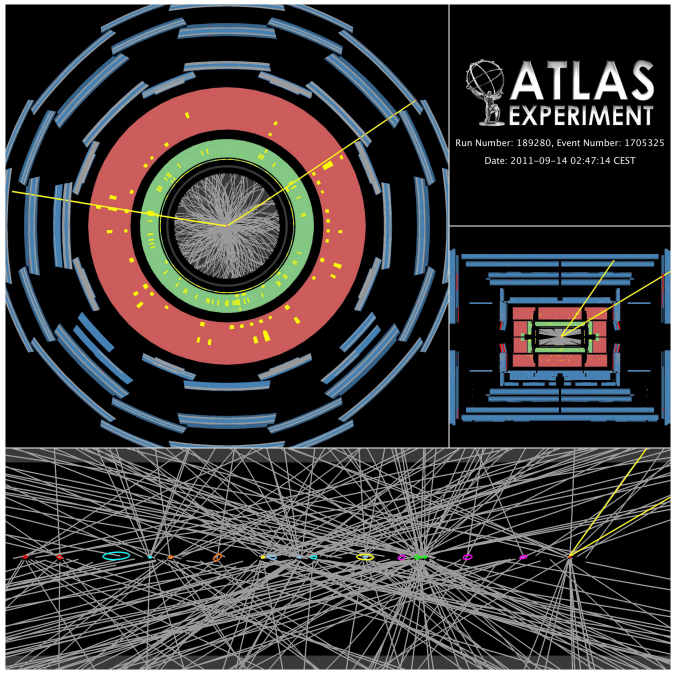

Figure 4.1: ATLAS event display of a $Z \rightarrow \mu\mu$ event recorded on September 14^{th} 2011 with 20 reconstructed vertices. This is a typical occurrence in the high luminosity environment. Tracks were required to have $p_T > 0.4$ GeV and at least 2 hits in the Pixel detector and 7 in the SCT.

uate the impact of additional activity in proximity to the τ lepton, the efficiency is parametrised in the distance measurement ΔR (given in equation 3.2) between the τ candidate and the nearest jet in samples of $t\bar{t}$ events.

4.2 Overview of the Tau Trigger

4.2.1 Level 1

At Level 1(L1) a hardware trigger is used, based on trigger towers, which are sums of calorimeter cells in the Electromagnetic (EM) and Hadronic (HAD) calorimeters, with granularity $\Delta\eta \times \Delta\phi = 0.1 \times 0.1$. From these a Region-of-Interest (RoI) is formed of 2×2 towers. A local maxima in E_T is found in the core region of 2×2 trigger towers using a sliding window algorithm. As illustrated in figure 4.2 horizontal and vertical sums of energies are calculated and various quantities are formed and compared to pre-programmed thresholds.

The quantities calculated are:

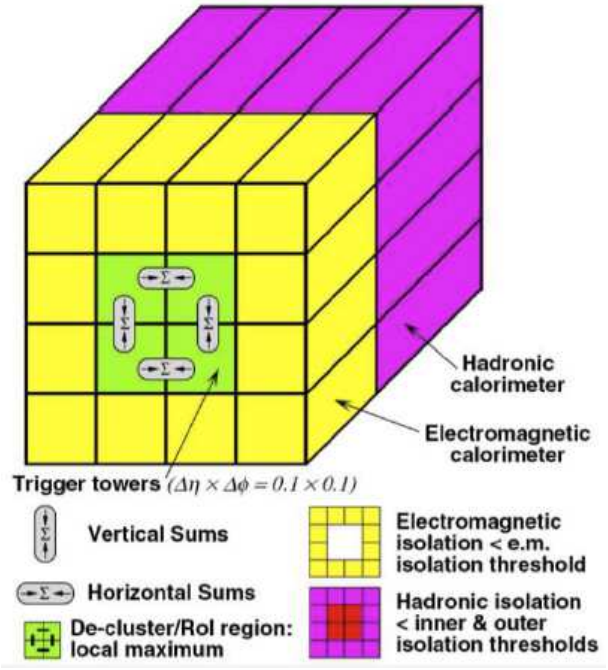

Figure 4.2: Diagram showing the different calculations used in the Level 1 Calorimeter trigger.

- **EMCore**: The energy in the central 2×2 trigger towers in the EM calorimeter
- **HadCore**: The energy in the central 2×2 trigger towers in the HAD calorimeter
- **EMEnergy**: The highest energy in a horizontal sum of 2×1 or a vertical sum of 1×2 EM trigger towers
- **TauEnergy**: The EMEnergy added to HadCore
- **EMIsolation**: The energy in the region between 2×2 and 4×4 towers in the EM calorimeter
- **HadIsolation**: The energy in the region between 2×2 and 4×4 towers in the HAD calorimeter

For an example of the pre-programmed thresholds for these variables see table 4.4 which gives the default values for the tau16i trigger, a baseline trigger, named for its p_T threshold of 16 GeV and i indicates that the configuration includes isolation criteria.

4.2.2 Level 2

At Level 2 (L2) the trigger is seeded by the L1 RoI, it is able to use the full detector granularity in this region and fast specialised algorithms with tracking in the Pixel and SCT detectors to calculate a series of variables using both the calorimetry and the tracking.

Calorimetry variables The second layer of the EM calorimeter is used to refine the position of the candidate, then shape variables can also be calculated, lastly the total energy of the candidate is recalculated for L2 by summing the energy of all the layers in the EM and HAD calorimeters and applying an energy calibration.

To calculate the shape variables, only the second layer of the EM calorimeter is used as the majority of the energy is deposited there; three window sizes are defined: $\eta \times \phi = 0.1 \times 0.1$ - small, $\eta \times \phi = 0.2 \times 0.2$ - medium, and $\eta \times \phi = 0.3 \times 0.3$ - large.
The variables are defined as:

- **StripWidth**: The width of the energy deposition:

$$\mathrm{StripWidth} = \sqrt{\frac{\sum\limits_{large} \eta_{cell}^2 . E_{cell}}{\sum\limits_{large} E_{cell}} - \left[\frac{\sum\limits_{large} \eta_{cell} . E_{cell}}{\sum\limits_{large} E_{cell}}\right]^2} \tag{4.1}$$

- **EMRadius**: The energy weighted squared radius of the energy deposition:

$$\mathrm{EMRadius_{L2}} = \frac{\sum\limits_{large} E_{cell} \Delta R_{cell}^2}{\sum\limits_{large} E_{cell}} \tag{4.2}$$

- **IsoFrac**: The difference in energy between the small and medium windows normalised to the medium window:

$$\mathrm{IsoFrac} = \frac{\sum\limits_{med} E_{cell} - \sum\limits_{small} E_{cell}}{\sum\limits_{med} E_{cell}} \tag{4.3}$$

- **Calibrated** η: Sum of the energy in all calorimeter layers, EM and HAD in a large window,

calibrated

Tracking variables Using the common L2 tracking algorithm the L2 trigger reconstructs tracks in an area $\eta \times \phi = 0.6 \times 0.6$ around the calorimeter central position with a $p_T > 1.5$ GeV requirement. The highest p_T track is selected as the leading track, two cones are defined at $\Delta R = 0.15$ and $\Delta R = 0.3$ and the region between these is known as the isolation region.

- **NTracks**: Number of tracks found in the $\Delta R = 0.3$ cone
- **Leading Track** p_T: p_T of the Leading Track
- **Charge**: The absolute sum of the charge of all tracks in the $\Delta R = 0.3$ cone
- **SumPtRatio**: Ratio of the sum of the p_T of all tracks in the isolation region to the cone of $\Delta R = 0.15$

4.2.3 Event Filter

The Event Filter (EF) follows the offline reconstruction algorithms more closely; it uses an area around the L2 RoI to collect cells in $\eta \times \phi = 0.6 \times 0.6$ which offers more accurate direction determination. Tracking is performed in an area of $\eta \times \phi = 0.4 \times 0.4$; if there are multiple tracks, secondary vertexing can be performed. At EF calibration following offline procedures is applied to the τ candidate.

The variables calculated at the EF level are:

- **NTracks**: Number of tracks in a cone of $\Delta R = 0.2$ with $p_T > 2$ GeV
- **EMRadius**: An energy weighted radius of the transverse energy in the first three layers of the EM calorimeter:

$$\mathrm{EMRadius_{EF}} = \frac{\sum\limits_{large} E_{T,cell} \Delta R_{cell}}{\sum\limits_{large} E_{T,cell}} \tag{4.4}$$

- **IsoFrac**: The sum of energy in an annulus between $0.1 < \Delta R < 0.2$ divided by the energy

in a cone of $\Delta R = 0.3$:

$$\text{IsoFrac} = \frac{\sum\limits_{0.1<\Delta R<0.2} E_{cell}}{\sum\limits_{\Delta R=0.3} E_{cell}} \tag{4.5}$$

- **Leading Track** p_T: p_T of the Leading Track in a cone of $\Delta R = 0.2$
- **Calibrated** E_T: Total energy in a cone of $\Delta R = 0.3$ in all layers of the EM and HAD calorimeters with a calibration applied

4.3 Simulation Samples

This study was performed using the TrigTauPerform (TTP) package, designed by the Tau Trigger working group for validation, optimisation and performance studies on the trigger. As well as including the fully simulated trigger decisions it emulates the trigger to enable the user to change the cuts.

At the time this study was undertaken, no samples including pile-up were available, therefore to approximate a busy environment a $t\bar{t}$ sample was used; it is a reasonable proxy because it contains at least two b-jets and the possibility of other jets from $W \rightarrow q\bar{q}$. The study was undertaken using Monte Carlo simulated using the MC@NLO generator [71] at a centre of mass energy of $\sqrt{s} = 14$ TeV.

In the $t\bar{t}$ events in the Monte Carlo sample used, the two top quarks decay to W bosons and b quarks, one W boson decays leptonically to an e, μ, or τ lepton and the other is free to decay leptonically or hadronically. In figure 4.3 the topology of this event shows that there will usually be a jet from the b quark in proximity to the τ candidate since the W and the b-quark typically decay collinearly, as well as any other jets that may be present from the underlying event. The events selected for this study include at least one hadronically decaying τ from a W boson.

This will not be a totally effective proxy for real pile-up events, but the ability to be able to classify performance as a function of proximity to jets is useful.

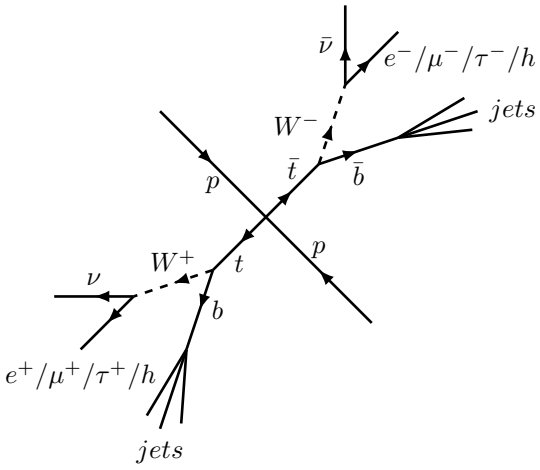

Figure 4.3: Schematic of a $t\bar{t}$ event where each W boson can decay to either a lepton and a neutrino or to hadrons.

4.4 Efficiency Measurement

4.4.1 Definition of Efficiency

For the purpose of this study let us define two types of efficiency measurement, the first is more widely used and shall be known as "relative efficiency", defined in equation 4.6; this measures the trigger efficiency relative to the offline reconstructed τ leptons and therefore a measure of only the efficiency of the trigger. Changing a cut may not necessarily improve the efficiency when measuring relative to the offline if the cut is already applied in the offline selection; therefore another definition is useful. This shall be known as "absolute efficiency" and is defined in equation 4.7; it is a measure of the efficiency of the trigger with respect to the truth level. It decouples the trigger selection from the offline selection and highlights the full effect of the cuts. This could potentially show recovery of τ candidates not selected at the offline level.

$$\varepsilon_R = \frac{N_{\text{trigger candidates}}}{N_{\text{offline taus}}} \tag{4.6}$$

$$\varepsilon_A = \frac{N_{\text{trigger candidates}}}{N_{\text{truth taus}}} \tag{4.7}$$

4.4.2 Tau Selection

Truth τ candidates The truth τ leptons were selected with the requisites: a W boson as parent; visible $p_T > 10$ GeV (i.e. the sum of the decay products excluding the neutrinos) and visible $|\eta| < 2.5$.

Offline τ candidates At the time of this study two algorithms for reconstructing hadronically decaying τ leptons were available. The first, tauRec [58], a calorimetry-based algorithm, identified EM and HAD calorimeter cluster deposits as seeds and built a τ candidate incorporating information from Inner Detector tracking. The second, tau1p3p [58], a tracking-based algorithm, used a low number of collimated selected tracks as a seed and built a τ candidate incorporating calorimeter information; it was possible for a τ candidate to have both seeds. Reconstructed offline τ candidates were then required to pass identification requirements which were seed-type dependent. Candidates seeded by tauRec alone or both seeds, with 1 track, had to have a Likelihood [72] value > 2.2, for any other number of tracks they had to have Likelihood > 4.8. Candidates with a tau1p3p seed or both seeds were required to have a cut based DiscriCut [72] value of > 0.5.

Matching of τ candidates Identified reconstructed offline τ candidates were matched to selected truth τ candidates within $\Delta R < 0.2$. Trigger candidates were matched to the selected truth τ at L1 with $\Delta R < 0.15$, at L2 with $\Delta R < 0.1$ and at EF with $\Delta R < 0.1$.

4.4.3 Efficiency Measurement Methods in Data

During data taking the efficiency measurement has to be carried out in a different way; there are three methods for doing this:

- “Tag and Probe” - An event containing two similar objects is used, one object is used to trigger the event and the other can then be studied.
- “Orthogonal Trigger method” - An event is triggered on a different object such as missing transverse energy and this sample can be used to measure the efficiency of the Tau Trigger.
- “Bootstrap method” - A trigger with simply a lower threshold is used to trigger events giving a sample with which to measure the efficiency of the higher threshold trigger.

4.5 Parton Matching

4.5.1 Calculating ΔR

To assess the proximity of the τ lepton in $t\bar{t}$ events to jets, ΔR was calculated between each jet and each τ lepton; a distribution of ΔR between all jets and all τ candidates is shown in figure 4.4(a). The closest jet in ΔR was then selected and this value is plotted in figure 4.4(b) for each offline τ lepton, where there may be more than one offline τ lepton per event.

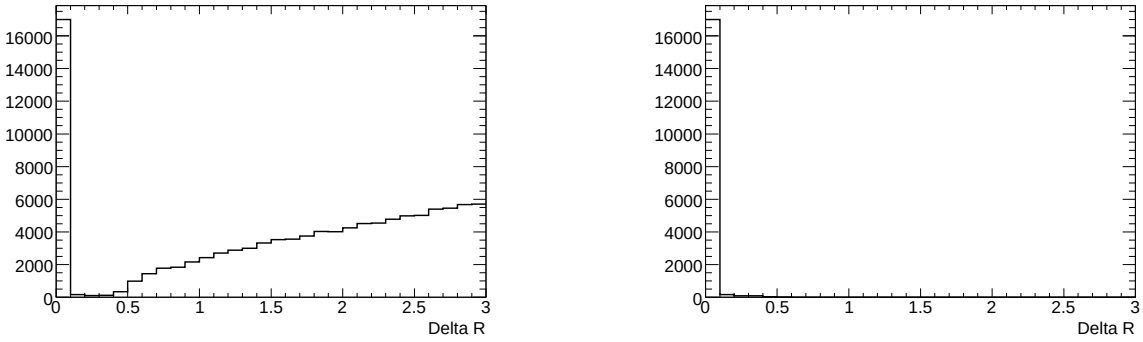

(a) Delta R between offline τ lepton and each jet

(b) Delta R between offline τ lepton and closest jet

Figure 4.4: Distributions between τ leptons and offline jets.

The peak at $\Delta R < 0.1$ as seen in figure 4.4(b) arises since the τ leptons themselves are reconstructed as jets. Figure 4.4(a)shows that the values of ΔR between each jet in each event and each offline τ lepton are spread throughout the range of ΔR. The algorithm used to reconstruct offline jets was a cone algorithm with conesize of $\Delta R = 0.4$ [58].

It is very difficult to resolve whether a jet falling in the region of $\Delta R < 0.1$ is a genuine overlapping jet or the τ lepton itself reconstructed as a jet; obviously there is a mixture of both. Due to this difficulty, this region was not studied here and instead the focus lies in the region $0.1 < \Delta R < 1.0$. In all plots where efficiency has been plotted against p_T a veto was placed on jets at less than $\Delta R = 0.1$.

This is clearer when the efficiency of the Tau Trigger is plotted against ΔR between the τ lepton and its closest jet; when $\Delta R < 0.1$ the efficiency was higher than at slightly larger values of ΔR, for example $0.1 < \Delta R < 0.5$, after that it began to rise again. The higher efficiency at values of $\Delta R < 0.1$ further consolidates that many of these jets are in fact τ leptons. This feature can be seen in figure 4.5(b).

4.5.2 b-quark Matching

One way to use genuine overlapping jets in the simulation is to match the jets to partons. b-quark jets are expected to be close to the τ leptons, shown in the topology in figure 4.3. This study matched jets to b-quarks in the event, these jets were then labelled as 'b-jets'; the relative efficiency for the Tau Trigger combined over all trigger levels was plotted against ΔR between each selected truth τ and its closest b-jet in the event, for the events which contain a selected truth τ and a b-jet. The b-quarks were matched to their closest offline jet in ΔR within a cone of $\Delta R \leq 1.0$ from the b-quark. The distribution in ΔR of these b-jets from each offline τ lepton is shown in figure 4.5(a), where there is a significant reduction in the number of jets in the region $\Delta R < 0.1$.

In table 4.1 the relative efficiencies for each level of the trigger are summarised and divided into regions of $\Delta R = 0.5$. There is a clear drop in efficiency from the average efficiency of $78 \pm 1\%$ to $21 \pm 5\%$ for the region $0.1 < \Delta R < 0.5$, and to $70 \pm 3\%$ for the region $0.5 < \Delta R < 1.0$. This is further illustrated in figure 4.5(b), labelled as the 'no parent' case, explained below.

To further purify the event selection to those shown in the topology in figure 4.3 require-

Trigger Level	Efficiency [%]			
	$0.1 \leq \Delta R < 0.5$	$0.5 \leq \Delta R < 1.0$	$1.0 \leq \Delta R < 1.5$	
L1	91 ± 13	93 ± 4	94 ± 3	
L2	72 ± 12	88 ± 4	88 ± 3	
EF	32 ± 8	85 ± 4	95 ± 3	
Combined	21 ± 5	70 ± 3	80 ± 2	
Trigger Level	Efficiency [%]			
	$1.5 \leq \Delta R < 2.0$	$2.0 \leq \Delta R < 2.5$	$2.5 \leq \Delta R < 3.0$	All regions
L1	95 ± 3	95 ± 3	94 ± 4	94 ± 1
L2	89 ± 3	89 ± 3	90 ± 4	89 ± 1
EF	95 ± 3	94 ± 3	94 ± 4	93 ± 1
Combined	80 ± 3	79 ± 3	79 ± 3	78 ± 1

Table 4.1: Relative efficiencies of the Tau Trigger for τ leptons in proximity to b-jets (with $\Delta R < 0.1$ veto).

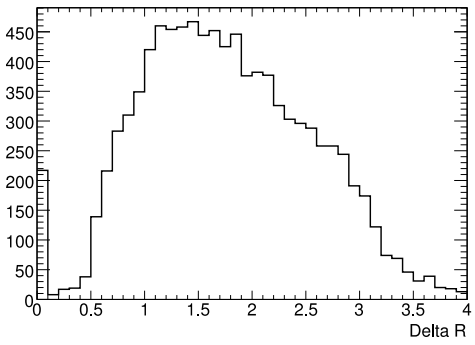

(a) ΔR between selected truth τ and closest b-jet

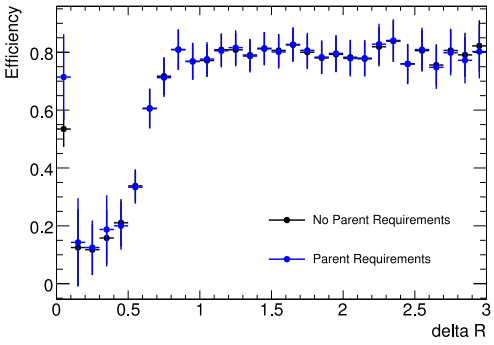

(b) Relative efficiency vs ΔR between truth τ and closest b-jet

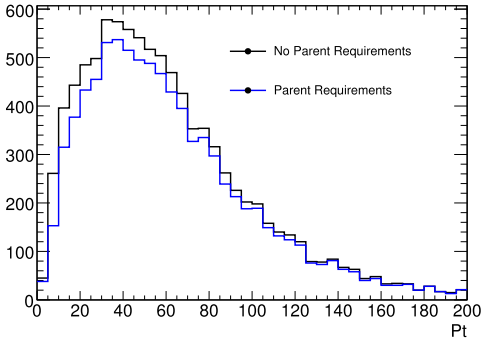

(c) p_T of closest jet with and without parent requirements

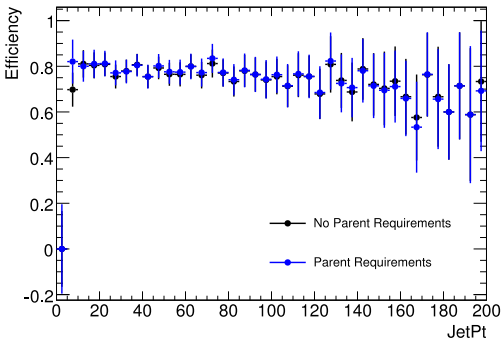

(d) Relative efficiency vs closest b-jet p_T

Figure 4.5: Relative efficiency of Tau Trigger with a b-jet in proximity.

ments were placed on the parenthood of the τ lepton. The τ lepton was required to be the daughter of a W boson, and the b quark, to be the daughter of a top quark. This helps select jets

with higher p_T which are more likely to affect the triggering, figure 4.5(c) shows a comparison between the scenarios with and without parent requirements; it depicts the normalised p_T distributions of the closest jet to each offline τ lepton. It shows a slight reduction in the number of lower-p_T jets with the addition of these parent requirements. In figure 4.5(d) the dependence of the Tau Trigger efficiency on the p_T of the closest jet is shown to be negligible. Since no benefit was seen and this further reduced statistics, these requirements were not employed.

4.5.3 All Parton Matching

To raise statistics without generating more events and to generalise the study it was extended to include jet matching to all partons instead of just the b-jets. This increased the number of offline τ candidates with jets close to them from 9602 out of 17373 offline τ candidates in the events to 16596; the percentage of τ leptons affected therefore rose from 55 to 96% as seen in table 4.2.

The parton matching was done in the same way as for b-jets, within a cone of $\Delta R = 1.0$ around the truth quark (u, d, c, s or b) the closest offline jet was chosen and labelled as a "parton-jet". The efficiency of the Tau Trigger was again measured for events which contained one of the parton-jets and a τ lepton and the efficiency was plotted as a function of ΔR between them. Figure 4.6 shows both the absolute efficiency and the relative efficiency for this scenario. The similar shapes in both plots, figure 4.6(a) and figure 4.6(b) show that this degradation in efficiency is a problem in both the trigger and the offline.

	B-Jet	Parton-Jet
Number of Events	185350	185350
Number of Good τ Leptons	17373	17373
Number of τ Candidates with Jets Close	9602	16596
Number of τ Candidates with No Close Jets	7771	777
Fraction of τ Candidates Affected [%]	55	96

Table 4.2: Statistics for b-jet study vs parton-jet study.

This degradation is shown in table 4.3, the values are averaged over a region of ΔR and are

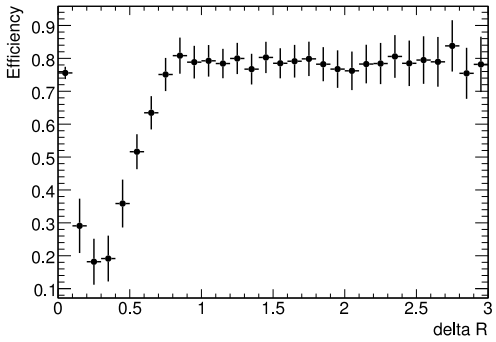

(a) Relative Efficiency vs ΔR between offline tau and closest parton-jet

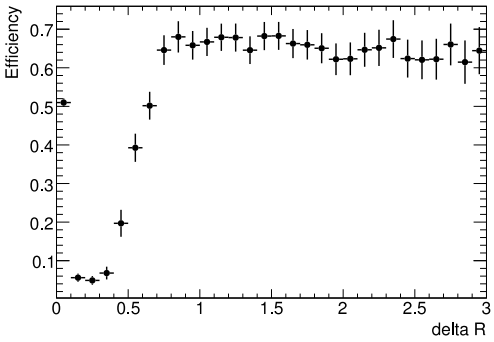

(b) Absolute Efficiency vs ΔR between good tau and closest parton-jet

Figure 4.6: Trigger Efficiencies for τ leptons with parton-jets in proximity.

effectively weighted by the statistics, which are lowest in the area most degraded in efficiency, $0.1 < \Delta R < 1.0$. In the corresponding plot for relative efficiencies in figure 4.6(a), the effect is clearer because the efficiency is averaged over smaller bins of $\Delta R = 0.1$. The efficiencies for each level calculated independently are included in table 4.3.

Trigger Level	Efficiency [%]			
	$0.1 \leq \Delta R < 0.5$	$0.5 \leq \Delta R < 1.0$	$1.0 \leq \Delta R < 1.5$	
L1	90 ± 8	94 ± 3	94 ± 2	
L2	74 ± 8	87 ± 3	88 ± 2	
EF	42 ± 6	88 ± 3	95 ± 3	
Combined	28 ± 4	72 ± 2	79 ± 2	
Trigger Level	Efficiency [%]			
	$1.5 \leq \Delta R < 2.0$	$2.0 \leq \Delta R < 2.5$	$2.5 \leq \Delta R < 3.0$	All regions
L1	95 ± 3	95 ± 3	95 ± 4	94 ± 1
L2	88 ± 2	88 ± 3	89 ± 4	88 ± 1
EF	94 ± 3	93 ± 3	93 ± 4	92 ± 1
Combined	78 ± 2	78 ± 3	78 ± 3	76 ± 1

Table 4.3: Relative efficiencies of the Tau Trigger for τ leptons in proximity to parton-jets (with $\Delta R < 0.1$ veto).

4.6 Variable Performance

Since the performance of the trigger has been shown to be reduced with additional activity in the event, it is important to probe the mechanisms of the trigger algorithm to look for any clear

causes. As τ leptons are primarily identified by being isolated and collimated, the most likely individual cuts causing the degradation are expected to be the isolation-based criteria because if a jet were to lie in the isolation region surrounding the τ candidate it should cause the τ lepton to fail the trigger. The baseline trigger tau16i was tested, the variables used in the trigger and their default values are listed in table 4.4.

Level 1 Quantities	
EMCore	$>$ 0 (off)
HadCore	$>$ 0 (off)
EMEnergy	$>$ 0 (off)
TauEnergy	$>$ 9 GeV
EMIsolation	$<$ 6 GeV
HadIsolation	$<$ 0 (off)
Level 2 Calorimetry Quantities	
StripWidth (single and multi-prong)	$<$ 1.0
EMRadius (single and multi-prong)	$<$ 0.01470
IsoFrac (single and multi-prong)	$<$ 1.0 (off)
Calibrated E_T	$>$ 0 (off)
Level 2 Tracking Quantities	
NTracks	1 - 7
Leading Track P_T	$>$ 0 (off)
Charge	$false$ (off)
SumPtRatio	$<$ 0.1
Event Filter Quantities	
NTracks	1 - 5
EMRadius (single and multi-prong)	$<$ 0.1 (0.12)
IsoFrac (single and multi-prong)	$<$ 1.0 (off)
Leading Track P_T (single and multi-prong)	$>$ 2.5 GeV
Calibrated E_T (single and multi-prong)	$>$ 16 GeV

Table 4.4: Tau16i standard trigger cut values.

As the degradation seems to occur when there is a jet close to the τ lepton it is logical that if the isolation requirements were relaxed in the Tau Trigger, the efficiency of these events should rise. Each variable was given a variety of values for the cut, each over the range of the variable distribution in the $t\bar{t}$ sample. The distribution of each variable for all selected truth τ leptons is shown in figure 4.7.

For each variable a new trigger menu was defined, each of the 10 triggers in the menu

mirrored the standard tau16i trigger with only one variable changed.

For each trigger the efficiency was calculated for each level independently and for the trigger combined over 6 regions of ΔR. The combined efficiency for each region of ΔR was plotted for each trigger cut value to see if there were a trigger cut value which would give a suitable trade-off between average efficiency and degradation in the lower regions of ΔR. Each variable was tested for all τ candidates and 1 and 3-prong τ candidates separately. Figure 4.8 shows the relative efficiency of the trigger for all τ candidates per variable. From these plots it is clear that none of the variables offered any cut values providing reduction in the difference between the efficiencies for the $\Delta R < 1.0$ and $\Delta R > 1.0$ regions without lowering the average efficiency too significantly; the outlook was the same in both the case of the 1 and 3-prong τ candidates.

The absolute efficiency measurements are shown in figure 4.9 for all τ candidates; these are important as they avoid any cuts already placed in the offline selection i.e. if cuts were placed in the offline selection it would not be possible to regain any additional candidates by loosening a cut. However the absolute efficiency distributions do not illustrate any potential for retuning the existing cuts in this manner.

4.7 Summary and Outlook

The performance of the Tau Trigger in conditions approximating pile-up was investigated. A Monte Carlo simulated sample of $t\bar{t}$ events was used which contained a τ lepton and a minimum of two jets expected to be in proximity to the τ lepton originating from the top quark decay. The performance was investigated by parametrising the measured trigger efficiency in terms of ΔR, a distance parameter between the τ candidate and its closest jet.

The efficiency was shown to be lower when a jet was present in the region $0.1 < \Delta R < 0.5$ around the τ candidate, the efficiency for all levels combined fell for this region to $28 \pm 4\%$ from the average, over all τ candidates with a jet within a radius of $\Delta R < 3.0$, of $76 \pm 1\%$.

To ascertain if any particular variable could be causing this degradation of performance, a

study of each variable related to isolation criteria was performed. Each variable was changed independently while the rest of the trigger remained unchanged. No values of any of the variables were observed which would reduce the difference in the performance between this region and the others, without causing a large reduction in the overall efficiency of the Tau Trigger. Therefore this study concludes that in order to improve performance under pile-up conditions new variables are necessary.

Since this study was performed as a preliminary study before the availability of simulated pile-up, a similar study of the degradation of performance of the Tau Trigger was later performed with simulated pile-up and reached the same conclusion that new variables were necessary to regain performance lost in pile-up conditions. Two new variables were introduced which were shown to be more stable with respect to pile-up and were able to improve performance [73].

The trigger for hadronically decaying τ leptons is not used throughout the remainder of this thesis. For the 2010 dataset it was possible to use single lepton triggers with a low enough p_T threshold. However a combined τ and lepton trigger will be required to analyse 2011 data due to the increase in instantaneous luminosity and therefore the rise of the p_T threshold of the triggers.

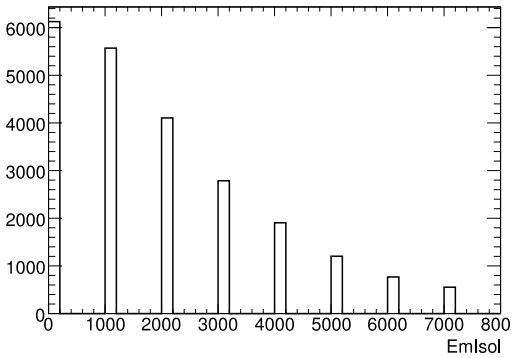

(a) L1EMIsolation distribution for all selected (good) truth τ candidates

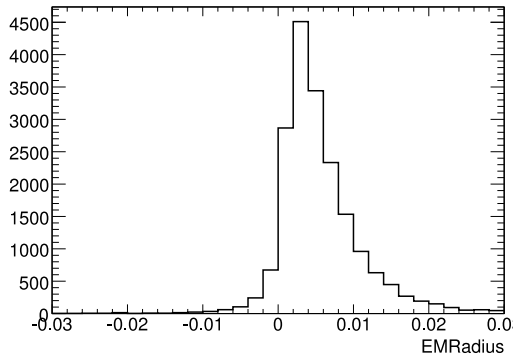

(b) L2EMRadius distribution for all selected (good) truth τ candidates

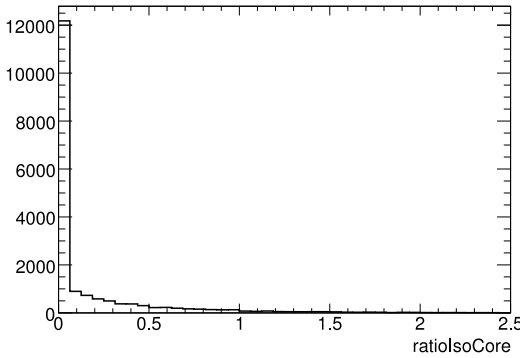

(c) L2RatioIsoCore distribution for all selected (good) truth τ candidates

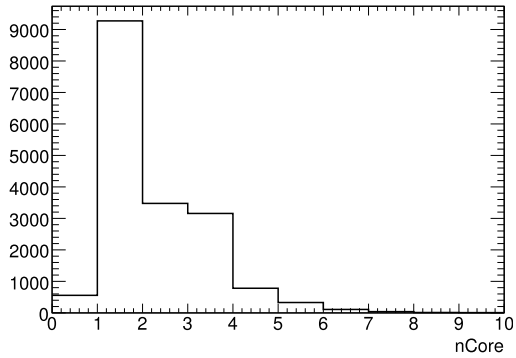

(d) L2NCore distribution for all selected (good) truth τ candidates

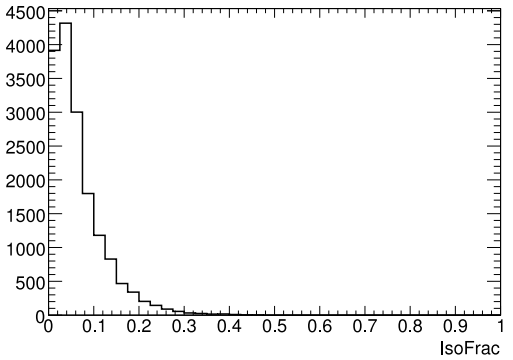

(e) L2IsoFrac distribution for all selected (good) truth τ candidates

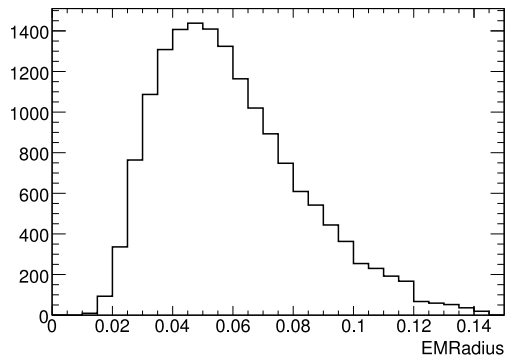

(f) EFEMRadius distribution for all selected (good) truth τ candidates

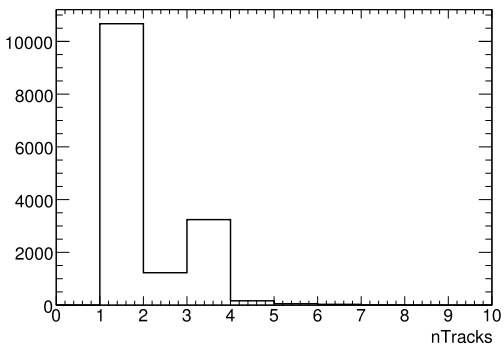

(g) EFNTracks distribution for all selected (good) truth τ candidates

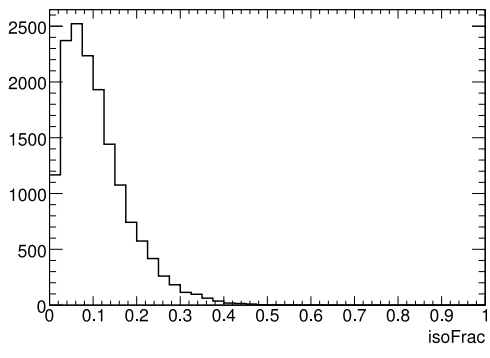

(h) EFIsoFrac distribution for all selected (good) truth τ candidates

Figure 4.7: Isolation-based trigger variable distributions for all selected truth τ candidates.

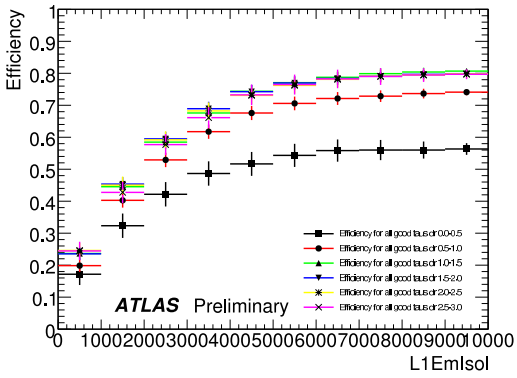

(a) Efficiency of the Tau Trigger vs L1EMIsolation

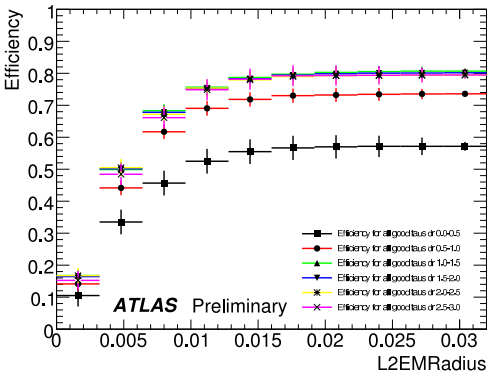

(b) Efficiency of the Tau Trigger vs L2EMRadius

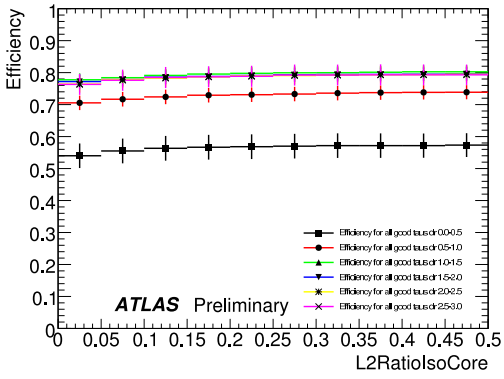

(c) Efficiency of the Tau Trigger vs L2RatioIsoCore

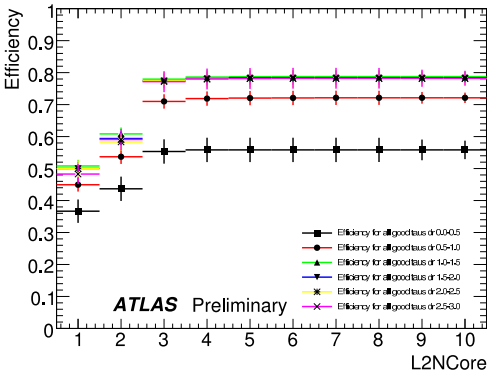

(d) Efficiency of the Tau Trigger vs L2NCore

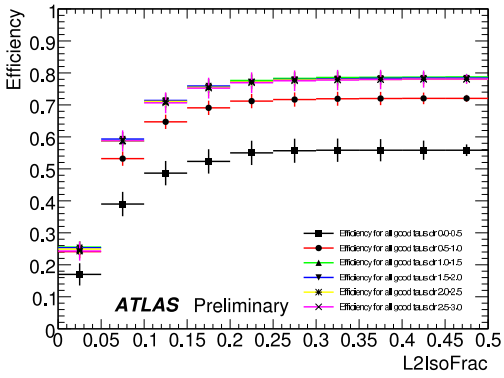

(e) Efficiency of the Tau Trigger vs L2IsoFrac

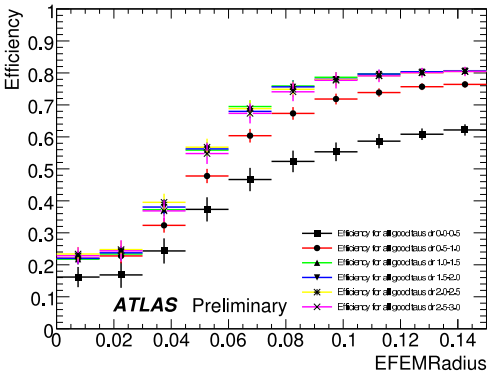

(f) Efficiency of the Tau Trigger vs EFEMRadius

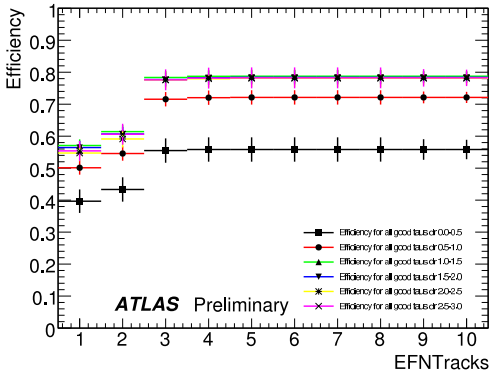

(g) Efficiency of the Tau Trigger vs EFNTracks

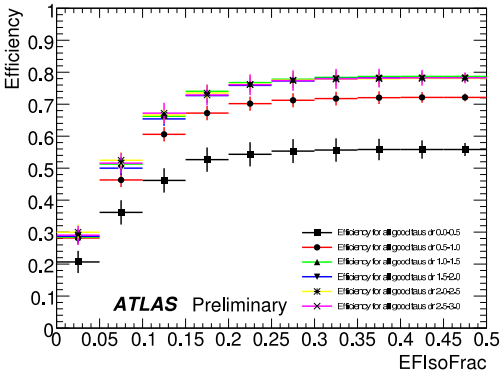

(h) Efficiency of the Tau Trigger vs EFIsoFrac

Figure 4.8: Relative trigger efficiencies vs isolation-based trigger variables for all τ candidates with $\Delta R < 0.1$ veto.

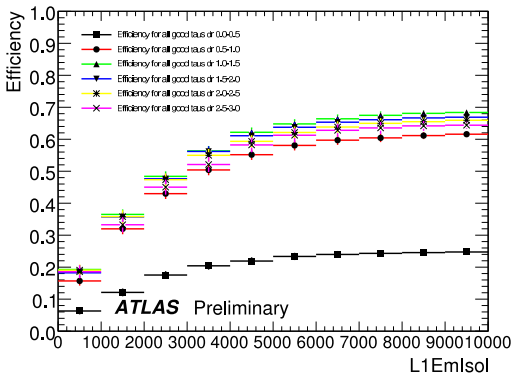

(a) Efficiency of the Tau Trigger vs L1EMIsolation

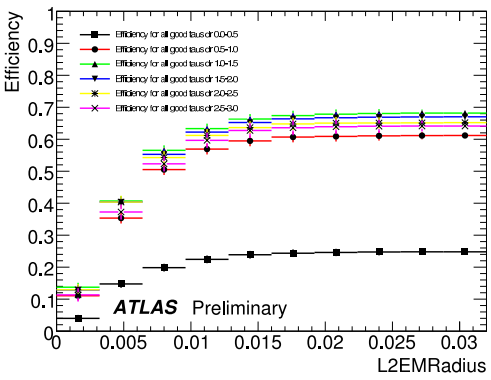

(b) Efficiency of the Tau Trigger vs L2EMRadius

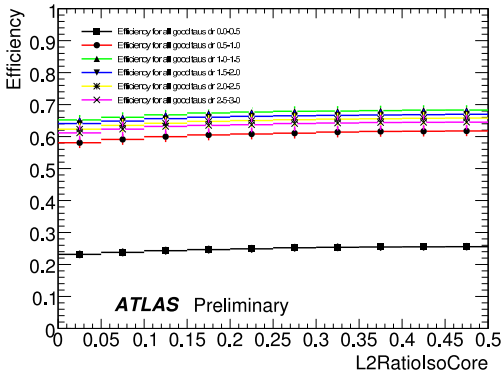

(c) Efficiency of the Tau Trigger vs L2RatioIsoCore

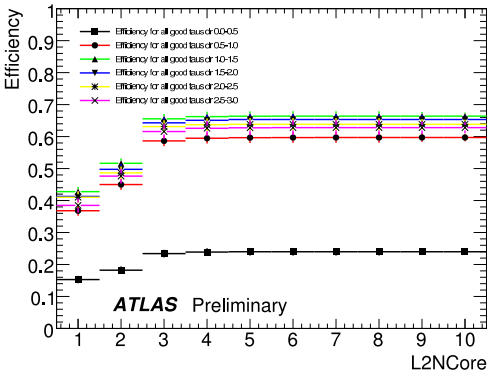

(d) Efficiency of the Tau Trigger vs L2NCore

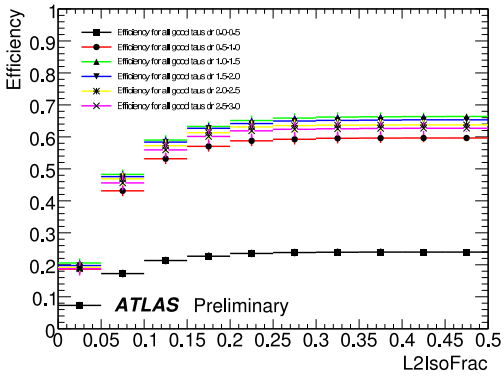

(e) Efficiency of the Tau Trigger vs L2IsoFrac

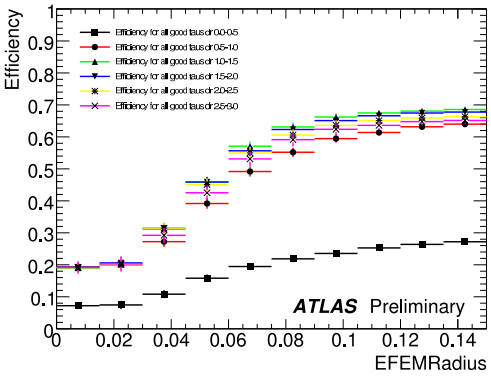

(f) Efficiency of the Tau Trigger vs EFEMRadius

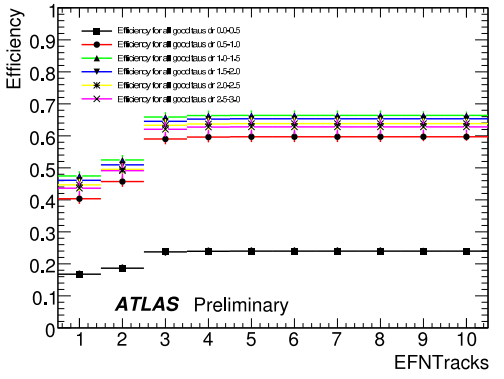

(g) Efficiency of the Tau Trigger vs EFNTracks

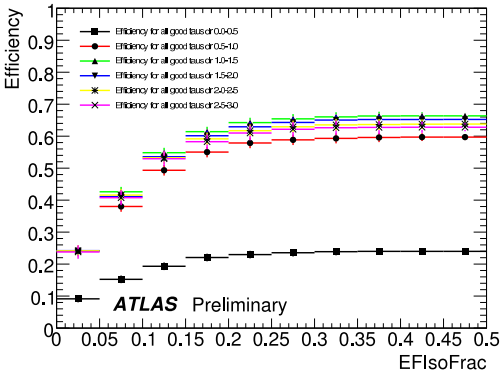

(h) Efficiency of the Tau Trigger vs EFIsoFrac

Figure 4.9: Absolute trigger efficiencies vs isolation-based trigger variables for all τ candidates with $\Delta R < 0.1$ veto.

Chapter 5

$Z \to \tau_\ell \tau_h$ Cross-section Measurement: Event Selection and Background Estimation

5.1 The $Z \to \tau_\ell \tau_h$ Process

The $Z \to \tau\tau$ process is a good source of τ leptons decaying hadronically. Identifying these is useful for many τ lepton physics performance studies which will improve the τ lepton triggering, reconstruction and identification. The τ lepton is often an key element in new physics searches, both in signal and background processes, and the understanding obtained by measuring the cross-section is very useful.

The measurement documented here is performed in two channels, the first is $Z \to \tau_e \tau_h$ and the second is $Z \to \tau_\mu \tau_h$. The cross-section is also measured in the two fully leptonically decaying modes, $Z \to \tau_e \tau_e$ and $Z \to \tau_\mu \tau_\mu$ and the four channels were combined and the results publically released [74]. The first iteration of this analysis was released as an observation using $\sim$8.5pb^{-1} [75] and was shown at the XLVI Rencontres de Moriond Electroweak session by the author of this thesis. The combined cross-section measurement has been published as a paper and shown at a variety of conferences.

The experimental signature for a hadronically decaying τ lepton (τ_h) is one or three charged tracks collimated in a narrow, isolated cone of energy deposits in the electromagnetic and hadronic calorimeters. The backgrounds to this topology consist of a lepton, which could be a real lepton from heavy flavour decays, or a fake lepton, in addition to a fake τ candidate from a quark or gluon initiated jet.

One of the main backgrounds to this process is the multijet background (often known as

QCD) due to its large cross-section, selecting isolated leptons is important to control this background; the isolation criteria are introduced in section 5.4.4. Another important background process is W + jets, which has a cross-section ten times higher than the signal. To help reject this background the angular correlations between the missing transverse energy (E_T^{miss}) and the visible decay products can be exploited, as well as the transverse mass quantity; both are discussed further in section 5.5.2. The background from $\gamma^*/Z \to ee, \mu\mu$ processes also needs to be identified and removed where possible, this is done using a di-lepton veto, described in section 5.5.1.

5.2 ATLAS Data in 2010

5.2.1 Data Quality

The data used for this analysis was proton-proton collision data at a centre-of-mass energy of 7 TeV collected by the ATLAS detector between July and October 2010. Data were selected using a number of quality requirements. The LHC had to be operating with stable beam conditions and collisions taking place and requirements were imposed on the conditions of the subdetectors. The selection was performed using a system called Good Runs Lists (GRL), based on requiring certain detector flags [76]. Both the solenoid and toroid magnets had to be operational and all L1 and Event Filter triggers had to be running. Additionally, criteria to ensure the quality of data for each reconstructed object were included for electrons, muons, τ leptons, jets and E_T^{miss}.

The luminosity was calculated using an ATLAS tool [77]. The calculation was based on the specific GRL and triggers used in this analysis. The result was scaled to the most-up-to-date luminosity measurement made by ATLAS, detailed in [78]. This resulted in 35.74 pb^{-1} for the electron channel and 35.51 pb^{-1} for the muon channel.

5.2.2 Monte Carlo Simulation

The Monte Carlo used for this analysis was generated taking advantage of knowledge gained from measurements made in early running in 2010, including material distribution, underlying event tuning, pile-up conditions and alignment [79]. Once the Monte Carlo had been generated, the full ATLAS simulation [80] was run and pile-up was modelled by overlaying minimum bias events onto the generated event. The following generators were used to produce the Monte Carlo samples: all W and $\gamma^{\star}/Z$ background samples as well as the Z signal samples were generated using PYTHIA [81], the $t\bar{t}$ samples with MC@NLO [82] and the di-boson samples with HERWIG [83]. The multijet (QCD) samples were produced with PYTHIA and filtered to contain at least one lepton with $p_T > 8$ GeV and $|\eta| < 3$. All τ decays were modelled using the TAUOLA interface [84] and all generators were interfaced with the PHOTOS package [85] to model final state QED radiation.

The cross-sections for the W, Z and $\gamma^{\star}/Z$ samples were calculated at NNLO and taken from [86], except for the low-mass $\gamma^{\star}/Z$ cross-sections which were taken from [87, 88]. The rest of the cross-sections were calculated at LO by the generators. All of the cross-sections used in this analysis, for each simulated sample, are summarised in table 5.1, along with the number of generated events.

5.2.3 Pile-up Simulation

There are two sources of pile-up in the data, the first, "in-time pile-up", arises from multiple interactions in the same bunch crossing. The second, "out-of-time pile-up", is additional activity from previous bunch crossings. Both give rise to additional reconstructed vertices in a given event. This is simulated by overlaying minimum bias events over the hard interaction in a particular bunch-train timing structure: individual bunches are separated by 150 ns and are in trains eight bunches long; the second train follows 225 ns later and a third after a longer

[1] These JXe and $JXmu$ samples are QCD di-jet production and the numbers refer to ranges of p_T of the hard scatter, $0 =$ 8-17 GeV, $1 =$ 17-35 GeV, $2 =$ 35-70 GeV and $3 =$ 70-140 GeV.

Dataset	Events	Cross-section [nb]
$Z \to ee$ ($m_{\ell\ell} > 60$ GeV)	5 M	990
$Z \to \mu\mu$ ($m_{\ell\ell} > 60$ GeV)	5 M	990
$Z \to \tau\tau$ ($m_{\ell\ell} > 60$ GeV)	2 M	990
$W \to e\nu$	7 M	1046
$W \to \mu\nu$	7 M	1046
$W \to \tau\nu$	2 M	1046
$t\bar{t}$	1 M	91.50
$J1e$[1](electron filter $p_T > 8$ GeV, $\|\eta\| < 3$)	998 k	8.81×10^5
$J2e$ (electron filter $p_T > 8$ GeV, $\|\eta\| < 3$)	497 k	2.54×10^5
$J3e$ (electron filter $p_T > 8$ GeV, $\|\eta\| < 3$)	499 k	3.72×10^4
$J0mu$ (muon filter $p_T > 8$ GeV, $\|\eta\| < 3$)	967 k	8.48×10^5
$J1mu$ (muon filter $p_T > 8$ GeV, $\|\eta\| < 3$)	997 k	8.14×10^5
$J2mu$ (muon filter $p_T > 8$ GeV, $\|\eta\| < 3$)	495 k	2.21×10^5
$J3mu$ (muon filter $p_T > 8$ GeV, $\|\eta\| < 3$)	499 k	2.85×10^4
$\gamma^*/Z \to \tau\tau$ (10 GeV $< m_{\ell\ell} <$ 60 GeV)	190 k	396.7
$\gamma^*/Z \to ee$ (15 GeV $< m_{\ell\ell} <$ 60 GeV)	996 k	146.2
$\gamma^*/Z \to \mu\mu$ (15 GeV $< m_{\ell\ell} <$ 60 GeV)	999 k	146.2
WW	250 k	11
ZZ	250 k	1.0
WZ	250 k	3.4

Table 5.1: Monte Carlo samples used for this analysis. All samples were generated with PYTHIA, except for $t\bar{t}$ which was generated with MC@NLO and the di-boson samples generated with HERWIG. All samples are with bunch-train pile-up setup.

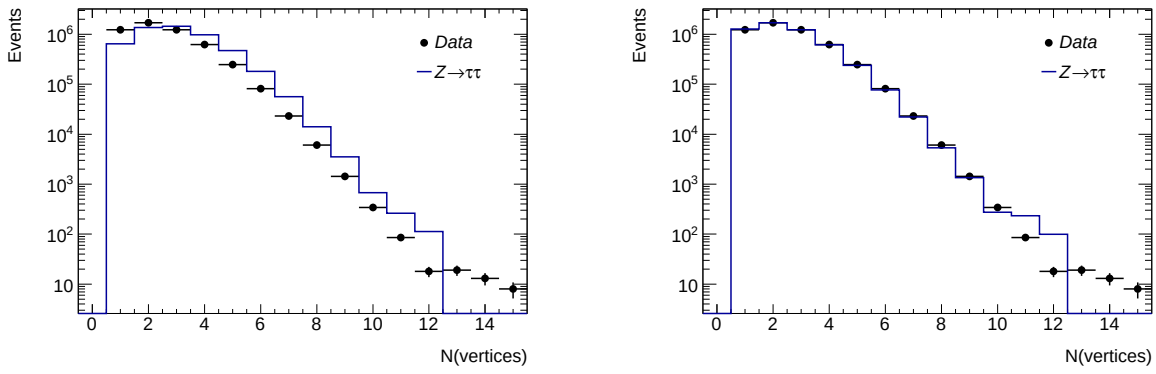

(a) (b)

Figure 5.1: Comparison of vertex distributions between data and signal Monte Carlo before (left) and after (right) vertex re-weighting.

pause. The simulation is generated with a Poisson distribution with an expectation value of 2.2 additional minimum bias interactions per event to simulate the data conditions. This gives rise to a difference in the distribution of the number of vertices between data and simulation, therefore

this distribution is reweighted in the simulation to match the data. The initial difference can be seen in figure 5.1(a) and the result of the re-weighting procedure is shown in figure 5.1(b). The weights were calculated separately for the electron and muon channels and then averaged; they are documented in table 5.2.

N_{vertex}	Event Weight
1	1.970(8)
2	1.242(4)
3	0.853(3)
4	0.633(2)
5	0.509(3)
6	0.427(4)
7	0.392(6)
8	0.38(1)
9	0.39(2)
10	0.41(5)
>=11	0.89(14)

Table 5.2: Number of reconstructed vertices and corresponding pile-up weights, the statistical uncertainty of the last digit is given in parentheses.

5.3 Event Preselection

5.3.1 Vertex Requirement

Collision candidate events were selected by requiring at least one primary reconstructed vertex with at least 3 reconstructed tracks.

5.3.2 Jet Cleaning

Occasionally there are localised deposits of energy in the calorimeters which do not originate from the proton-proton collision, these lead to mis-measurements of E_T^{miss} by causing high energy tails [89], or by being used as inputs for reconstructed jet and τ candidates. One cause of these deposits is high energy cosmic muons producing bremsstrahlung radiation as they traverse the calorimeters. By studying ATLAS data in 2010 with jet triggers, a series of recommenda-

tions for removing these events was formulated [90, 91]. These recommendations cut on the following properties of jets reconstructed with the Anti-k_t algorithm [65, 66] (using a cone of $\Delta R = 0.4$).

i) the fraction of the jet energy deposited in the Hadronic End Cap (HEC) calorimeter must be greater than the fractional contribution of the HEC calorimeter contribution to the jet energy from cells with normal signal shape

ii) if more than 50% of the jet energy is deposited in the HEC calorimeter, less than 50% of the HEC calorimeter contribution to the jet energy must come from cells with abnormal signal shape

iii) the jet must not have negative energy with a magnitude greater than 60 GeV

iv) if the jet is central in the detector ($|\eta| < 2.8$) and more than 90% of the jet energy is deposited in the electromagnetic (EM) calorimeter, less than 80% of the total jet energy must come from cells with an abnormal signal shape

v) the jet must primarily contain cells with energy deposited less than 10 ns before or after the nominal proton-proton collision time

vi) if the sum of the transverse momentum of the tracks associated to a central jet ($|\eta| < 2$) is less than 10% of the total jet energy , at least 5% of the jet energy must be deposited in the EM calorimeter

vii) if a jet is not central ($|\eta| \geq 2.0$), at least 5% of the jet energy must be deposited in the EM calorimeter

iix) if the jet is central ($|\eta| < 2.0$), the maximum fraction of the total energy in a single calorimeter layer must not exceed 99%

If all jets in a given data event with $p_T > 10$ GeV passed these requirements and did not overlap with an electron or muon, the event was kept.

5.3.3 Trigger Requirement

Events were triggered using unprescaled single lepton triggers. For the electron channel the trigger had a threshold of 15 GeV, for the muon channel the trigger for the earlier data had a threshold of 10 GeV, and for the later of 13 GeV.

The trigger efficiencies were measured from different data samples using a tag and probe analysis. For the muon channel this was performed on a sample of Z bosons decaying to two muons [64] and for the electron channel from a sample of W bosons decaying to an electron and a neutrino. These efficiencies can be seen in table 5.3 and table 5.4 respectively. The ratio of these efficiencies measured in data and simulation constitute the correction factors applied to the simulation to make them agree with data.

Trigger	Efficiency [%]
`EF_mu10_MG`	82.9±0.9(stat.)±0.3(syst.)
`EF_mu13_MG`	84.5±0.4(stat.)±0.1(syst.)
`EF_mu13_MG_tight`	83.1±0.4(stat.)±0.2(syst.)

Table 5.3: Muon trigger efficiency measured with respect to offline selected muons with $p_T >$ 15 GeV in data. Details can be found in [64].

Trigger	`EF_e15_medium` [%]
16 - 18 GeV	95.8±2.2(stat.)±0.6(syst.)
18 - 20 GeV	96.5±2.1(stat.)±0.4(syst.)
$>$ 20 GeV	99.05±0.22(stat.)±0.08(syst.)

Table 5.4: Electron trigger efficiency measured with respect to offline selected electrons in three p_T bins in data.

5.4 Object Selection

The $Z \to \tau_\ell \tau_h$ signature event contains an electron or a muon, a hadronically decaying τ lepton and neutrinos. Leptons were required to pass preselection criteria, these preselected leptons were then used to perform overlap removal, see section 5.4.1. If two or more of these preselected leptons were present, the event was vetoed, see section 5.5.1. After this, the leptons underwent

a tighter selection and the τ candidates were required to pass "tight" selection criteria, see section 5.4.5. The E_T^{miss} was reconstructed, but no direct requirement was made on it.

5.4.1 Preselection

Electrons The electron was required to have been reconstructed by the default cluster-based algorithm with a matched track, as described in section 3.3.2.1. The electron identification algorithm is designed to separate true electrons from jets faking electrons. It uses variables based on cluster shapes and tracking information. The electron identification has three levels of signal efficiency and purity, "loose", "medium" and "tight" [60]. Preselected electrons were required to have $p_T > 15$ GeV, be within $|\eta| < 2.47$, excluding the transition region between the barrel and end-cap calorimeters ($1.37 < |\eta| < 1.52$) and pass "medium" electron identification criteria. To avoid using any electron built from a cluster suffering from detector problems, information was used from the Object Quality maps (OQmaps) [86]. A summary of the preselection can be seen in table 5.5.

Muons Preselected muons were required to have $p_T > 15$ GeV, and $|\eta| < 2.4$ corresponding to the trigger acceptance region. The muons were reconstructed as a track from the inner detector combined with one from the muon spectrometer. The preselected muons were also required to have a longitudinal distance from the primary vertex, z_0, of less than 10 mm. A summary of the preselection can be seen in table 5.6.

τ Leptons Preselected τ candidates were required to have $p_T > 20$ GeV and be within $|\eta| < 2.47$, but not in the crack region ($1.37 < |\eta| < 1.52$). Further information about the τ reconstruction and identification algorithms can be found in section 5.4.5.

Overlap Removal Electrons, muons and τ candidates can often be reconstructed from the same tracks or energy clusters, therefore it was important to perform overlap removal. Muons are reconstructed with the highest purity, followed by electrons and finally τ leptons. If any

Electron Preselection used for Overlap Removal and Di-lepton Veto
$p_T > 15$ GeV
$\|\eta\| < 2.47$, but excluding $1.37 < \|\eta\| < 1.52$
Not in bad OQmaps region, use map of run 167521
"MediumWithTrackMatch" electron
Electron Selection
$p_T > 16$ GeV
"TightWithTrackMatch" electron

Table 5.5: Preselection and selection cuts of electrons.

preselected τ candidate overlapped with a preselected electron or muon within $\Delta R < 0.4$ it was removed. If a preselected electron overlapped with a preselected muon within $\Delta R < 0.2$ it was removed. If any preselected electron or muon overlapped with a higher-p_T object of the same type within $\Delta R < 0.2$ it was also removed. After all cuts the overlap removal was shown to reduce signal efficiency by only 0.1%.

5.4.2 Electron Selection

In order to avoid the poorly modelled region of phase space in the simulation where the p_T of the electron is close to the trigger threshold, the selected electrons were required to have $p_T > 16$ GeV. The selected electrons were also required to pass the "tight" level of identification. The full preselection and selection requirements are listed in table 5.5.

5.4.3 Muon Selection

Selected muons were required to have good quality inner detector tracks, this meant at least 1 hit in the b-layer, and that the sum of hits and dead sensors in the pixel detector must be greater than 1. They were also required to have a minimum of 5 hits and dead sensors in the SCT detector and less 2 holes in the pixel and SCT detector. Finally an additional cut was applied to the fraction of TRT outlier hits (see section 3.3.1.2) to total TRT hits. The full preselection and selection requirements are listed in table 5.6.

Muon Preselection used for Overlap Removal and Di-lepton Veto
$p_T > 15$ GeV
$\|\eta\| < 2.4$
"isCombinedMuon"
$\|z_0\| < 10$ mm
Muon selection
$p_T > 15$ GeV
no BlayerHit expected or nBLayerHits > 0
nPixHits + nDeadPixelSensors > 1
nSCTHits + nDeadSCTSensors > 5
nPixHoles + nSCTHoles < 2
$\|\eta\| < 1.9$: nTRT Outliers / (nTRT Hits + nTRT Outliers) < 0.9
& nTRT Hits + nTRT Outliers > 5
$\|\eta\| >= 1.9$: (nTRT Hits + nTRT Outliers > 5
& nTRT Outliers / (nTRT Hits + nTRT Outliers) < 0.9)
or nTRT Hits + nTRT Outliers < 6

Table 5.6: Preselection and selection cuts of muons.

5.4.4 Lepton Isolation

The leptons from Z$\rightarrow \tau\tau$ events are typically isolated, unlike those from multijet events, which can be jets falsely identified as leptons or muons produced inside jets. Therefore requiring that the leptons in the event passed strict isolation criteria gave powerful rejection against the multijet background.

Two isolation variables were defined: the first (equation 5.1) is the sum of the transverse momenta of tracks in a cone of $\Delta R = 0.3$ or 0.4 around the lepton, divided by the transverse momentum of the lepton. The second (equation 5.2) is the sum of the transverse energy of neutral and charged particles in the calorimeter in a cone of $\Delta R = 0.3$ or 0.4 around the lepton, divided by the transverse momentum of the lepton.

$$p_T\text{Cone}/p_T = \frac{\sum\limits_{\Delta R} p_{T_{tracks}}}{p_{T_{lepton}}} \tag{5.1}$$

$$E_T\text{Cone}/p_T = \frac{\sum\limits_{\Delta R} E_{T_{cal}}}{p_{T_{lepton}}} \tag{5.2}$$

For both variables, the contribution to either the sum of the transverse momenta or energies

in the isolation cone from the lepton itself was subtracted in an inner cone of $\Delta R = 0.05$.

The p_TCone40$/p_T$ and E_TCone40$/p_T$ variables for muons are illustrated in figure 5.2(a) and figure 5.2(c) and the p_TCone40$/p_T$ and E_TCone30$/p_T$ variables for electrons in figures 5.2(b) and 5.2(d). In figure 5.2 the simulation and data required an opposite sign τ candidate and lepton, and the multijet background was taken from a control sample in data in which the lepton and τ candidate were required to have same sign electric charge.

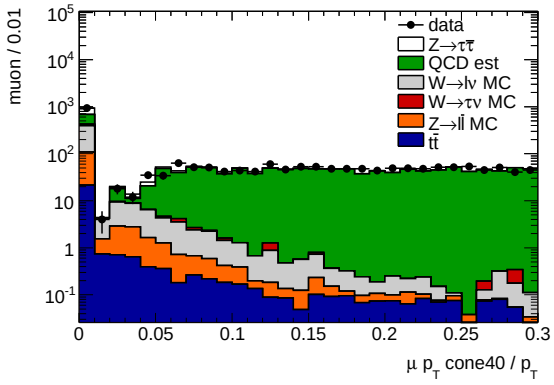

(a) Muon isolation p_TCone40/p_T.

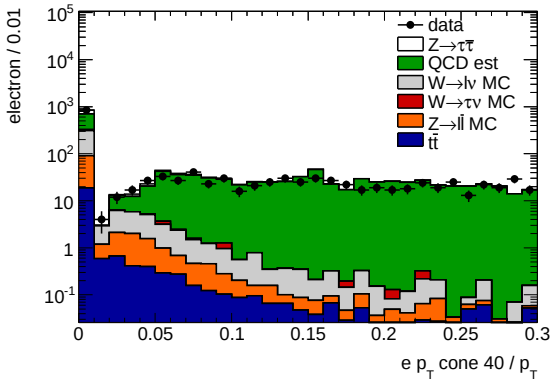

(b) Electron isolation p_TCone40/p_T.

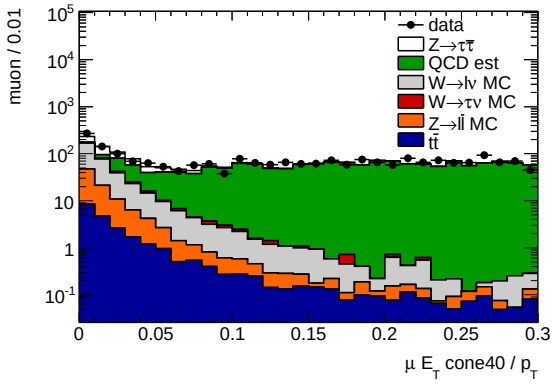

(c) Muon isolation E_TCone40/p_T.

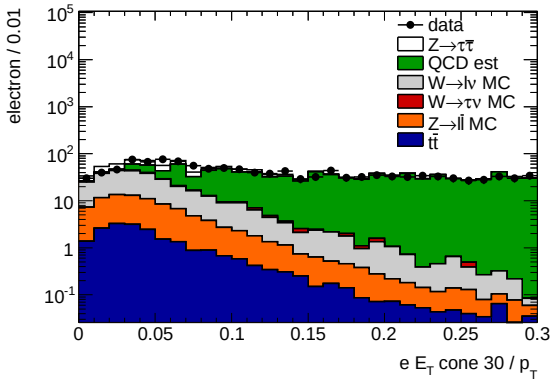

(d) Electron isolation E_TCone30/p_T.

Figure 5.2: Isolation variables for electroweak simulation, multijet events and data events after selecting one τ candidate and one lepton with opposite sign electric charges. The electroweak background was obtained from simulation, weighted by cross-section. The multijet background (QCD est.) was estimated by reversing the opposite sign requirement.

These different cone sizes were tested for performance in terms of signal efficiency and efficiency for multijet events, this can be seen in figure 5.3(a) and figure 5.3(b) for muons and electrons respectively. The signal was taken from simulation and the multijet events were taken from a control sample in data, defined by inverting the τ identification requirements and

requiring the selected lepton and τ candidates to have the same sign electric charge.

To reject the multijet events while keeping a large number of signal events, the following cuts were chosen:

- For electrons: $p_T\text{Cone40}/p_T < 0.06$ and $E_T\text{Cone30}/p_T < 0.1$
- For muons: $p_T\text{Cone40}/p_T < 0.06$ and $E_T\text{Cone40}/p_T < 0.06$

the two cuts together are known as "combined isolation". The corresponding cut efficiencies are given in table 5.7.

Isolation Variable	$Z \to \tau\tau$	Multijet
muon $p_T\text{Cone40}/p_T < 0.06$	0.926(2)	0.076(1)
muon $E_T\text{Cone40}/p_T < 0.06$	0.872(3)	0.0309(6)
muon "Combined Isolation"	0.841(3)	0.0143(4)
electron $p_T\text{Cone40}/p_T < 0.06$	0.941(3)	0.232(3)
electron $E_T\text{Cone30}/p_T < 0.1$	0.814(4)	0.082(2)
electron "Combined Isolation"	0.781(4)	0.046(1)

Table 5.7: Efficiency of isolation variables for electrons and muons in signal simulation and multijet background after object selection cuts. In parentheses is the statistical error of the last digit.

The efficiency of the isolation cuts was measured in data using a tag and probe method and correction factors were applied to the simulation to correct for the differences between simulation and data (further details in section 6.1.1.7).

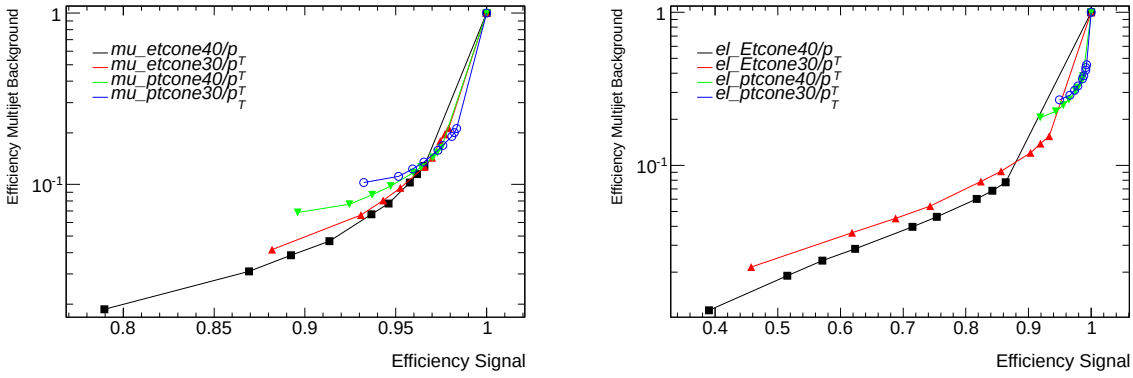

(a) Muon channel. (b) Electron channel.

Figure 5.3: Isolation efficiencies of signal simulation and multijet data events for different isolation variables.

5.4.5 Tau Selection

Hadronically decaying τ leptons are reconstructed by searching for calorimeter jets reconstructed using the Anti-k_{T} algorithm [65, 66] (with distance parameter $\Delta R = 0.4$) from topological clusters [59]. They were required to have $p_T > 10$ GeV and were calibrated by applying a correction to the reconstructed energy at the electromagnetic energy scale. A track was associated to the candidate if it had $p_T > 10$ GeV and passed selected quality criteria, detailed in [45]. Additional variables were calculated for each τ candidate from the calorimeter and tracking information, which were then used to identify good quality candidates.

The cut-based identification quality criteria defined in Winter 2011 [45] were used for this analysis. The cuts are detailed in section 3.3.4.2.

There are three levels of cuts, "loose", "medium" and "tight". Each level is defined based on a target efficiency for the signal, where the target efficiency for "loose" is 60%, for "medium" it is 45% and for "tight" it is 30%. This analysis required "medium" for one-prong candidates and "tight" for three-prong candidates. All τ candidates also had to pass a separate electron veto [58] (see section 3.3.4.3). The τ lepton selections are summarised in table 5.8.

τ Candidate Preselection
$p_T > 20$ GeV
$\lvert\eta\rvert < 2.47$, excluding $1.37 < \lvert\eta\rvert < 1.52$
τ Candidate Selection
Passes Electron Veto
1-prong "medium", 3-prong "tight" cuts τ-ID

Table 5.8: Summary of the τ candidate selection cuts.

5.4.6 Transverse Missing Energy

The transverse missing energy E_T^{miss} reconstruction used components from three algorithms, combined as in equation 5.3.

$$E_T^{\mathrm{miss}} = E_T^{\mathrm{miss}}(Calorimeter) + E_T^{\mathrm{miss}}(Muon) - E_T^{\mathrm{miss}}(Muon\,Track). \tag{5.3}$$

where $E_T^{\text{miss}}(Calorimeter)$ is a sum of all the energy deposited in calorimeter cells used in topological clusters [59] which are calibrated to either the electromagnetic or hadronic scale depending on the classification of the object. $E_T^{\text{miss}}(Muon)$ is the combined sum of p_T of all combined isolated muons, muons in gaps and non-isolated muon tracks in the muon spectrometer. If a muon was $\Delta R > 0.3$ from a jet, it was considered as isolated. $E_T^{\text{miss}}(Muon\ Track)$ is the sum of the energy deposited in the calorimeter cells by isolated muons.

5.4.7 Object Selection Summary

Table 5.9 summarises the cut flow so far, normalised to the integrated luminosity. It shows that the requirement of a selected τ lepton was the least efficient cut. Figure 5.4 shows the kinematic distributions of the selected objects.

	Electron channel (35.7pb^{-1})	Muon channel (35.5pb^{-1})
Selection	N_{events}	N_{events}
Preselected Lepton and Overlap Removal	2497(7)	2478(7)
Preselected τ Candidate and Overlap Removal	1179(5)	1133(5)
Selected Lepton	690(4)	1143(5)
Isolated Lepton	531(3)	941(5)
Selected τ Candidate	141(2)	258(2)

Table 5.9: Summary of object selection effect on signal Monte Carlo events for both channels. Numbers are normalised to the integrated luminosity used.

5.5 Event Selection

5.5.1 Di-lepton Veto

In order to eliminate $Z \to \ell\ell$ background events, events with more than one preselected lepton of any kind were vetoed. This was also effective at suppressing $Z \to \tau\tau \to \ell\ell + \nu\nu$ background events. Figure 5.5 shows the number of preselected leptons for each background sample. Rejecting leptons at the level of preselection instead of selection offered an additional rejection

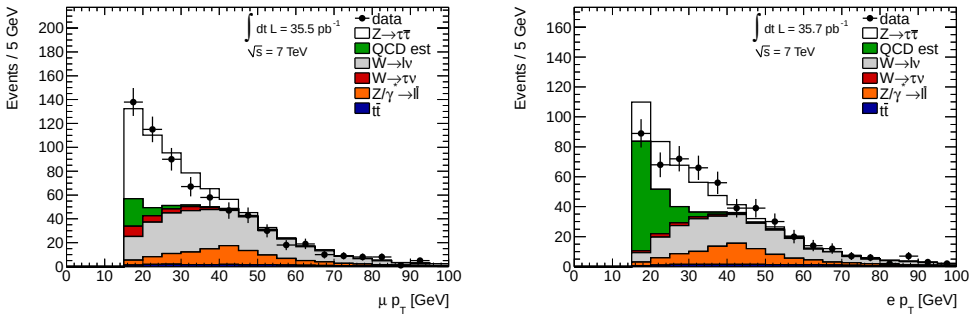

(a) Muon channel

(b) Electron channel

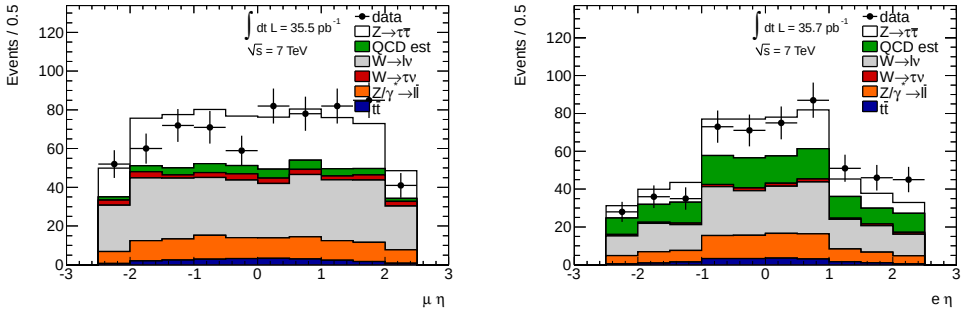

(c) Muon channel

(d) Electron channel

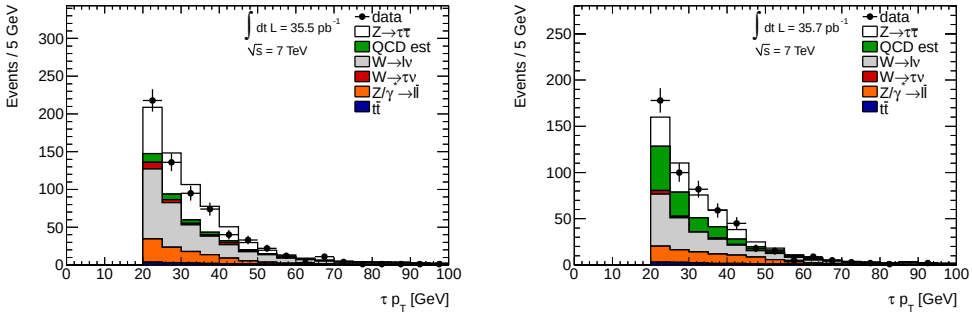

(e) Muon channel

(f) Electron channel

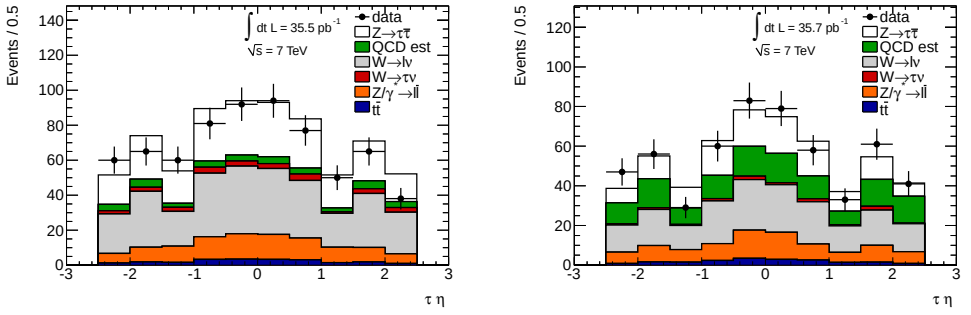

(g) Muon channel

(h) Electron channel

Figure 5.4: Kinematic distributions for reconstructed leptons and τ candidates following all object selections. A requirement of the charge of the τ candidate to be of opposite sign of that of the lepton was also applied. The predictions for individual processes were taken from Monte Carlo, except for the multijet background, which was taken from an orthogonal data sample obtained by inverting the opposite-sign requirement and rescaled using the multijet background estimation.

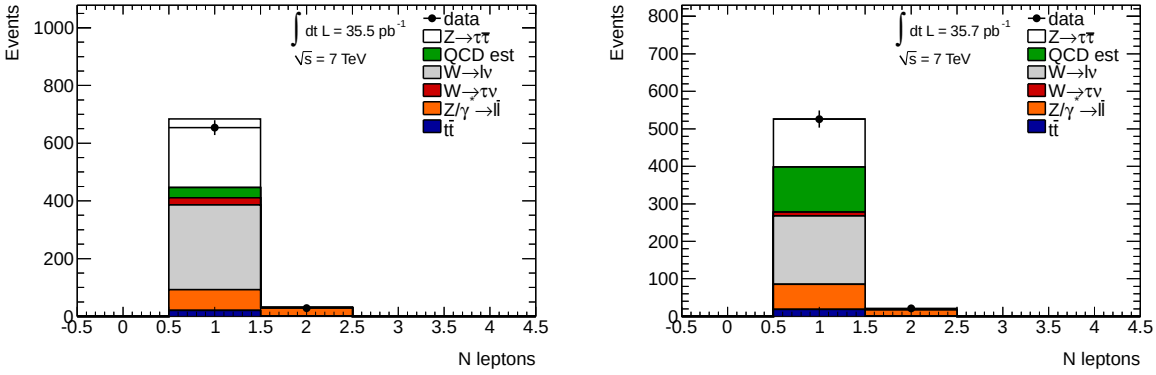

(a) Muon channel (b) Electron channel

Figure 5.5: Distributions of the number of preselected leptons prior to the di-lepton veto, following all object selections. A requirement on the charge of the τ candidate to be of opposite sign to that of the lepton has been applied, the multijet background contribution was estimated by inverting this cut in data; all other processes were estimated using Monte Carlo.

of 18% and 2% of $Z \to ee$ and $\mu\mu$ background events respectively, while only losing an extra 0.1% of $Z \to \tau\tau$ signal events.

5.5.2 W + jets Suppression Cuts

One of the most significant backgrounds to control was the W + jets background, consisting of both $W \to \ell\nu$ and $W \to \tau\nu \to \ell\nu\nu\nu$ decays. Taking advantage of the kinematics of the event topology it was possible to form two variables based on the direction of the missing transverse energy and the lepton, which effectively discriminated against this background. Due to the mass difference between the Z boson and the τ lepton, the decay products of the τ lepton are collimated in the direction of the τ lepton.

$$\sum \cos\Delta\phi = \cos\left(\phi(\ell) - \phi(E_T^{\text{miss}})\right) + \cos\left(\phi(\tau_{\text{h}}) - \phi(E_T^{\text{miss}})\right) \tag{5.4}$$

The first variable, the sum of the differences in ϕ between the lepton and E_T^{miss} and the τ lepton and the E_T^{miss}, $\sum \cos\Delta\phi$, is zero when the two τ leptons are back to back, as in the case of most $Z \to \tau\tau$ signal events. If the Z boson is boosted the E_T^{miss} vector lies in the azimuthal range spanned by the decay products, as illustrated in figure 5.6(a), and $\sum \cos\Delta\phi$ is positive. In the

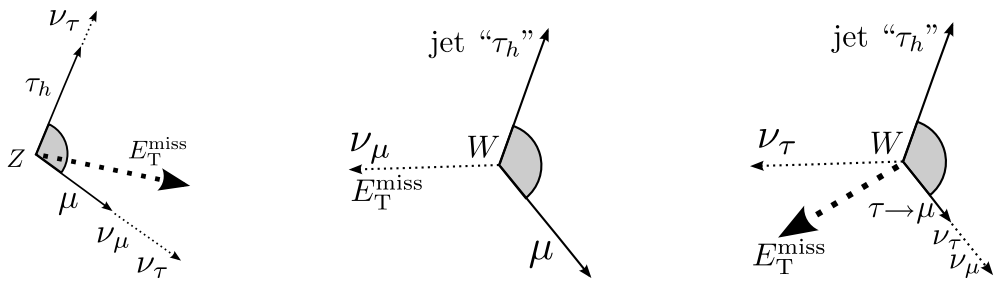

(a) $Z \to \tau\tau \to \mu\nu\nu\tau_{\mathrm{h}}\nu$ (b) $W \to \mu\nu$ (c) $W \to \tau\nu \to \mu\nu\nu\nu$

Figure 5.6: Drawings of representative transverse plane orientations of W and Z decay products and the E_T^{miss}. The shaded angles indicate the angle (less than π) between the lepton and the (fake) τ candidate. In (a), the Z is depicted to have non-zero p_T, which must be balanced on the left by some other activity omitted for clarity.

W + jets events the E_T^{miss} vector tends to lie outside of this angle, as shown in figures 5.6(b) and 5.6(c), therefore $\sum \cos\Delta\phi$ is predominantly negative. Requiring $\sum \cos\Delta\phi >$ -0.15 effectively discriminated against the W + jets events.

$$m_{\mathrm{T}}(\ell, E_T^{\mathrm{miss}}) = \sqrt{2\, p_{\mathrm{T}}(\ell) \cdot E_T^{\mathrm{miss}} \cdot (1 - \cos\Delta\phi(\ell, E_T^{\mathrm{miss}}))} \tag{5.5}$$

The second variable, $m_{\mathrm{T}}(\ell, E_T^{\mathrm{miss}})$, is small for signal events, whereas in the W + jets events it peaks around the W boson mass. Due to the effectiveness of the $\sum \cos\Delta\phi$ cut, a loose cut of $m_{\mathrm{T}} < 50$ GeV was used. The distributions of both of these variables are included for both channels in figure 5.7.

5.5.3 Final Event Selection

5.5.3.1 τ candidate cuts

To reject the multijet background, the τ candidate was required to have unit electric charge and exactly one or three tracks, which is strongly characteristic of hadronic decays of τ leptons.

In $Z \to \tau\tau$ events the lepton and the τ candidate will be of opposite charge, however in multijet events there is no bias towards opposite sign or same sign, therefore an opposite sign requirement gives good rejection.

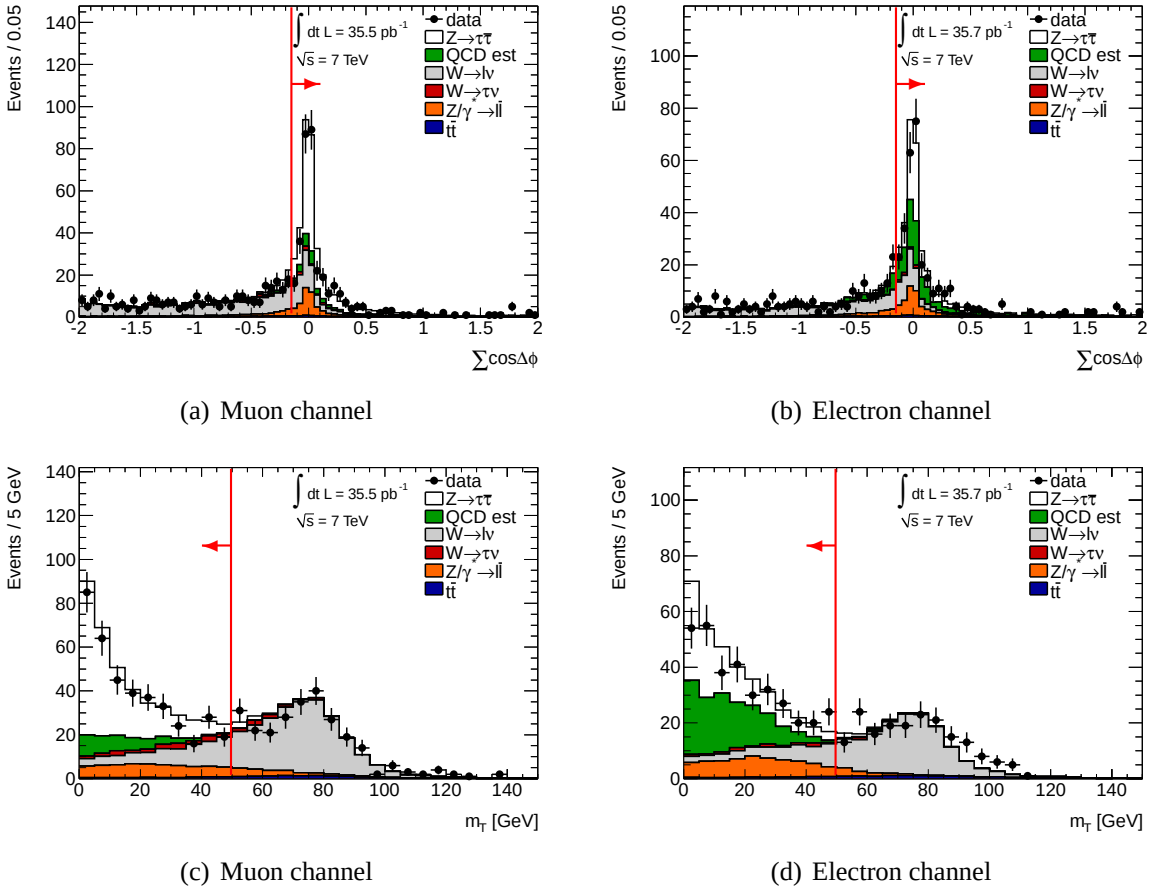

(a) Muon channel

(b) Electron channel

(c) Muon channel

(d) Electron channel

Figure 5.7: The distributions of $\sum \cos \Delta\phi$ are shown for the muon (a) and electron (b) channels. The distributions of transverse mass, m_{T}, of the combination of the lepton and the E_T^{miss} are shown for the muon (c) and electron (d) channels. All of these distributions are shown following the full object selections (Section 5.4) and di-lepton veto (Section 5.5.1). A requirement on the charge of the τ candidate to be of opposite sign to that of the lepton was also applied, the multijet background contribution was estimated by inverting this cut in data; all other processes were estimated using Monte Carlo.

5.5.3.2 Visible Mass

The visible mass is defined as the invariant mass of the τ candidate and the lepton and peaks around 55 GeV for $Z \rightarrow \tau\tau$ events as can been seen in the distributions of this variable for both channels in figure 5.8. Imposing a window cut on the visible mass of 35-75 GeV reduced contamination from $Z \rightarrow \ell\ell$ events which peak around 90 GeV. This peak can be clearly seen in the electron channel in figure 5.8(b).

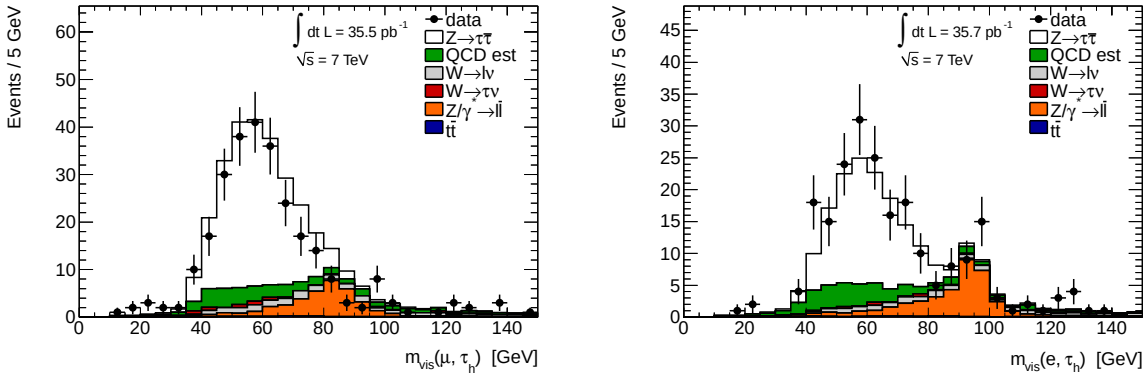

(a) Muon channel (b) Electron channel

Figure 5.8: The distributions of the visible mass of the combination of the chosen τ candidate and chosen lepton are shown for the muon (a) and electron (b) channels. These distributions are shown following the full object selections (Section 5.4) and event selections (Section 5.5), except for the visible mass window and clearly show the excess of signal over background.

5.5.3.3 Selection Summary

Table 5.10 presents a summary of all event selections. The numbers of events passing each cut in the muon and electron channels can be seen in tables 5.11 and 5.12 respectively.

The η and p_T distributions of the selected leptons and τ candidates for all events passing the event selection can be seen in figure 5.9. In figure 5.10 the distributions of the E_T^{miss}, $\Delta\Phi$ between the selected τ candidate and lepton, and the W suppression cuts are shown after all other cuts were applied. These give the reader a feel for the distributions and also show good agreement with the data. In figure 5.11 the distribution of the number of tracks associated to the selected τ candidate is shown in both channels and shows the characteristic shape expected of hadronically decaying τ leptons.

5.6 Background Estimation

To obtain estimates of the number of events from backgrounds after the final event selection, Monte Carlo was used for the $Z \to \ell\ell$, $t\bar{t}$ and di-boson backgrounds, normalised to integrated luminosity and cross-section. The $W \to \ell\nu$ and $W \to \tau\nu$ backgrounds were taken from simulation and normalised to agree with the data, using a scale factor discussed further in sec-

Event Preselection	
Primary Vertex	$N_{vtx} \geq 1$ with $N_{trk} \geq 3$
Jet Cleaning	Cleaning cuts "medium" with τ specific modifications
Trigger	`EF_e15_medium` (e channel) `EF_mu10_MG`,`EF_mu13_MG`,`EF_mu13_MGtight` (μ channel)
Preselection	
Electrons	$p_T > 15$ GeV $\|\eta\| < 2.47$, but excluding $1.37 < \|\eta\| < 1.52$ not in bad Object Quality map region, map of run 167521 "MediumWithTrackMatch" electron
Muons	$p_T > 15$ GeV $\|\eta\| < 2.4$ "isCombinedMuon" $\|z_0\| < 10$ mm
τ candidates	$p_T > 20$ GeV $\|\eta\| < 2.47$, but excluding $1.37 < \|\eta\| < 1.52$
Overlap Removal	Order of lowest priority: τ candidate, electron, muon
Object Selection	
Electrons	$p_T > 16$ GeV "TightWithTrackMatch" electron p_TCone40$/p_T < 0.06$; E_TCone30$/p_T < 0.1$
Muons	$p_T > 15$ GeV no BlayerHit expected or nBLayerHits > 0 nPixHits + nDeadPixelSensors > 1 nSCTHits + nDeadSCTSensors > 5 nPixHoles + nSCTHoles < 2 $\|\eta\| < 1.9$: nTRT Outliers / (nTRT Hits + nTRT Outliers) < 0.9 & nTRT Hits + nTRT Outliers > 5 $\|\eta\| >= 1.9$: (nTRT Hits + nTRT Outliers > 5 & nTRT Outliers / (nTRT Hits + nTRT Outliers) < 0.9) or nTRT Hits + nTRT Outliers < 6 p_TCone40$/p_T < 0.06$; E_TCone40$/p_T < 0.06$
τ candidates	Passes e Veto 1-prong "medium", 3-prong "tight" cuts τ-ID
Event Selection	
W + jets Suppression	$\sum \cos\Delta\phi >$ -0.15 $m_{\mathrm{T}} < 50$ GeV
Di-lepton Veto	Remove Event if N(preselected leptons)> 1
Visible Mass Cut	35 GeV $< m_{vis} <$ 75 GeV
τ Candidate Cuts	$N_{\mathrm{tracks}}(\tau_{\mathrm{h}}) = 1$ or 3 $\|\mathrm{charge}(\tau_{\mathrm{h}})\| = 1$
Opposite Sign Cut	$\mathrm{charge}(\tau_{\mathrm{h}}) \times \mathrm{charge}(\ell) < 0$

Table 5.10: Selection summary.

	Data	$\gamma^*/Z \to \tau\tau$	Multijets	$\gamma^*/Z \to \mu\mu$	$W \to \mu\nu$	$W \to \tau\nu$	$t\bar{t}$	Di-boson
Object Selection	1365	261(3)	163(9)	216(2)	649(6)	54(3)	38.9(5)	8.6(1)
Di-lepton Veto	1291	260(3)	162(8)	125(2)	648(6)	54(3)	34.3(5)	7.8(1)
W Suppression Cuts	462	231(3)	90(4)	58(1)	66(2)	18(2)	7.8(2)	1.34(5)
$m_{\mathrm{vis}} = 35$-75 GeV	327	205(2)	71(3)	23.1(9)	23(1)	10(1)	2.4(1)	0.49(3)
$N_{\mathrm{trk}}(\tau_{\mathrm{h}}) = 1$ or 3, $\lvert \mathrm{Q}(\tau_{\mathrm{h}}) \rvert = 1$	247	187(2)	42(3)	15.3(7)	12.1(8)	5(1)	1.4(1)	0.32(2)
Opposite Sign	213	186(2)	23(3)	11.1(5)	9.3(7)	3.6(8)	1.3(1)	0.28(2)

Table 5.11: Numbers of events passing the cumulative event selections for the muon channel. The statistical errors on the least significant digits are given in the parentheses. The predictions for individual processes were taken from Monte Carlo, except for multijets, which was estimated with the Non-Isolated method described in section 5.6.3.

	Data	$\gamma^*/Z \to \tau\tau$	Multijets	$\gamma^*/Z \to ee$	$W \to e\nu$	$W \to \tau\nu$	$t\bar{t}$	Di-boson
Object Selection	1203	141(2)	402(12)	164(1)	409(4)	24(2)	33.0(4)	6.4(1)
Di-lepton Veto	1144	140(2)	400(11)	116(1)	409(4)	24(2)	29.1(4)	5.9(1)
W Suppression Cuts	449	125(2)	159(6)	70(1)	43(1)	10(1)	6.7(2)	0.98(4)
$m_{\mathrm{vis}} = 35\text{-}75$ GeV	273	107(1)	95(4)	19.2(7)	12.8(7)	3.7(7)	1.7(1)	0.32(2)
$N_{\mathrm{trk}}(\tau_{\mathrm{h}}) = 1$ or 3, $\lvert \mathrm{Q}(\tau_{\mathrm{h}}) \rvert = 1$	180	98.5(1)	53(4)	11.0(5)	6.7(5)	1.8(5)	1.13(9)	0.21(2)
Opposite Sign	151	97(1)	25(3)	6.9(4)	4.8(4)	1.5(4)	1.02(8)	0.18(1)

Table 5.12: Numbers of events passing the cumulative event selections for the electron channel. The statistical errors on the least significant digits are given in the parentheses. The predictions for individual processes are taken from Monte Carlo, except for multijets, which was estimated with the Non-Isolated method described in section 5.6.3.

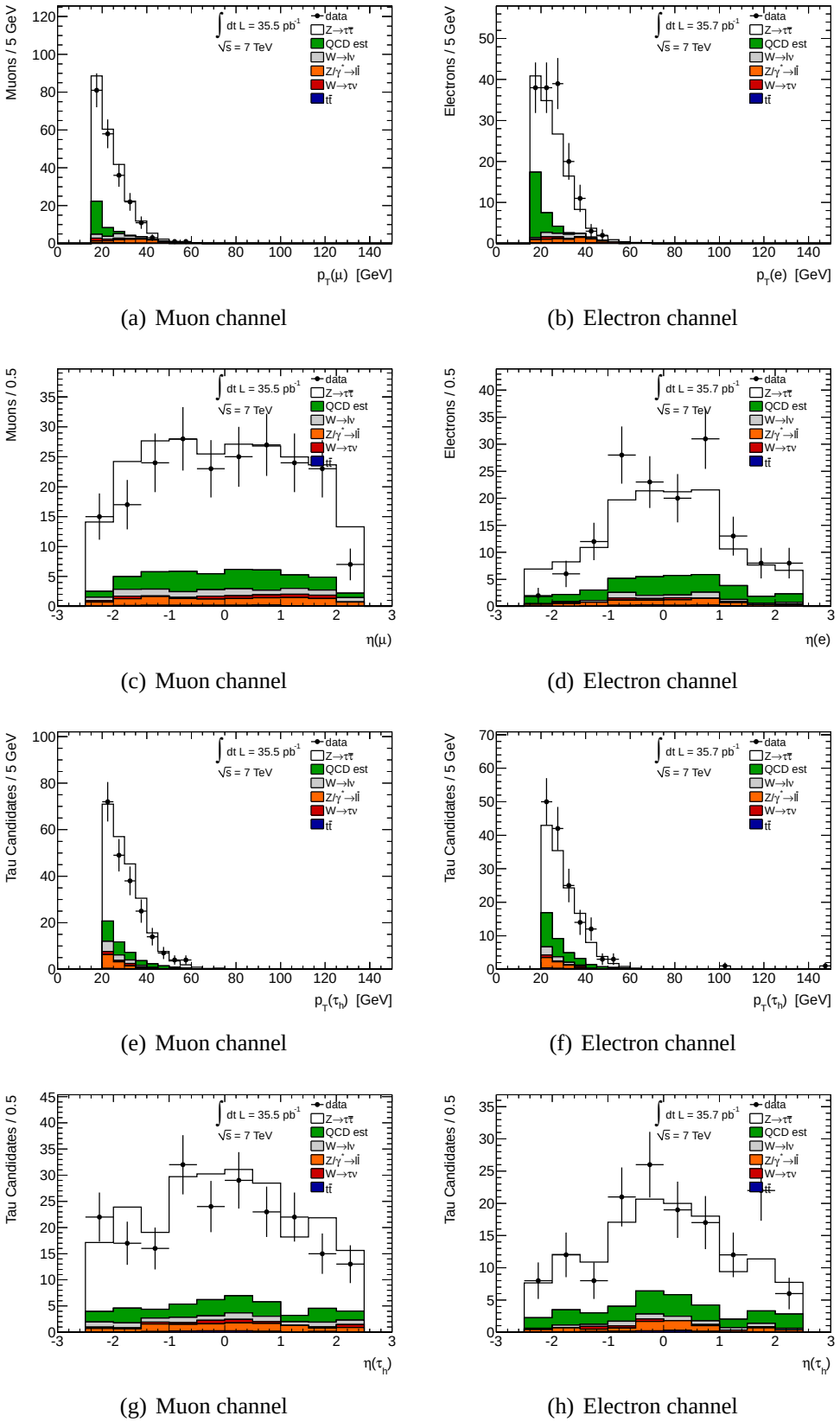

(a) Muon channel (b) Electron channel

(c) Muon channel (d) Electron channel

(e) Muon channel (f) Electron channel

(g) Muon channel (h) Electron channel

Figure 5.9: Distributions of the selected lepton and τ candidate p_{T} and η, for events passing all signal selection.

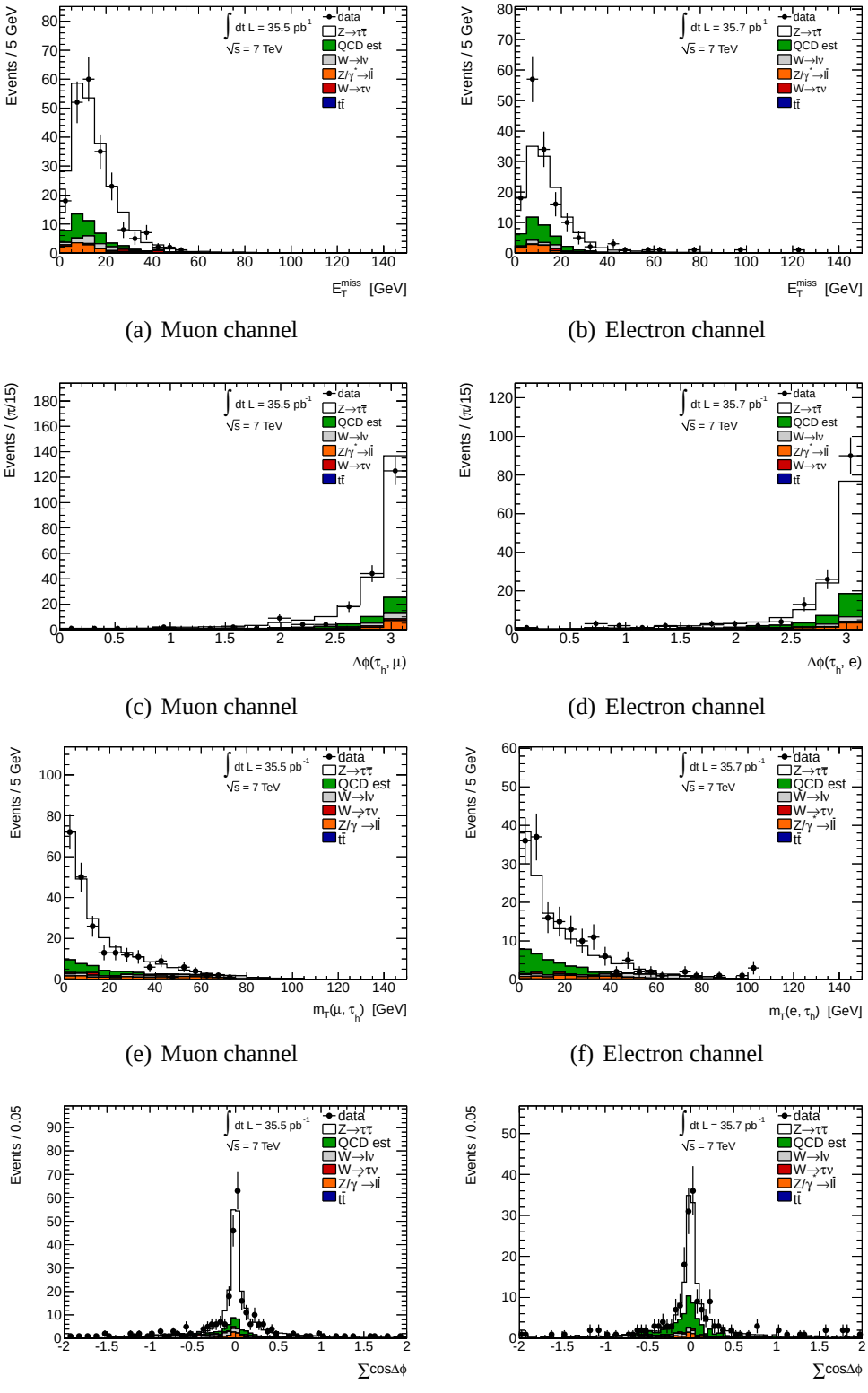

Figure 5.10: The distributions of the E_T^{miss} and $\Delta\phi$ between the selected τ candidate and lepton, in the final visible mass window for the muon (a),(c) and electron (b),(d) channels and the W suppression cuts, $\sum \cos\Delta\phi$ and m_{T} , after all other cuts applied (e), (f), (g), (h). The standard m_{T} cut was applied when plotting the $\sum \cos\Delta\phi$, while the $\sum \cos\Delta\phi$ cut was applied when plotting the m_{T}.

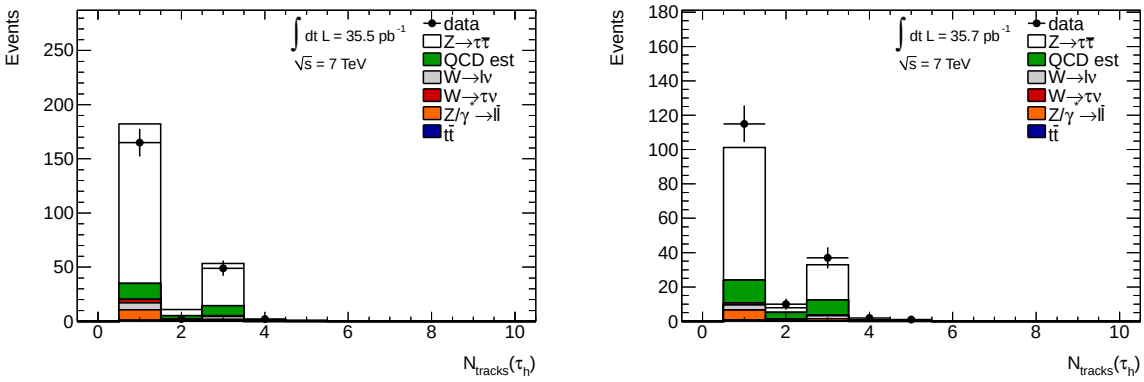

(a) Muon channel (b) Electron channel

Figure 5.11: The final track distribution after all cuts in opposite signed bin, except the requirement on the τ track distribution itself and on the magnitude of the τ charge.

tion 5.6.1. To estimate the multijet backgrounds two data-driven estimation methods were developed which served as a useful cross-check to each other. Both methods used three control regions, known as an ABCD matrix method. The primary method, the Same Sign method, used the two uncorrelated variables, lepton isolation, section 5.4.4, and the product of the charge of the electron or muon and the reconstructed τ lepton, section 5.5.3.1, to create the control regions and is described in section 5.6.2. The second method, the Non-Isolated method, used the uncorrelated lepton isolation and τ identification requirements, section 5.4.5, and is documented in section 5.6.3. To aid understanding of this procedure, the regions for both methods are shown side-by-side in a diagram format in figure 7.3. The Same Sign method was chosen as the primary method because the control regions were free from signal contamination, meaning an iterative procedure to extract the cross-section was not necessary, as would have been the case for the Non-Isolated method, which did not exclude signal contributions in the control regions.

5.6.1 W Scale Factor

The simulation has been shown to overestimate the fake rate from jets in the W + jets backgrounds [92]. By defining a W boson rich control region in data it was possible to investigate the effect of this mis-modelling by looking at a comparison of the shapes of distributions of

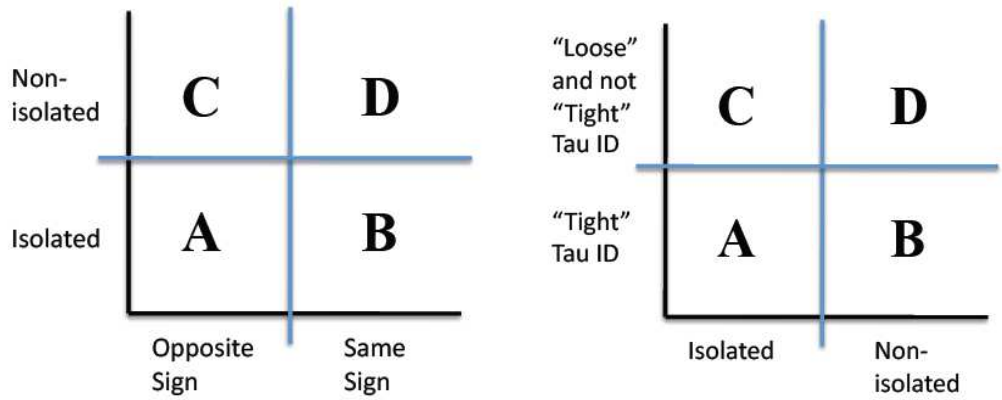

(a) Schematic diagram of the control regions for the same sign sample multijet background estimation method.

(b) Schematic diagram of the control regions for the non-isolated leptons multijet background estimation method.

Figure 5.12: Cartoon images to aid visualisations and similarities of the two background estimation methods.

data and simulation in this control region, and a scale factor k_W was assigned to correct the normalisation of the simulation to the data. To obtain this control region, both of the W + jets suppression cuts, described in section 5.5.2, were reversed, but all other event selections were applied in order to minimise contamination from the multijet background. This gave a high purity and simulation was used to estimate the contamination from other backgrounds, which was subtracted from the number of data events, as in the following equation:

$$N_W^{\mathrm{WCR}} \rightarrow k_W N_W^{\mathrm{WCR}} = N_{\mathrm{data}}^{\mathrm{WCR}} - N_{Z\rightarrow\ell\ell}^{\mathrm{WCR}} - N_{t\bar{t},diboson}^{\mathrm{WCR}} \tag{5.6}$$

In figure 5.13 the extent of this overestimation in the distributions of p_T for the light lepton and τ candidate is illustrated, before and after "tight" level τ identification was required. It is clear that the agreement between data and simulation is reasonable before the requirement of "tight" level τ identification, therefore k_W should be much closer to one for the control region where τ identification was required to be "loose" but not "tight". Different k_W factors were required for the opposite and same sign control regions, thought to be due to the different compositions of quark and gluon jets in each sample and the fact that the τ identification is modelled differently for each. The events from W + quark jet are opposite sign biased, whereas those from W +

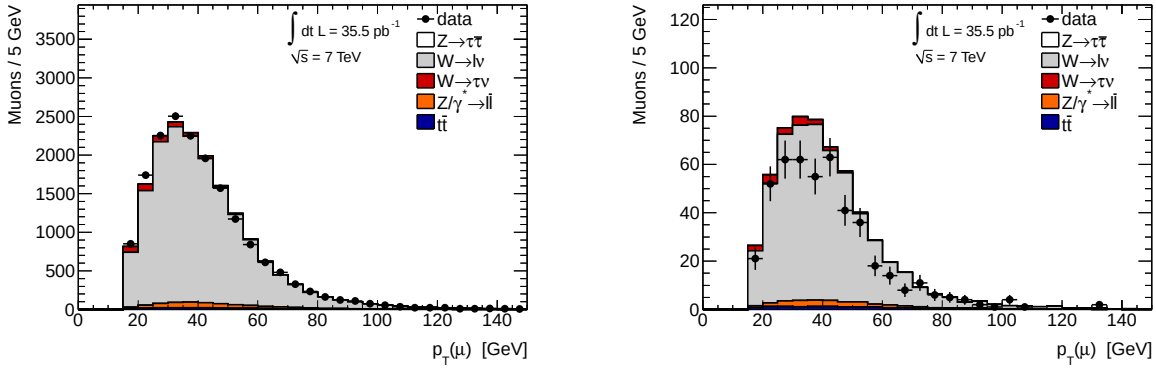

(a) No τ identification

(b) "tight" τ candidate

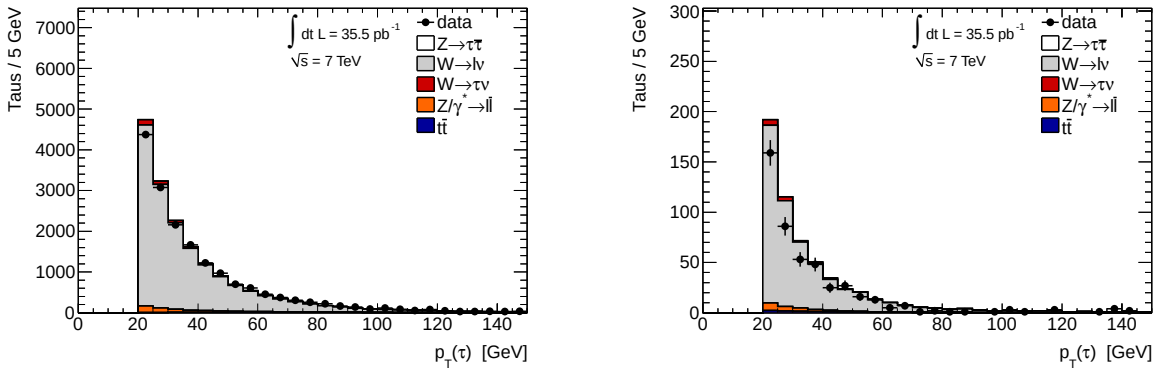

(c) No τ identification

(d) "tight" τ candidate

Figure 5.13: Muon and τ p_T distributions in the W control region, following no τ identification (a)/(c) and "tight" (b)/(d) τ identification. Following "tight" τ identification, the simulation overestimates the W contribution. A similar effect is seen in the electron channel.

gluon jet have no sign bias [93].

The measured k_W factors are listed below:

$$k_W = \begin{cases} 0.93 \pm 0.04\ (\text{stat.}) & \text{muon channel, loose + not tight } \tau, \text{ opposite sign} \\ 0.73 \pm 0.06\ (\text{stat.}) & \text{muon channel, tight } \tau, \text{ opposite sign} \\ 0.94 \pm 0.13\ (\text{stat.}) & \text{muon channel, tight } \tau, \text{ same sign} \\ 0.97 \pm 0.04\ (\text{stat.}) & \text{electron channel, loose + not tight } \tau, \text{ opposite sign} \\ 0.63 \pm 0.07\ (\text{stat.}) & \text{electron channel, tight } \tau, \text{ opposite sign} \\ 0.83 \pm 0.15\ (\text{stat.}) & \text{electron channel, tight } \tau, \text{ same sign} \end{cases} \tag{5.7}$$

These k_W factors were applied to the W + jets Monte Carlo predictions in each of the control

regions for both multijet estimation methods.

5.6.2 Background Estimation from Same Sign Sample

The first method for the multijet background estimation takes advantage of the fact that the multijet background is expected to be approximately the same regardless of whether the lepton and the τ candidate have the same or the opposite sign charge. The following relation can be used:

$$\frac{N^{A}_{\text{multijets}}}{N^{B}_{\text{multijets}}} = \frac{N^{C}_{\text{multijets}}}{N^{D}_{\text{multijets}}} \tag{5.8}$$

where N is the number of multijet events in four statistically independent regions, denoted $\{A, B, C, D\}$ and defined as follows:

- A: signal region with isolated lepton and the opposite sign requirement
- B: control region with isolated lepton and the opposite sign requirement reversed
- C: control region with inverted lepton isolation requirement and the opposite sign requirement
- D: control region with the opposite sign and isolation requirements inverted

This method takes advantage of the fact that the signal was composed of almost exclusively isolated leptons whose charges are of opposite value to those of the τ candidates, therefore signal contributions were effectively excluded in all control regions B, C and D.

All four regions have the same cuts applied except for the opposite sign and isolation requirements, keeping this method simple and reducing the number of systematic uncertainties. In each of the control regions an estimate for the number of multijet events was obtained by correcting for the $Z \to \ell\ell$, $t\bar{t}$ and di-boson contributions as predicted from simulation and for the $W \to \ell\nu$ and $W \to \tau\nu$ contributions by correcting the simulation predictions using the k_W

normalisation factors discussed in section 5.6.1 as described by the equation:

$$N^i_{multijets} = N^i_{Data} - N^i_{Z\to\tau\tau} - N^i_{Z\to\ell\ell} - N^i_{t\bar{t},diboson} - k_W(N^i_{W\to\ell\nu} + N^i_{W\to\tau\nu}) \quad \text{for } i = \mathrm{B}, \mathrm{C}, \mathrm{D} \tag{5.9}$$

The leptons from the backgrounds $W \to \ell\nu$, $W \to \tau\nu$ and $Z \to \ell\ell$ are typically very isolated, like the signal, as discussed in section 5.4.4. From simulation estimations, regions C and D are ∼99% multijet pure. These multijet rich regions were used to measure the OS/SS ratio R_{OSSS} for multijets, which was expected to be very close to unity:

$$R_{\mathrm{OSSS}} = \begin{cases} 1.07 \pm 0.04\ (\mathrm{stat.}) \pm 0.04\ (\mathrm{syst.}) & \text{muon channel} \\ 1.07 \pm 0.07\ (\mathrm{stat.}) \pm 0.07\ (\mathrm{syst.}) & \text{electron channel} \end{cases} \tag{5.10}$$

This measured R_{OSSS} was then used to scale the multijet estimate from region B to region A, using Eq. 5.11:

$$N^A_{\mathrm{multijets}} = \frac{N^C_{\mathrm{multijets}}}{N^D_{\mathrm{multijets}}} N^B_{\mathrm{multijets}} = R_{\mathrm{OSSS}} N^B_{\mathrm{multijets}} \tag{5.11}$$

These regions yielded the numbers shown in table 5.13. The expected number of multijet events in the signal region A was

$$N^A_{\mathrm{multijets}} = \begin{cases} 24 \pm 6\ (\mathrm{stat.}) \pm 3\ (\mathrm{syst.}) & \text{muon channel} \\ 23 \pm 6\ (\mathrm{stat.}) \pm 3\ (\mathrm{syst.}) & \text{electron channel} \end{cases} \tag{5.12}$$

This method is limited by low statistics in the control region. Investigations of the effect of possible systematic uncertainties were performed and are described in section 6.1.2.1.

5.6.3 Background Estimation from Non-Isolated Leptons

The second method used the lepton isolation and the τ candidate identification to define the control regions as they are expected to be uncorrelated. Specifying “loose” but not “tight”

		Muon channel		Electron channel	
		Isolated Lepton	Non-Isolated Lepton	Isolated Lepton	Non-isolated Lepton
		Region A	Region B	Region A	Region B
	Data	213(15)	1521(39)	151(12)	398(20)
	$Z \to \tau\tau$	185(2)	8.4(4)	97(1)	3.2(2)
	$\gamma^*/Z \to \tau\tau$	0.7(3)	0.05(5)	0.3(2)	0(0)
OS Events	Multijet	24(6)	1511(39)	23(6)	394(20)
+ Final Selection	$W \to \ell\nu$	9.3(7)	0.3(1)	4.8(4)	0.2(1)
	$W \to \tau\nu$	3.6(8)	0.08(8)	1.5(4)	0.04(4)
	$Z \to \ell\ell$	8.7(3)	0.33(6)	4.9(2)	0.12(3)
	$\gamma^*/Z \to \ell\ell$	2.4(4)	0.16(8)	2.0(3)	0.03(3)
	$t\bar{t}$	1.31(1)	0.99(8)	1.02(8)	0.11(3)
	Di-boson	0.28(2)	0.052(8)	0.18(1)	0.009(3)
		Region C	Region D	Region C	Region D
	Data	34(6)	1415(38)	29(5)	367(19)
	$Z \to \tau\tau$	1.3(2)	0.3(8)	1.0(1)	0.23(7)
	$\gamma^*/Z \to \tau\tau$	0.06(6)	0.09(9)	0.2(1)	0(0)
SS Events	Multijet	22(6)	1413(38)	21(5)	367(19)
+ Final Selection	$W \to \ell\nu$	3.7(5)	0.09(6)	2.3(3)	0(0)
	$W \to \tau\nu$	2.1(7)	0.2(2)	0.3(3)	0(0)
	$Z \to \ell\ell$	1.9(1)	0.11(3)	2.7(3)	0.05(2)
	$\gamma^*/Z \to \ell\ell$	2.5(4)	0.11(8)	1.3(3)	0.13(11)
	$t\bar{t}$	0.21(4)	0.61(6)	0.1(3)	0.06(18)
	Di-boson	0.044(7)	0.021(4)	0.029(5)	0.005(3)

Table 5.13: Numbers of events in the control regions discussed in section 5.6.2. The numbers in parenthesis are the statistical errors in the least significant digits. The multijet expectations were determined by the data-driven method discussed in that section. The other processes were estimated with simulation.

τ identification helped to ensure high numbers of multijet candidates. The four independent regions are defined as:

- A: signal region with isolated lepton and "tight" τ candidate
- B: control region with non-isolated lepton and "tight" τ candidate
- C: control region with isolated lepton and "loose" but not "tight" τ candidate
- D: control region with non-isolated lepton and "loose" but not "tight" τ candidate

The control regions C and D were used to measure a ratio of isolated to non-isolated multijet events R_{iso}, which were then used to normalise the number of multijet events in region B, to give the number of multijet events expected to fall within the signal region A, as in the following

		Muon channel		Electron channel	
		Isolated Lepton	Non-isolated Lepton	Isolated Lepton	Non-isolated Lepton
		Region A	Region B	Region A	Region B
	Data	213(15)	1521(39)	151(12)	398(20)
	$Z \to \tau\tau$	185(2)	8.4(4)	97(1)	3.2(2)
	$\gamma^*/Z \to \tau\tau$	0.7(3)	0.05(5)	0.3(2)	0(0)
"tight" τ candidate	Multijet	23(3)	1510(39)	25(3)	394(20)
+ Final Selection	$W \to \ell\nu$	9.3(7)	0.31(12)	4.8(4)	0.2(1)
	$W \to \tau\nu$	3.6(8)	0.08(8)	1.5(4)	0.04(4)
	$Z \to \ell\ell$	8.7(3)	0.33(6)	4.9(2)	0.12(3)
	$\gamma^*/Z \to \ell\ell$	2.4(4)	0.16(8)	2.0(3)	0.03(3)
	$t\bar{t}$	1.3(1)	0.99(8)	1.02(8)	0.11(3)
	Di-boson	0.28(2)	0.052(8)	0.18(1)	0.009(3)
		Region C	Region D	Region C	Region D
	Data	283(17)	9696(98)	225(15)	2159(46)
	$Z \to \tau\tau$	72(1)	4.2(3)	39.5(8)	1.4(2)
	$\gamma^*/Z \to \tau\tau$	3(1)	0.3(2)	0	0.03(3)
"loose" not "tight"	Multijet	144(17)	9688(98)	139(15)	2156(46)
τ candidate	$W \to \ell\nu$	35(2)	1.8(3)	22(1)	0.6(2)
	$W \to \tau\nu$	11(2)	0.5(3)	7.6(1)	0
	$Z \to \ell\ell$	6.3(2)	0.28(5)	9.6(3)	0.20(4)
	$\gamma^*/Z \to \ell\ell$	7.5(7)	0.3(1)	5.2(5)	0.2(1)
	$t\bar{t}$	2.3(1)	1.07(8)	1.4(1)	0.22(4)
	Di-boson	0.31(3)	0.09(1)	0.22(2)	0.019(4)

Table 5.14: Numbers of events in the control regions discussed in section 5.6.3. The numbers in parenthesis are the statistical errors in the least significant digits. The multijet expectations are determined by the data-driven method using non-isolated leptons, discussed in that section. The other processes were estimated with simulation.

relation:

$$N^A_{\text{multijets}} = N^B_{\text{multijets}} \left(\frac{N^C_{\text{multijets}}}{N^D_{\text{multijets}}} \right) = N^B_{\text{multijets}} \, R_{\text{iso}} \tag{5.13}$$

Due to the inefficiencies in the cut-based τ identification for signal events, there was contamination from signal events as well as other backgrounds, although this was a small percentage of the total number of events in the control region. The simulation, normalised to the theoretical cross-section, was used to correct for this contamination using this relation:

$$N^i_{multijets} = N^i_{Data} - N^i_{Z\to\tau\tau} - N^i_{Z\to\ell\ell} - N^i_{t\bar{t},diboson} - k_W(N^i_{W\to\ell\nu} + N^i_{W\to\tau\nu}) \quad \text{for } i = \text{B, C, D} \tag{5.14}$$

where k_W is detailed in section 5.6.1. The total estimated number of events from data and each background, in each region, is detailed in table 5.14. This method estimated the following numbers of multijet events in the signal region A to be:

$$N^{A}_{\text{multijets}} = \begin{cases} 23 \pm 3\,(\text{stat.}) \pm 4\,(\text{syst.}) & \text{muon channel} \\ 25 \pm 3\,(\text{stat.}) \pm 3\,(\text{syst.}) & \text{electron channel} \end{cases} \tag{5.15}$$

The number of the estimated multijet events is in good agreement with values obtained from the method based on the same sign sample: 24 $\pm$ 6(stat.) $\pm$ 3(syst.) events from multijet processes in the muon channel and 23 $\pm$ 6(stat.) $\pm$ 4(syst.) in the electron channel as presented in the previous section.

5.7 Cross-section Calculation

The measurement of the cross-sections was performed using the formula

$$\sigma(Z \to \tau\tau) \times BR(\tau \to l\,\nu\,\nu, \tau \to \tau_{had}\,\nu) = \frac{N_{obs} - N_{bkg}}{A_Z \cdot C_Z \cdot \mathcal{L}} \tag{5.16}$$

where

- N_{obs} is the number of observed events in data
- N_{bkg} is the number of estimated background events
- A_Z denotes the kinematic and geometric acceptance for the signal process
- C_Z is a factor containing the efficiencies for triggering, reconstruction and identification objects within the fiducial region
- $\mathcal{L}$ denotes the integrated luminosity for the channel of interest

A_Z is determined from generator level Monte Carlo as:

$$A_Z = \frac{N_{dressed}^{gen\,kin}}{N_{born}^{gen\,m_{inv}}} \tag{5.17}$$

where $N_{born}^{gen\,m_{inv}}$ is the number of generated events at Born level, meaning before the leptons emit photons via QED final-state radiation, which fall within the invariant mass window of 66-116 GeV and $N_{dressed}^{gen\,kin}$ is the number of generated events which when dressed, fall within the fiducial regions summarised below. The procedure of dressing events is a partial way to correct back to Born level. The τ lepton decay products were "dressed" with photons radiated by the τ leptons themselves and the decay products, this was done using a cone of $\Delta R < 0.1$ for electrons and muons and $\Delta R < 0.4$ for hadronic decay products to select photons to add to the τ lepton decay products.

The A_Z values were calculated using a PYTHIA sample generated with a modified LO parton distribution function (PDF) MRSTLO* [94][2]and the ATLAS MC10 tune [79]. By construction the A_Z factor includes a correction for events which migrate inside the invariant mass window in the fiducial region, including events from the low mass tail (above 10 GeV) from $\gamma^\star/Z$ processes. The values are shown in table 5.15, the difference between channels can be attributed to the difference in η ranges essentially, in the electron channel the crack region is excluded. The statistical uncertainty on both values is ∼2%.

C_Z is defined as follows:

$$C_Z = \frac{N^{reco\,pass}}{N_{dressed}^{gen\,kin}} \tag{5.18}$$

where $N^{reco\,pass}$ is the number of events which pass all cuts after all of the correction factors, to correct simulation to data, have been applied. $N_{dressed}^{gen\,kin}$ is defined in the same way as above. By construction the correction for events migrating into the acceptance is included. For the C_Z values the statistical uncertainties are ∼1.5%.

[2]The * indicates that this PDF is modified and designed to be used in conjunction with a LO matrix element, required due to flaws in either the standard LO or NLO PDFs, this PDF is optimised to perform better than either [94].

	Muon channel	Electron channel
A_Z	0.11691 $\pm$ 0.00023(stat.)	0.10073 $\pm$ 0.00021(stat.)
C_Z	0.2045 $\pm$ 0.0024(stat.)	0.1197 $\pm$ 0.0017(stat.)

Table 5.15: Central values for the A_Z acceptance factor defined by equation 5.17 from PYTHIA ATLAS MC10 Monte Carlo generated with MRSTLO* PDF at generator level and C_Z correction factor defined by equation 5.18 determined using the same sample at generator level and after full detector simulation.

The cross-sections defined by equation 5.16 are total inclusive cross-sections. The fiducial cross-sections are obtained by setting A_Z to one, which gives:

$$\sigma^{fid}(Z \to \tau\tau) \times BR(\tau \to l\,\nu\,\nu,\ \tau \to\ had\,\nu) = \frac{N_{obs} - N_{bkg}}{C_Z \cdot \mathcal{L}} \tag{5.19}$$

Measuring the fiducial cross-sections removes some of the theoretical uncertainties from the measurement.

The fiducial regions were defined by the following cuts:

Muon channel

- Muon: $p_T > 15$ GeV, $|\eta| < 2.4$
- Tau: $E_T > 20$ GeV, $|\eta| < 2.47$, excluding $1.37 < |\eta| < 1.52$
- Event: $\Sigma \cos\Delta\phi >$ -0.15, $m_{\mathrm{T}} <$ 50 GeV, $35 < m_{\mathrm{vis}} <$ 75 GeV

Electron channel

- Electron: $E_T > 16$ GeV, $|\eta| < 2.47$, excluding $1.37 < |\eta| < 1.52$
- Tau: $E_T > 20$ GeV, $|\eta| < 2.47$, excluding $1.37 < |\eta| < 1.52$
- Event: $\Sigma \cos\Delta\phi >$ -0.15, $m_{\mathrm{T}} <$ 50 GeV, $35 < m_{\mathrm{vis}} <$ 75 GeV

5.8 Z Candidates and Backgrounds after Event Selection

A summary of the number of events passing the selection in data and for the multijet background, estimated using the both methods, detailed in section 5.6.2 and section 5.6.3, along with the estimated number of events from each of the other electroweak backgrounds is presented in table 5.16. Since the Same Sign method was chosen as the primary method the measurement of the cross-section is performed using this method, however both are included here to enable the reader to draw a comparison. The number of events that were seen, after subtracting the number of events estimated to be from backgrounds is: 164 $\pm$ 16(stat.) $\pm$ 4(syst.) for the muon channel and 114 $\pm$ 14(stat.) $\pm$ 3(syst.) for the electron channel. This is compatible with the Standard Model signal expectations of 186.2 $\pm$ 2.1(stat.) $\pm$ 25.7(syst.) and 97.8 $\pm$ 1.4(stat.) $\pm$ 16.2(syst.) events respectively.

	Muon channel (35.5 pb^{-1})	Electron channel (35.7 pb^{-1})
Data (after all selections)	213	151
Est. multijet background OS/SS	24 $\pm$ 6(stat.) $\pm$ 3(syst.)	23 $\pm$ 6(stat.) $\pm$ 3(syst.)
Est. multijet background isol. lep.	23 $\pm$ 3(stat.) $\pm$ 4 (syst.)	25 $\pm$ 3(stat.) $\pm$ 3 (syst.)
Est. $W, Z, t\bar{t}$, diboson background	25 $\pm$ 1(stat.) $\pm$ 5(syst.)	14 $\pm$ 1(stat.) $\pm$ 4(syst.)
Data (less backgrounds, OS/SS)	164 $\pm$ 16(stat.)$\pm$4(syst.)	114 $\pm$ 14(stat.)$\pm$3(syst.)
Data (less backgrounds, isol. lep.)	164 $\pm$ 13(stat.) $\pm$ 5(syst.)	111 $\pm$ 11(stat.) $\pm$ 4(syst.)
SM signal expectation	186.2 $\pm$ 2.1(stat.) $\pm$ 25.7(syst.)	97.8 $\pm$ 1.4(stat.) $\pm$ 16.2(syst.)

Table 5.16: Summary of $Z \rightarrow \tau\tau$ observation results: observed number of events in data, estimated background and number of data events after subtracting the estimated background compared to the SM signal expectation. OS/SS and Isol. Lep. refer to the two multijet background estimation methods, described in sections 5.6.2 and 5.6.3 respectively.

Chapter 6

$Z \to \tau_\ell \tau_h$ Cross-section Measurement: Results and Systematics

6.1 Systematics

The systematic uncertainties were estimated for the calculations of the A_Z factor, the geometric and kinematic acceptance, and the C_Z factor, containing the efficiencies for triggering and reconstruction and identification of objects in the fiducial region, as well as for the background estimations. There are two categories of uncertainties for the background estimations, the first type are the uncertainties associated with the simulation predictions for the electroweak background including those used to correct the contamination in the control regions for the data-driven estimates; the second are the uncertainties associated with the data-driven method itself. The systematic uncertainties on the simulation predictions used to correct for the contamination in the control regions, in both background estimation methods, were propagated into the multijet estimates. Some systematic uncertainties were investigated in dedicated studies outside of this analysis; where values are used from those studies, references are given to the full details.

6.1.1 Systematic Uncertainties on Monte Carlo Predictions

6.1.1.1 Pile-up

To correctly model the pile-up in the simulation, the vertex distributions need to be reweighted to match those in the data, details of this are in section 5.2.3. The effect that the pile-up had on the quantities used in this analysis was most evident in cell-based variables such as R_{EM} of the

τ candidates and the E_TCone variable used for the lepton isolation, discussed in section 5.4.4. Both of these variables are shown in figure 6.1 with various pileup conditions. The distributions of τ candidates were taken from simulation. The muons used for the isolation distributions were taken from the tag and probe analysis described in section 6.1.1.7.

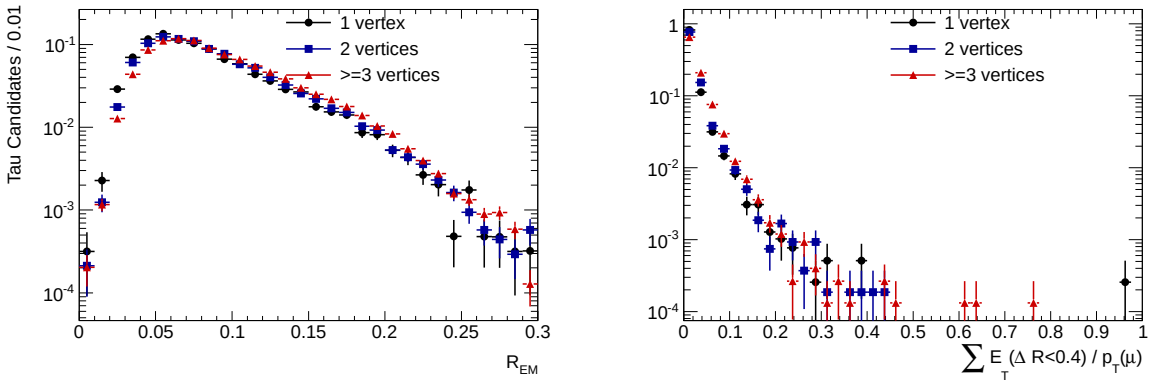

(a) (b)

Figure 6.1: The τ candidate electromagnetic radius was plotted from simulated signal events in (a) and the E_TCone variable of isolated muons from $Z \to \mu\mu$ events in data in (b), both show a comparison of the variable in events with different numbers of vertices: one, two and three and above.

The systematic uncertainty was estimated by varying the weights used up and down by 1σ within the statistical uncertainty and measuring the percentage change in the final event yield for each simulation sample. The results of this procedure can be seen in table 6.1.

Shift	$Z \to \tau\tau$	$Z \to ee$ ($m_{\ell\ell} > 60$ GeV)	$Z \to \mu\mu$ ($m_{\ell\ell} > 60$ GeV)	$t\bar{t}$
$+1\sigma$	+0.35%	+0.35%	+0.35%	+0.35%
-1σ	-0.35%	-0.35%	-0.35%	-0.35%

Table 6.1: The percentage change in event yield when the pile-up weights were shifted up and down by 1σ on each simulated sample.

6.1.1.2 Energy Scale and E_T^{miss} Scale

The uncertainty due to the τ energy scale was assessed by scaling the energy of each τ candidate in the event and measuring the percentage change in the final event yield. The scale factors were binned in p_T, η and the number of prongs of the τ candidate, the scale factors used are given in table 6.2 [45].

	1-Prong ($\|\eta\|$ Regions)			Multi-Prong ($\|\eta\|$ Regions)		
p_T Region	< 1.3	1.3 - 1.6	> 1.6	< 1.3	1.3 - 1.6	> 1.6
$15 < p_T < 20$ GeV	4.5%	7.0%	4.5%	14.0%	7.0%	6.5%
$20 < p_T < 30$ GeV	3.5%	7.0%	4.5%	10.0%	7.0%	6.5%
$p_T > 30$ GeV	2.5%	7.0%	4.5%	8.0%	7.0%	6.5%

Table 6.2: Scale factors used for rescaling τ candidates' energy up and down.

Since they are correlated the E_T^{miss} and the electron energy must be scaled at the same time. For the muons, the energy smearing was studied independently and found to be negligible. Before the preselection of τ candidates and electrons, the energies of all the τ and electron candidates in the event were scaled either up or down and the change in electron energy was propagated into the calculation of E_T^{miss}, which is described in section 5.4.6. Then all other topoclusters in the event not within $\Delta R < 0.2$ of the selected lepton were scaled up or down according to the formula: $1 + a\left(1 + \frac{N-1}{p_T}\right)$ within $|\eta| < 3.2$, where a and N are chosen to cover the full range of uncertainties derived from studies of E/p in data and Monte Carlo for single hadrons [95] [96]. In figure 6.2 the distributions of E_T^{miss} and τ candidate p_T are shown, for the default values and once the clusters have been scaled both up and down in energy. The value of the systematic uncertainty per simulation sample was defined as the maximum shift in event yield for any value of a or N. These shifts are summarised in table 6.3, the maximal values used as the systematics were 9.44(8.55)% for the signal simulation, 29(24)%, 21(18)% and 13(18)% for the $Z \to \ell\ell$, $W \to \ell\nu$, and $t\bar{t}$ backgrounds respectively in the electron (muon) channel.

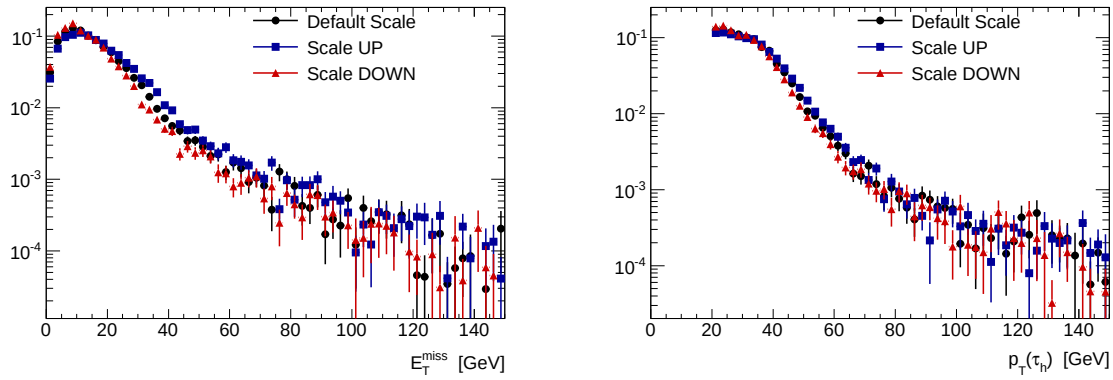

(a) (b)

Figure 6.2: The variables E_T^{miss} in (a) and τ p_T in (b) before and after scaling the cluster energy up and down.

Shift	$Z \to \tau\tau(e)$	$Z \to ee$	$W+$ jets	$t\bar{t}$
a=0.07, N-1=0.93	9.39	29	21.1	10.6
a=0.06, N-1=1.17	9.21	27	20	11
a=0.05, N-1=1.50	9.16	24	18.6	10.2
a=-0.05, N-1=1.50	-9.1	-4.11	-8.74	-12.5
a=-0.06, N-1=1.17	-9.26	-4.58	-9.07	-12.9
a=-0.07, N-1=0.93	-9.44	-5.7	-10.1	-13
Cluster $\|\eta\| > 3.2$				
a=1.1, N-1=0	-0.154	1.88	-2.15	1.63
a=0.9, N-1=0	-0.246	-0.803	-3.36	-0.0744
Shift	$Z \to \tau\tau(\mu)$	$Z \to \mu\mu$	$W+$ jets	$t\bar{t}$
a=0.07, N-1=0.93	7.54	24.3	18.1	17.8
a=0.06, N-1=1.17	7.5	24.1	17.9	17.6
a=0.05, N-1=1.50	7.4	23.6	18.1	17.9
a=-0.05, N-1=1.50	-8.24	-17.9	-18.5	-13.5
a=-0.06, N-1=1.17	-8.42	-19.2	-18.4	-14
a=-0.07, N-1=0.93	-8.55	-20.1	-18.4	-14.7
Cluster $\|\eta\| > 3.2$				
a=1.1, N-1=0	0.0517	-0.04	-0.0895	0.129
a=0.9, N-1=0	-0.0501	0.617	-3.71	1.5

Table 6.3: The percentage difference in event yield after the cluster energies and τ energy were shifted. In the electron channel the electron energy was also scaled.

6.1.1.3 Lepton Trigger Efficiency

Trigger efficiencies were measured using a tag and probe analysis. The efficiencies were calculated in both data and simulation, with respect to reconstructed and identified leptons. The ratio of the efficiency in data and simulation yields the correction factor which was applied to the simulation to achieve agreement with data.

Muons Using the $Z \to \mu\mu$ tag and probe analysis, the trigger efficiency was measured as a function of η and p_T; the trigger efficiency as a function of these two variables can be seen in figure 6.3. The trigger efficiency is flat after the turn-on at $p_T > 15$ GeV with respect to p_T and therefore the correction factors were only computed as a function of η. The η dependence is due to the non-homogeneity of the muon detectors. In the end-cap region there are muon trigger chambers covering the full extent of the muon spectrometers and therefore the trigger efficiencies are higher at $> 95\%$, in the barrel region there are some missing and therefore

the trigger efficiency can be as low as 80%. This drops even further in the transition region at $|\eta| \sim 1.2$. By varying the parameters of the tag and probe analysis, such as the size of the invariant mass window, the systematic uncertainties on these efficiency measurements were estimated. The summary of these integrated trigger efficiencies and the following correction factors for each of the triggers used in this cross-section measurement are given in table 6.4 and table 6.5 respectively.

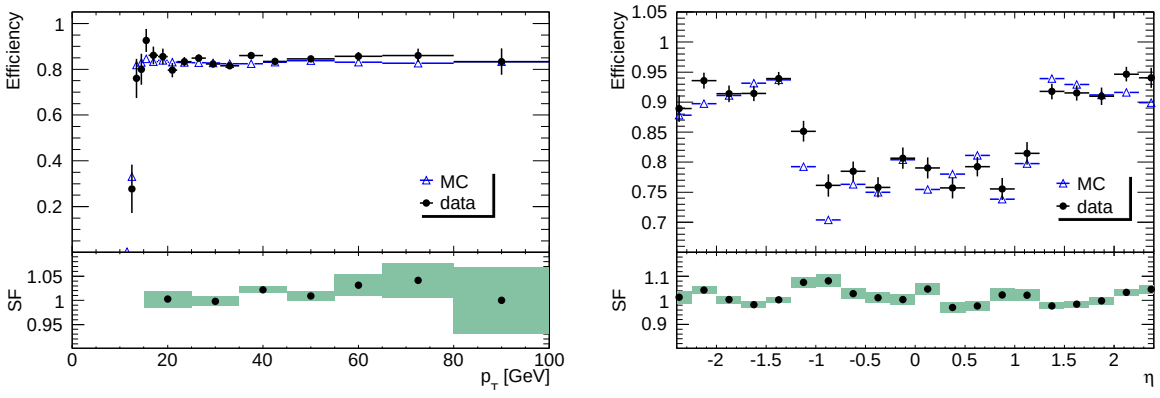

(a) (b)

Figure 6.3: Trigger efficiency and scale factors measured in data and simulation, for the mu13MG_tight trigger, where the green bands represent the uncertainty on the scale factors.

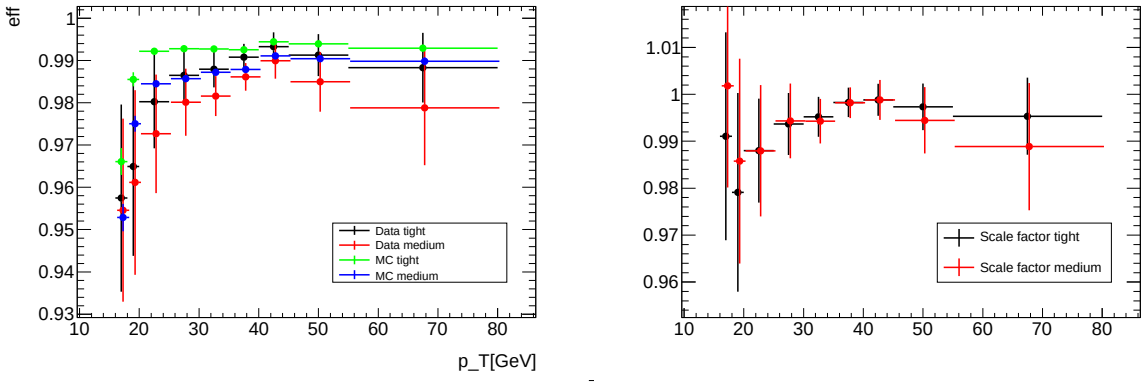

(a) (b)

Figure 6.4: Trigger efficiency for the e15_medium trigger at EF level in (a) measured in $W \rightarrow e\nu$ data events and simulation. Scale factors for the e15_medium trigger at EF level in (b) for medium and tight level electrons.

Electrons For electrons the trigger efficiency was measured using two different methods. The first, for offline electrons with $p_T > 20$ GeV, was a combination of the results of two tag and

Trigger Flag Type	Efficiency	
	Data	Simulation
EF_mu10MG	82.79 ± 0.92 (stat.) ± 0.31 (syst.) %	82.55 ± 0.02 (stat.) ± 0.02 (syst.) %
EF_mu13MG	84.48 ± 0.40 (stat.) ± 0.13 (syst.) %	82.55 ± 0.02 (stat.) ± 0.02 (syst.) %
EF_mu13MG_tight	83.07 ± 0.39 (stat.) ± 0.14 (syst.) %	82.05± 0.02 (stat.) ± 0.02 (syst.) %

Table 6.4: Integrated efficiency for each muon trigger threshold, measured with respect to reconstructed and identified muons.

Trigger Flag Type	Scale Factor
EF_mu10MG	1.003 ± 0.011
EF_mu13MG	1.024 ± 0.005
EF_mu13MG_tight	1.013 ± 0.005

Table 6.5: The scale factors for each muon trigger threshold, used to correct the trigger efficiencies measured in simulation to those measured in data.

Electron Type	p_T Range Threshold	Efficiency	
		Data	Simulation
"medium"	$16 < E_T < 18$ GeV	95.7 ± 2.4 (stat.) ± 0.3 (syst.) %	95.3 ± 0.3 (stat.) %
"tight"	$16 < E_T < 18$ GeV	95.8 ± 2.2 (stat.) ± 0.6 (syst.) %	96.6 ± 0.3 (syst.) %
"medium"	$18 < E_T < 20$ GeV	96.3 ± 2.2 (stat.) ± 0.4 (syst.) %	97.50 ± 0.16 (stat.) %
"tight"	$18 < E_T < 20$ GeV	96.5 ± 2.1 (stat.) ± 0.4 (syst.) %	98.55 ± 0.16 (stat.) %

Table 6.6: The trigger efficiencies for the e15_medium trigger in two different p_T ranges for "medium" and "tight" electrons, measured from a $W \rightarrow e\nu$ tag and probe data analysis. For the region of $p_T > 20$ GeV, the scale factor of 0.995 was used.

probe analyses, one using $Z \rightarrow ee$ events and the other using $W \rightarrow e\nu$ events. This gave the correction factor of 0.995 ± 0.005 [60, 97]. Electrons with $p_T > 20$ GeV are on the plateau, thus no p_T binning was required as the efficiencies are flat with respect to p_T. The second is for offline electrons with $p_T < 20$ GeV, and was measured using a tag and probe analysis on $W \rightarrow e\nu$ events. For this momentum range the efficiencies were binned in two p_T bins, 16-18 GeV and 18-20 GeV since the trigger is turning on in this p_T range. These efficiencies are listed in table 6.6. The scale factors obtained using this method are summarised in table 6.7 [64]. The efficiencies measured for the e15_medium trigger at Event Filter level using the second method can be seen in figure 6.4 along with the corresponding scale factors.

Electron Type	p_T Range Threshold	Scale Factor
"medium"	$16 < E_T < 18$ GeV	1.004 ± 0.025
"tight"	$16 < E_T < 18$ GeV	0.992 ± 0.023
"medium"	$18 < E_T < 20$ GeV	0.987 ± 0.023
"tight"	$18 < E_T < 20$ GeV	0.979 ± 0.021

Table 6.7: The scale factors for the e15_medium trigger in two different p_T bins for "medium" and "tight" electrons, used to correct the trigger efficiencies in simulation to those measured in data.

6.1.1.4 Lepton Reconstruction and Identification Efficiency

Muons The $Z \to \mu\mu$ tag and probe analysis was used to measure the efficiency of the muon reconstruction and identification for both data and simulation [98]. While the efficiencies were found not to be dependent on p_T, the combined muon reconstruction and identification efficiencies varied depending on the region in the detector. Therefore the simulation to data scale factors, were binned in different regions of $\eta - \phi$ space, and can be found in [98]. The systematic uncertainties on these scale factors were estimated by varying the requirements of the $Z \to \mu\mu$ tag and probe analysis.

Electrons Tag and probe studies were used to show that the electron reconstruction efficiencies were well modelled in simulation and that no scale factor was necessary [97]. The systematic uncertainty assigned to this measurement was 1.5%.

The efficiencies for the identification of electrons in simulation and data were measured using tag and probe analyses performed on $Z \to ee$ and $W \to e\nu$ events , the disagreement between simulation and data was corrected for by defining scale factors, dependent on η and p_T. These dependencies were found to be uncorrelated, so the two scale factors, one binned in η, the other in p_T, were multiplied together to give the final scale factors. The individual scale factors and the uncertainties on these measurements can be found in [60, 97].

6.1.1.5 Lepton p_T Resolution

To achieve agreement between data and simulation for the $Z \to \ell\ell$ mass peak, smearing was applied to the lepton p_T in the simulated events. To estimate the systematic uncertainty on this correction procedure the smearing factor was varied by one σ and the percentage change was found to be only 0.2%.

6.1.1.6 Lepton Charge Misidentification

The mis-identification of lepton charge typically occurs after showering of electrons; due to the large number of charged tracks in the vicinity of the electron, it is easier to combine the wrong track with the electron. This effect was measured by looking at $Z \to ee$ events, selected in a tag and probe analysis, and comparing the number of events where both electrons had the same electric charge to the total number of events. The systematic uncertainty on this measurement was measured to be 0.2%. For muon events the charge-misidentification rate for this analysis was found to be negligible.

6.1.1.7 Lepton Isolation

The efficiency of the isolation requirements placed on the selected leptons, discussed in section 5.4.4, was measured using $Z \to \ell\ell$ tag and probe analyses. The efficiency is defined as the percentage of selected leptons which also pass the isolation requirements. By taking the ratio of the efficiencies measured in data and simulation, correction factors were obtained which were then applied to the simulation.

Muons The $Z \to \mu\mu$ tag and probe analysis was used to measure the efficiency of the isolation requirements. This was found to be dependent on p_T but not η, this dependence is illustrated in figure 6.5(a); This was modelled well by simulation and the scale factors were consistently around one. The scale factors were applied in p_T bins, the systematic uncertainties were calculated independently per bin, by varying the tag and probe requirements.

Electrons A $Z \rightarrow ee$ tag and probe analysis was performed to measure the efficiencies of the isolation requirements on selected electrons. The same identification criteria for the electrons as used in the analysis, were used for the tag electron and all except the isolation criteria were used for the probe electron. In addition to this the electrons were required to have opposite sign electric charge and fall within an invariant mass window around that of the Z boson. No background subtraction was found to be necessary as the tight selection criteria on the tag electron combined with the invariant mass window of the two electrons was highly effective at suppressing the multijet background to $\sim$1%. The efficiencies were calculated in bins of p_T and η independently, the distributions of these dependencies can be seen in figures 6.5(b) and 6.5(d) respectively. These were found to be non-correlated, therefore to get the final scale factors, the scale factors in bins of p_T and η were multiplied together. The systematic uncertainties on these scale factors were estimated on a bin-by-bin basis by varying the tag and probe requirements such as electron identification level, invariant mass window size and minimum p_T of the tag electron.

6.1.1.8 τ Identification Efficiency

To evaluate the efficiencies and associated systematic uncertainties on the cut-based τ identification [45] and dedicated electron veto, studies were performed on the simulation to alter conditions which affect event generation, shower modelling and reconstruction and measure the effects on the efficiency [45]. The following conditions were taken into account:

1. Detector Geometry
2. Monte Carlo event generator and underlying event model
3. Hadronic shower model
4. Noise thresholds of calorimeter cells for cluster reconstruction

The efficiencies and systematic uncertainties were measured in bins of p_T, η, number of prongs and in one or more vertices. The efficiencies and the resulting event yield shifts are

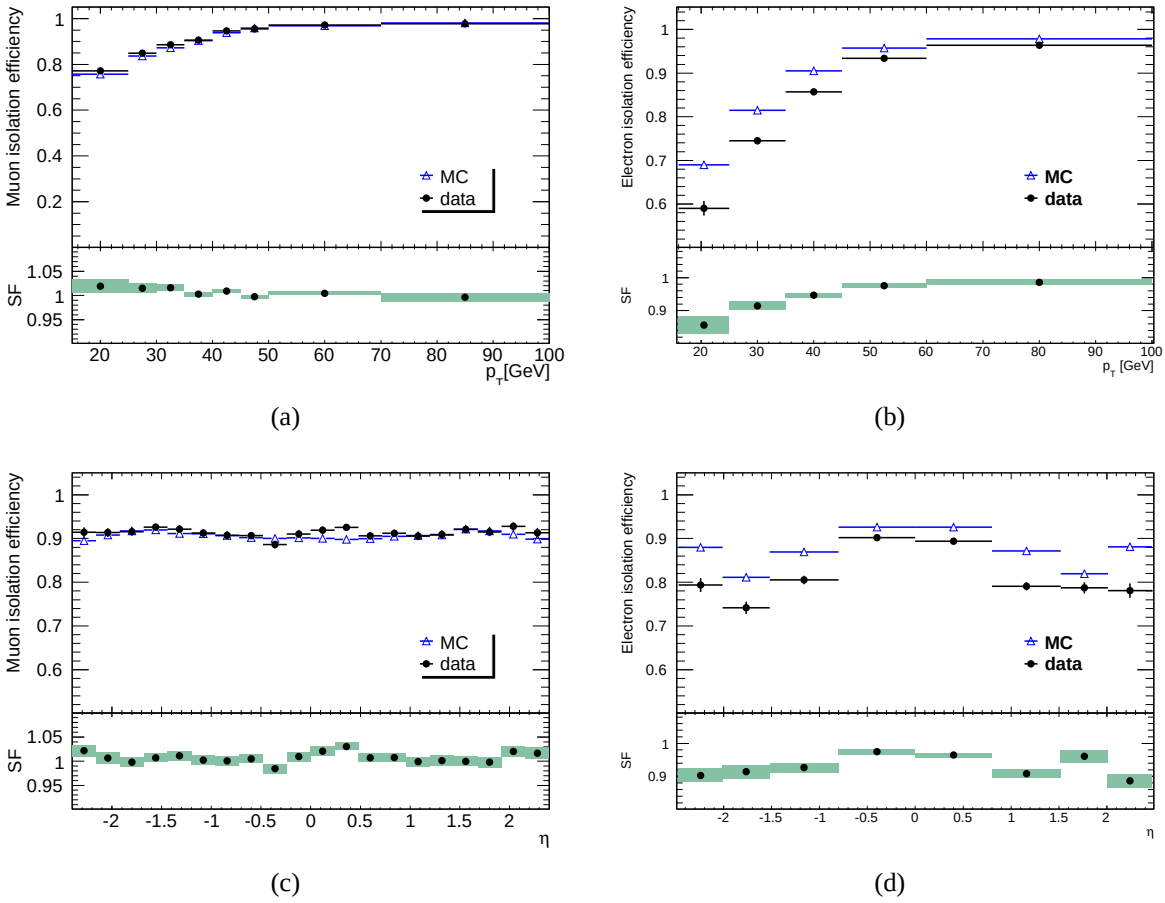

Figure 6.5: Efficiency of the isolation requirements and scale factors measured in data and simulation, for muons, p_TCone40/$p_T < 0.06$ and E_TCone40/$p_T < 0.06$, plotted against p_T in (a) and η in (c) and for electrons, p_TCone40/$p_T < 0.06$ and E_TCone30/p_T, against p_T in (b) and against η in (d), where the green bands represent the uncertainty on the scale factors.

summarised in table 6.8 where the systematic uncertainty quoted is the sum in quadrature of the effect of each variation listed above.

p_T (τ) [GeV]		[20, 30]		[30, 40]		[40, 100]	
N_{trk}	N_{vxp}	Effic. [%]	Syst. [%]	Effic. [%]	Syst. [%]	Effic. [%]	Syst. [%]
1	≤ 2	40.0±0.1	8.7±0.8	42.1±0.1	8.8±0.8	42.1±0.2	9.2±0.9
	≥ 3	31.7±0.1	11.0±0.7	34.6±0.1	10.4±0.8	35.7±0.1	9.6±0.8
3	≤ 2	23.3±0.1	12.3±2.9	29.6±0.2	8.9±1.7	34.9±0.3	11.9±2.6
	≥ 3	18.4±0.1	11.5±2.0	24.6±0.1	11.1±2.0	30.3±0.2	10.5±1.5

Table 6.8: The efficiencies of the τ lepton identification combined with the dedicated electron veto and the associated systematic uncertainties. For 1-prong τ candidates the "medium" identification is used and for 3-prong τ candidates the "tight" identification is used.

6.1.1.9 Jet Fake Rates of τ Leptons

To estimate the uncertainty on the fake rate of τ candidates from jets, the uncertainty was used from the cross-check measurement of the k_W scale factor. The k_W scale factor is a measure of the disagreement between data and simulation of the W+jets normalisation and is attributed to the jet-τ fake rate. The difference from one is added in quadrature to the uncertainty on the measurement of the k_W scale factor itself. The value of the systematic uncertainty this yielded was 24 % in the muon channel. This uncertainty was then applied to $\gamma^\star/Z \rightarrow \ell\ell$ and $t\bar{t}$ events. In the electron channel it was only applied to τ candidates which did not match true electrons in $\gamma^\star/Z \rightarrow ee$, this fake rate uncertainty of electrons faking τ candidates was estimated independently, see section 6.1.1.10. For $t\bar{t}$, where less than 2% of τ candidate fakes come from electrons, the jet fake-rate uncertainty was applied to all events.

6.1.1.10 Lepton Fake Rates of τ Leptons

A $Z \rightarrow ee$ tag and probe analysis was used to measure the fake rate of τ candidates originating from electrons in both data and simulation. A scale factor to correct the fake rates in simulation to those measured in data and the systematic uncertainty associated with this scale factor was calculated independently for one and three prong τ candidates and in bins of η for τ candidates matched to true electrons [99]. The uncertainty was applied to the $Z \rightarrow ee$ and $\gamma^\star/Z \rightarrow ee$ simulation events, weighted by the percentage of events where the τ candidate could be matched to a truth electron.

6.1.1.11 Electron Quality Maps

During the period that data were taken there were various problems within the calorimeter. It was necessary to reject electron candidates built using clusters corresponding to these problematic regions. To do this, maps were built in η and ϕ of dead and non-nominal HV regions, dead Front End Boards and isolated dead or high noise channels. These maps were updated

throughout data running and applied to data, but only one map was applied to Monte Carlo, corresponding to ∼52% of data, a systematic uncertainty due to this of 0.4% was estimated [100].

6.1.1.12 Jet Cleaning

Jets built from energy deposits not believed to be from the proton-proton collision were removed using the method detailed in section 5.3.2. Due to inconsistencies between data and simulation in the distributions of the variables used to remove these jets, an efficiency measured by the Jet/E_T^{miss} group from inclusive jet studies was applied to simulation. The effect of this on the signal event yield was taken as the systematic uncertainty, this was seen to be between 3.3% and 3.6% in the muon channel and less than 1.5% in the electron channel.

6.1.1.13 Cross-section and Luminosity

The uncertainty on the theoretical cross-sections used to normalise the Monte Carlo samples was 5% for the Z samples [101] and +7%/-9.5% for the $t\bar{t}$ sample [102]. The uncertainty on the luminosity measurement is 3.4% [78].

6.1.2 Systematic Uncertainties on QCD Background Estimation

To calculate the uncertainties on the background estimation methods, the relevant uncertainties on each of the W, Z and $t\bar{t}$ processes had to be taken into account as the Monte Carlo was used in the control regions. This effect was estimated by varying each different source of systematic uncertainty up or down by 1σ for each Monte Carlo contribution simultaneously, then the resulting percentage shifts for each systematic uncertainty were added in quadrature.

The methods themselves are subject to systematic uncertainties based on the underlying assumptions, which were estimated using the procedures discussed below. Finally both methods have statistical uncertainties, which are included in the summaries per channel along with the other systematic uncertainties in tables 6.13 and 6.14 for the Same Sign and Non-Isolated methods respectively.

6.1.2.1 QCD Estimation Same Sign Method

The main assumption underlying this background estimation method is that for multijet events there should be no bias towards events with a light lepton and a τ lepton of opposite or the same sign electric charge. In order to test this, a control sample was defined, all overlap removed τ candidates which failed "tight" τ identification were used, and the R_{OSSS} was plotted against the isolation variables: E_TCone30/p_T for the electron channel and E_TCone40/p_T for the muon channel. This test of the stability of R_{OSSS} is shown in figure 6.6. The bands represent the statistical uncertainty, and with the exception of the lowest isolation bin in the electron channel, which suffers from low statistics, the values lie within the statistical uncertainty on the measured ratio. A conservative systematic was assigned as the maximum variation from the measured value added in quadrature to the statistical uncertainty on the central value, which is 12.4% in the electron channel and 5.2% in the muon channel. To confirm that there was no correlation with the τ identification, the control region of inverted isolation was used to plot the measured R_{OSSS} against each level of τ identification cut, "loose", "medium" and "tight", this is shown in figure 6.6. The inverted isolation for the electron channel was $p_T\text{Cone}/40p_T \geq 0.06$ and $E_T\text{Cone}30/p_T \geq 0.1$; for the muon channel the inverted isolation was $p_T\text{Cone}40/p_T \geq 0.06$ and $E_T\text{Cone}40/p_T \geq 0.06$. As no significant correlation is evident, and only the "tight" level of τ identification was used in the estimation, no additional systematic was assigned.

6.1.2.2 QCD Estimation Non-Isolated Method

The main assumption in this method is that the lepton isolation and the τ identification are uncorrelated. To test this assumption, different values of the lepton isolation and different levels of the τ identification were chosen and the background estimate repeated. First the isolation variables were loosened, for electrons to $p_T\text{Cone}40/p_T \geq 0.1$ and $E_T\text{Cone}30\ /p_T \geq 0.2$; for muons to $p_T\text{Cone}40/p_T \geq 0.1$ and $E_T\text{Cone}40/p_T \geq 0.1$. In table 6.9 where the variations are summarised, this shift is labelled Isolation 1. The difference in the estimate was 0.6% (1.8%) for the

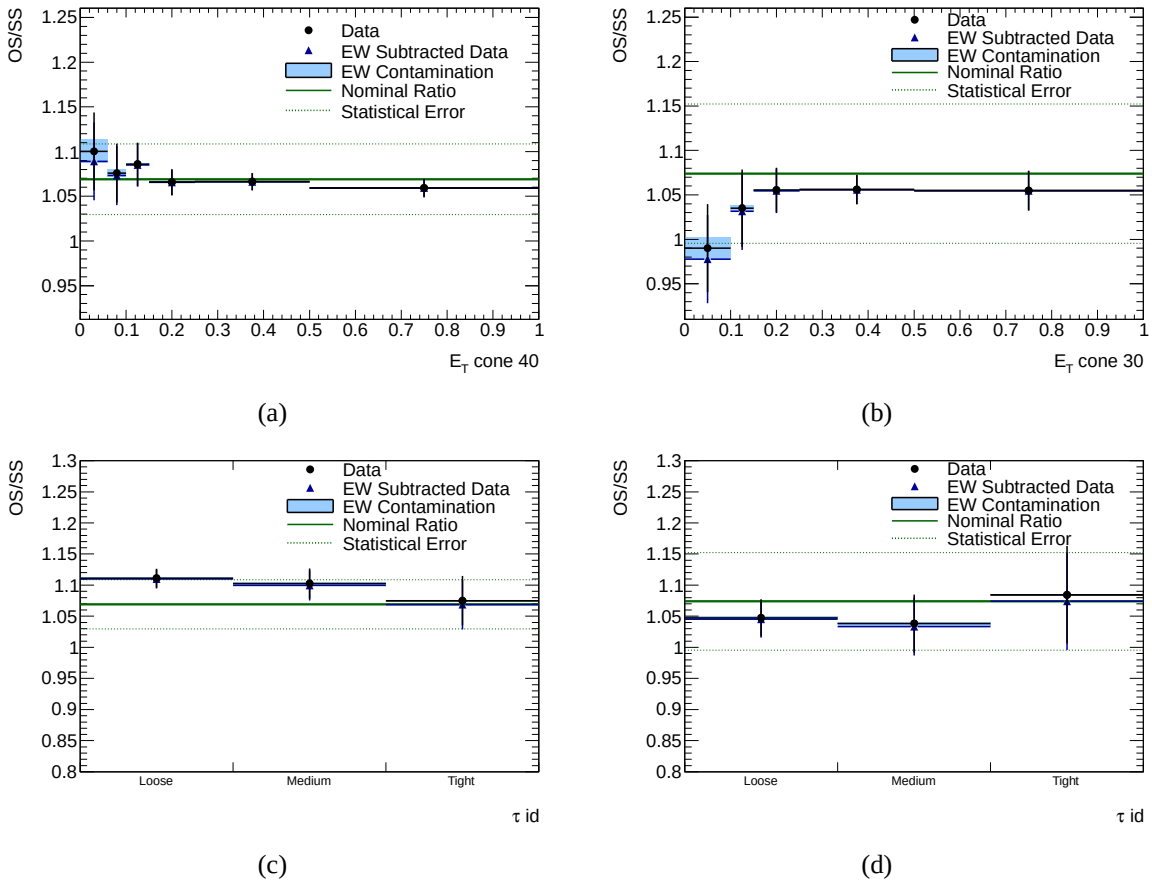

Figure 6.6: Stability of R_{OSSS} as a function of calorimeter isolation (τ identification) on top (bottom) for muons (electrons) on left (right) in data. The solid line represents the measured ratio and the dashed lines give the statistical error. The estimated impurity from the electroweak backgrounds is shown as a shaded box on each bin.

muon (electron) channel. Second the isolation variables were tightened, $p_T\text{Cone40}/p_T \geq 0.1$ and $E_T\text{Cone30}/p_T \geq 0.05$ for electrons; $p_T\text{Cone40}/p_T \geq 0.03$ and $E_T\text{Cone40}/p_T \geq 0.04$ for muons. This shift is labelled as Isolation 2. The difference for this variation was 1.1% (0.8%) for the muon (electron) channel. Third the τ identification was changed to select "loose", but not "medium", instead of the default "loose" but not "tight" τ candidates. This led to a much more significant difference of 8.8% (3.5%) for muon (electron) channel.

As an additional cross-check, the shapes of the isolation variables for different levels of the τ identification were compared to ensure no dependence was present. The sum of the two regions containing "tight" τ candidates (A+B) was compared to the sum of the two regions containing "loose" but not "tight" τ candidates. These comparisons can be seen in figure 6.7.

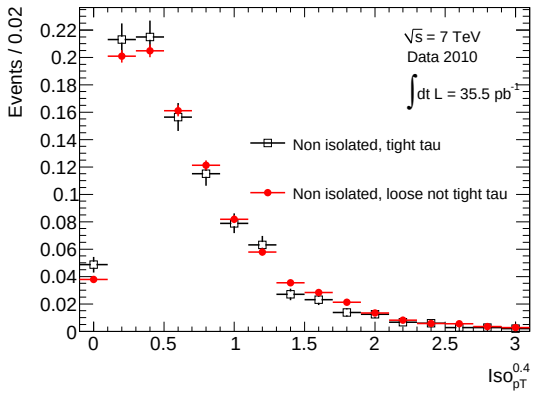

(a) Muon isolation p_TCone40 divided by p_T.

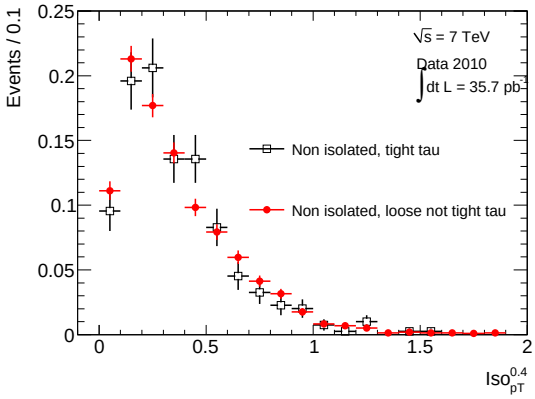

(b) Electron isolation p_TCone40 divided by p_T.

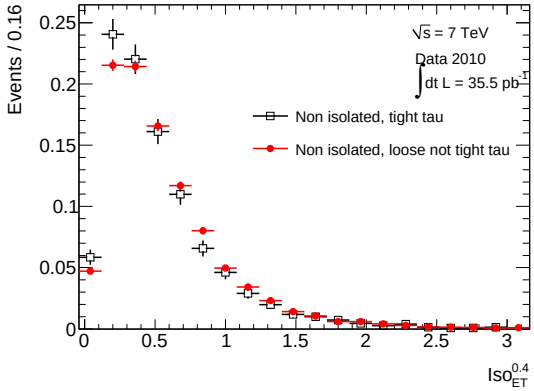

(c) Muon isolation E_TCone40 divided by p_T.

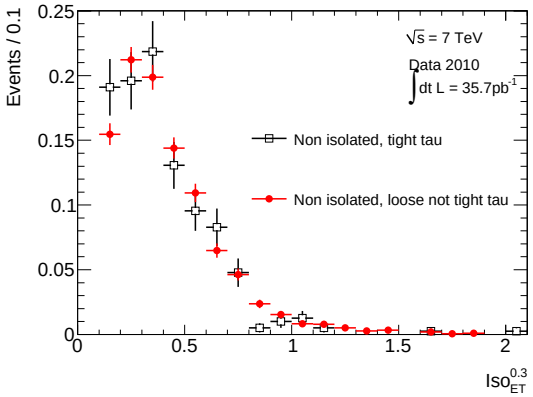

(d) Electron isolation E_TCone30 divided by p_T.

Figure 6.7: Comparison of the shape of the isolation distributions for the A+B and C+D regions.

The shapes were found to be in agreement within the statistical uncertainties and no systematic was assigned on this check.

Variation	Muon channel	Electron channel
Default	22.6 ± 2.7	25.4 ± 3.1
Isolation 1	22.7 ± 2.8	25.0 ± 3.1
Isolation 2	22.4 ± 2.7	25.6 ± 3.1
τ candidate “loose” not “medium”	20.6 ± 3.1	26.3 ± 3.6
Systematic uncertainty from Isolation	± 0.3	± 0.5
Systematic uncertainty from τ identification	± 2.0	± 0.9

Table 6.9: Summary of the background estimates after each variation described in 6.1.2.2 and the estimated systematic uncertainty for each.

To obtain a value for the total systematic on the background estimation, the aforementioned systematic uncertainties based on the correlations in the method were added in quadrature with those due to the systematic uncertainties on the contamination corrections in the control regions,

and with the statistical uncertainties arising due to the limited Monte Carlo available to estimate these corrections.

6.1.3 A_Z Calculation Systematic Uncertainty

The dominant theoretical uncertainties affecting this measurement arise from limited knowledge of the parton distribution functions and the modelling of the Z boson at the LHC. They can be divided into three components.

- **Uncertainty within one PDF set**

  The CTEQ6.6 NLO PDF set was used to estimate this uncertainty, it has 22 error eigenvalues available [103], for each error eigenvalue i, the sample was reweighted to the error eigenvalue, then the acceptances, A_Z^{i+} and A_Z^{i-}, were recalculated using the following relation:

$$\Delta A_Z = \frac{1}{2}\sqrt{\Sigma_i \left(A_Z^{i+} - A_Z^{i-}\right)^2} \tag{6.1}$$

- **Deviations between different PDF sets**

  The acceptance values from the default PDF were compared to those obtained when the sample was reweighted to the HERAPDF1.0 [104] and CTEQ6.6 PDF sets. The resulting deviation gave the systematic uncertainty.

- **Uncertainty due to the modelling of the parton shower**

  A sample was generated using MC@NLO and Herwig parton shower combined, with the CTEQ6.6 PDF, MC10 tune and a minimum invariant mass of 60 GeV, and used to recalcuate the A_Z factor. The variation from the default value was taken as the uncertainty. Since the Herwig generator did not handle the τ polarisation accurately during τ lepton decays when interfaced with the MC@NLO generator at the time, a correction was applied to account for the difference in acceptance calculated from the MC@NLO sample. The correction was determined from dedicated samples produced with and without

τ polarisation switched on. The correction factors were measured to be 0.9917 $\pm$ 0.0002 for the muon channel and 0.9904 $\pm$ 0.0002 for the electron channel, where the errors are statistical.

	Muon channel	Electron channel
PYTHIA MRSTLO*	0.1169	0.1007
PYTHIA CTEQ6.6	0.1191	0.1026
PYTHIA HERAPDF1.0	0.1185	0.1020
PYTHIA CTEQ6.6 $m_{Z/\gamma^*} > 60$ GeV	0.1185	0.1022
MC@NLO CTEQ6.6 $m_{Z/\gamma^*} > 60$ GeV	0.1174	0.1016
MC@NLO CTEQ6.6 $m_{Z/\gamma^*} > 60$ GeV (with spin effect correction)	0.1165	0.1006

Table 6.10: Values of the A_Z geometric and kinematic acceptance factor calculated using the default PDF (PYTHIA MRSTLO*) and other variations.

	Muon channel	Electron channel
CTEQ 6.6 Eigenvector Set	1.2%	1.2%
Different PDF Sets	1.9%	1.9%
Model Dependence	1.8%	1.6%
Total Uncertainty	2.9%	2.8%

Table 6.11: Relative uncertainties on the A_Z factors, calculated as described in the text.

A summary of these systematic assessments concerning use of different PDFs and models is given in tables 6.10 and 6.10. Additional sources of uncertainty on the A_Z measurement were considered, these were the modelling of the τ decays with TAUOLA [84] and of the QED radiation with PHOTOS [85]. The τ lepton p_T spectrum depends on the branching ratios of the hadronic decay modes and thus the fraction of energy they receive, in order to quantify the effect of changing this fraction, a secondary sample was generated using SHERPA [105] which contains its own library of τ decay branching ratios. The PHOTOS Monte Carlo is known to be accurate to better than 0.2%, which is negligible compared to the uncertainties due to the PDFs. The uncertainties from all sources were added in quadrature to obtain the total uncertainty on A_Z of 3% in both channels.

6.1.4 C_Z Calculation Systematic Uncertainty

As the C_Z value contains efficiencies for the detector, reconstruction and identification, the uncertainties were those applicable to the signal simulation described in section 6.1.1. Each uncertainty is listed in table 6.12, these were added in quadrature to obtain the total uncertainty. The dominant systematic uncertainties were the τ identification and energy scale. In the electron channel another significant uncertainty arose due to the large uncertainties on the correction factors for the electron identification at low values of p_T, between 16 and 20 GeV, where ∼35% of signal lies.

Systematic Uncertainty	$\delta C_Z/C_Z$ Muon channel	$\delta C_Z/C_Z$ Electron channel
Lepton Efficiency	3.6%	9.2%
Lepton Resolution (μ Energy Scale)	0.2%	0.2%
Problematic Regions in the Calorimeter	–	0.4%
e Charge Misidentification	–	0.21%
τ Id Efficiency	8.6%	8.6%
Energy Scale Lepton and τ	8.6%	9.4%
Pile-up Reweighting	0.4%	0.4%
Jet Cleaning	1.8%	1.8%
Total Systematic Uncertainty	12.8%	15.8%
Statistical Uncertainty	1.2%	1.4%
Total Uncertainty	12.8%	15.9%

Table 6.12: Relative percentage systematic uncertainties for the C_Z factor.

6.1.5 Systematics Summary

A summary of each of the systematic uncertainties is given in the following three tables: table 6.13 lists the systematic uncertainties on each of the backgrounds including the multijets estimated using the Same Sign method; table 6.14 lists the uncertainties using the Non-Isolated method of multijet background estimation and table 6.15 gives the uncertainties on the Monte Carlo prediction of expected signal.

Systematic Uncertainty	Muon channel (% Deviation)				Electron channel (% Deviation)			
	$(N_{obs} - N_{bkg})$	Multijet	$W+$ jets	$\gamma^\star/Z + t\bar{t}$	$(N_{obs} - N_{bkg})$	Multijet	$W+$ jets	$\gamma^\star/Z + t\bar{t}$
Lepton Efficiency	0.24	1.6	3	2.8 $(\gamma^\star/Z)$ 5.9 $(t\bar{t})$	0.31	2.7	7	5.0 $(\gamma^\star/Z)$ 9.0 $(t\bar{t})$
Lepton Resolution(μ Energy Scale)	0.018	0.092	0.2	0.2	0.012	0.065	0.2	0.2
Problematic Calorimeter Regions	0.0023	0.016	0	0	0.022	0.14	0.4	0.4
e Charge Misidentification	0.0023	0.016	0	0	0.014	0.064	0.21	0.21
τ Id Efficiency	0.078	0.54	0	0	0.11	0.55	0	0
Energy Scale Lepton and τ	1.7	10	19	24.3 $(\gamma^\star/Z)$ 18.0 $(t\bar{t})$	1.3	8.8	21	29.1 $(\gamma^\star/Z)$ 13.1 $(t\bar{t})$
Lepton-jet τ Fake Rate	1.1	5	0	24	0.66	3.9	0	20 $(\gamma^\star/Z)$ 24 $(t\bar{t})$
Pile-up Reweighting	0.029	0.17	0.35	0.35	0.02	0.12	0.35	0.35
Jet Cleaning	0.067	0.41	0	1.8	0.066	0.51	0	2.5
k_W Factor	0.12	3.6	8.2	0	0.18	2.2	11	0
OSSSRatio	0.76	5.2	0	0	2	10	0	0
Theoretical Cross-section	0.2	1.4	0	5.0 $(\gamma^\star/Z)$ 8.3 $(t\bar{t})$	0.12	1.3	0	5.0 $(\gamma^\star/Z)$ 8.3 $(t\bar{t})$
Total Systematic Uncertainty	2.2	13	21	34	2.5	14	25	35
Statistical Uncertainty	9.8	27	8.3	3	12	27	9.9	3.8
Total Uncertainty	10	30	22	34	12	30	27	35

Table 6.13: Summary of the systematic and statistical uncertainties for each of the main backgrounds and for the predicted signal for both the muon and electron channels using the Same Sign method of multijet background estimation, described in section 5.6.2. The "lepton efficiency" entry includes the lepton trigger, reconstruction, identification and isolation uncertainties added in quadrature.

	Muon channel (% Deviation)				Electron channel (% Deviation)			
Systematic Uncertainty	$(N_{obs} - N_{bkg})$	Multijet	$W+$ jets	$\gamma^\star/Z + t\bar{t}$	$(N_{obs} - N_{bkg})$	Multijet	$W+$ jets	$\gamma^\star/Z + t\bar{t}$
Lepton Efficiency	0.08	3.20	3.0	2.8 $(\gamma^\star/Z)$ 5.9 $(t\bar{t})$	0.54	4.81	7.0	5.0 $(\gamma^\star/Z)$ 9.0 $(t\bar{t})$
Lepton Resolution(μ Energy Scale)	0.004	0.19	0.2	0.2	0.31	0.13	0.2	0.02
Problematic Calorimeter Regions	0	0	0	0	0.32	0.25	0.4	0.4
e Charge Misidentification	0	0	0	0	0.31	0.14	0.21	0.21
τ Id Efficiency	0.61	4.49	0	0	0.89	2.51	0	0
Energy Scale Lepton and τ	1.41	13.1	18.8	24.3 $(\gamma^\star/Z)$ 18.0 $(t\bar{t})$	0.46	10.6	21.4	29.1 $(\gamma^\star/Z)$ 13.1 $(t\bar{t})$
Lepton-jet τ Fake Rate	1.51	1.88	0	24	0.52	2.81	0	20 $(\gamma^\star/Z)$ 24 $(t\bar{t})$
Pileup Reweighting	0.007	0.33	0.35	0.35	0.32	0.22	0.35	0.35
Jet Cleaning	0.03	1.15	0	1.3 $(\gamma^\star/Z)$ 5.0 $(t\bar{t})$	0.32	0.79	0	2.0 $(\gamma^\star/Z)$ 5.0 $(t\bar{t})$
k_W Factor	0.46	1.32	8.20	0	0.15	0.82	11.1	0
Multijet Estimate Method	2.22	8.84	0	0	3.02	4.05	0	0
Theoretical Cross-section	0.05	3.22	0	5.0 $(\gamma^\star/Z)$ 8.3 $(t\bar{t})$	0.40	2.08	0	5.0 $(\gamma^\star/Z)$ 8.3 $(t\bar{t})$
Total Systematic Uncertainty	3.12	17	21	34	3.4	13.1	25	35
Statistical Uncertainty	9.02	12	8.3	3	11.5	12.1	9.9	3.8
Total Uncertainty	9.54	21	22	34	12.0	17.8	27	35

Table 6.14: Summary of the systematic and statistical uncertainties for each of the main backgrounds and for the predicted signal for both the muon and electron channels using the Non-Isolated method of multijet background estimation, described in section 5.6.3. The "lepton efficiency" entry includes the lepton trigger, reconstruction, identification and isolation uncertainties added in quadrature.

Systematic Uncertainty	Muon channel (% Deviation)	Electron channel (% Deviation)
Lepton Efficiency	3.6	9.2
Lepton Resolution (μ Energy Scale)	0.2	0.2
Problematic Regions in the Calorimeter	0	0.4
e Charge Misidentification	0	0.21
τ Id Efficiency	8.6	8.6
Energy Scale Lepton and τ	8.6	9.4
Lepton-jet τ Fake Rate	0	0
Pileup Reweighting	0.4	0.4
Jet Cleaning	1.8	1.8
k_W Factor	0	0
Theoretical Cross-section	5.0	5.0
Total Systematic Uncertainty	13.8	16.6

Table 6.15: The estimated systematic uncertainties of the Monte Carlo predicted signal yield. The "lepton efficiency" entry includes the lepton trigger, reconstruction, identification and isolation uncertainties added in quadrature.

6.2 Cross-section Measurement

6.2.1 Measured Fiducial Cross-section

The fiducial cross-section was calculated, as defined in 5.19, to be

$$\sigma^{fid}(Z \to \tau\tau) \times BR(\tau \to \mu\,\nu\,\nu,\ \tau \to\ had\,\nu) = \\ 22.55 \pm 2.14\text{(stat.)} \pm 3.42\text{(syst.)} \pm 0.79\text{(lumi.) pb} \tag{6.2}$$

for the muon channel and

$$\sigma^{fid}(Z \to \tau\tau) \times BR(\tau \to e\,\nu\,\nu,\ \tau \to\ had\,\nu) = \\ 26.59 \pm 3.16\text{(stat.)} \pm 4.74\text{(syst.)} \pm 0.94\text{(lumi.) pb} \tag{6.3}$$

for the electron channel, where the individual components of the calculation are summarised in table 6.16.

	Muon channel	Electron channel
N_{obs}	213 ± 15	151 ± 12
$N_{obs} - N_{bkg}$	$164 \pm 16 \pm 4$	$114 \pm 14 \pm 3$
A_Z	$0.11691 \pm 0.00023 \pm 0.00351$	$0.10073 \pm 0.00021 \pm 0.00302$
C_Z	$0.2045 \pm 0.0024 \pm 0.0262$	$0.1197 \pm 0.0017 \pm 0.0189$
$\mathcal{L}$	35.51 ± 1.21	35.75 ± 1.22

Table 6.16: The components of the $Z \to \tau\tau$ cross-section calculation. The first error is statistical and the second systematic. For the multijet background estimation, the same-sign sample method described in section 5.6.2 was used.

6.2.2 Measured Total Cross-section

The total cross-section, as defined in 5.16, was found to be

$$\sigma(Z \to \tau\tau) \times BR(\tau \to \mu\,\nu\,\nu, \tau \to \tau_{had}\,\nu) = \\ 192.9 \pm 18.3\text{(stat.)} \pm 29.8\text{(syst.)} \pm 6.8\text{(lumi.) pb} \tag{6.4}$$

for the muon channel and

$$\sigma(Z \to \tau\tau) \times BR(\tau \to e\,\nu\,\nu, \tau \to \tau_{had}\,\nu) = \\ 264.1 \pm 31.3\text{(stat.)} \pm 47.7\text{(syst.)} \pm 9.3\text{(lumi.) pb} \tag{6.5}$$

for the electron channel, where each term in the calculation is listed in table 6.16.

After correction of the total cross-section for the $(\tau \to l\,\nu\,\nu, \tau \to \tau_{had})$ branching ratio, 0.22495 ± 0.00074 for the muon channel and 0.23130 ± 0.00074 for the electron channel [1], the following value for the inclusive cross-section was obtained:

$$\sigma(Z \to \tau\tau, m_{inv}\ 66 - 116\ \text{GeV}) = \\ 857.6 \pm 81.4\text{(stat.)} \pm 132.5\text{(syst.)} \pm 30.19\text{(lumi.)} \pm 2.8\text{(theo.) pb} \tag{6.6}$$

for the muon channel and

$$\sigma(Z \to \tau\tau, m_{inv}\ 66 - 116\ \text{GeV}) = \\ 1142 \pm 135.5(\text{stat.}) \pm 206.2(\text{syst.}) \pm 40.19(\text{lumi.}) \pm 3.6(\text{theo.})\ \text{pb} \tag{6.7}$$

for the electron channel.

6.2.3 Comparison to $Z \to ee, \mu\mu$ Channels and Theoretical Calculations

The obtained total cross-sections agree within uncertainties with the theoretical expectation of 960 ± 49.5 pb [106]. They are also, within uncertainties, in agreement with the combined cross-section of $Z \to \ell\ell$ measured by ATLAS in the $Z \to \mu\mu$ and $Z \to ee$ channels, 945 $\pm$ 6(stat.) $\pm$ 11(syst.) $\pm$ 32(lumi.) $\pm$ 38(acc.) pb [100]. Finally they are also compatible with the combined measurement of the $Z \to \tau\tau$ cross-section in 4 channels, published recently by the CMS collaboration, 1.00 $\pm$ 0.05(stat.) $\pm$ 0.08(syst) $\pm$ 0.04(lumi.) nb [107]. The comparison of the present study's results with those quoted above can be see in figure 6.8.

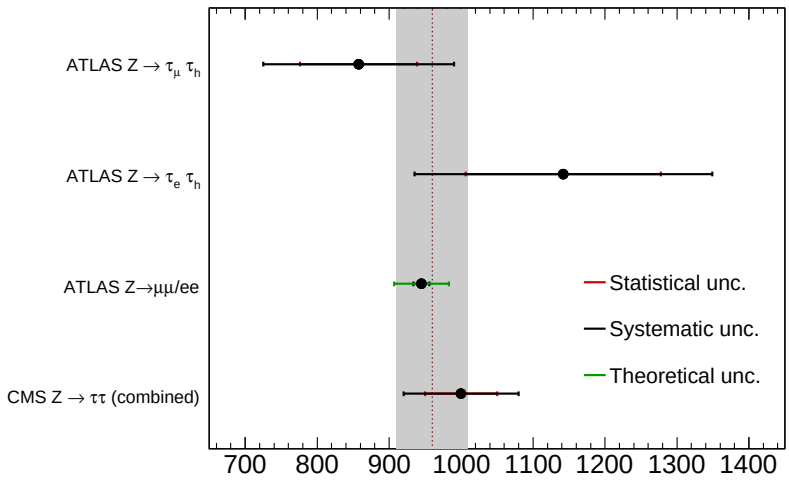

Figure 6.8: Comparison of the measured cross-sections to theory, the combined cross-section $Z \to \ell\ell$ measured by ATLAS in the $Z \to \mu\mu$ and $Z \to ee$ channels and to the combined measurement of the $Z \to \tau\tau$ cross-section in 4 channels, published recently by the CMS collaboration.

6.2.4 Event Display

To illustrate the ATLAS detector identification of a $Z \rightarrow \tau_\ell \tau_h$ event, a candidate event is demonstrated in the ATLAS event display format in figure 6.9. The particular event shown here was collected at centre-of-mass energy 7 TeV and was recorded on the 3^{rd} August 2010. One τ lepton decayed muonically and the other hadronically with 3 charged tracks. The muon and hadronically reconstructed τ lepton have opposite electrical charge and the event contains no further reconstructed electrons, muons or jets. The muon has p_T = 18 GeV, the τ lepton has visible p_T = 26 GeV. The reconstructed visible mass is m_{vis} = 47 GeV, the transverse mass m_T = 8 GeV and the E_T^{miss} = 7 GeV.

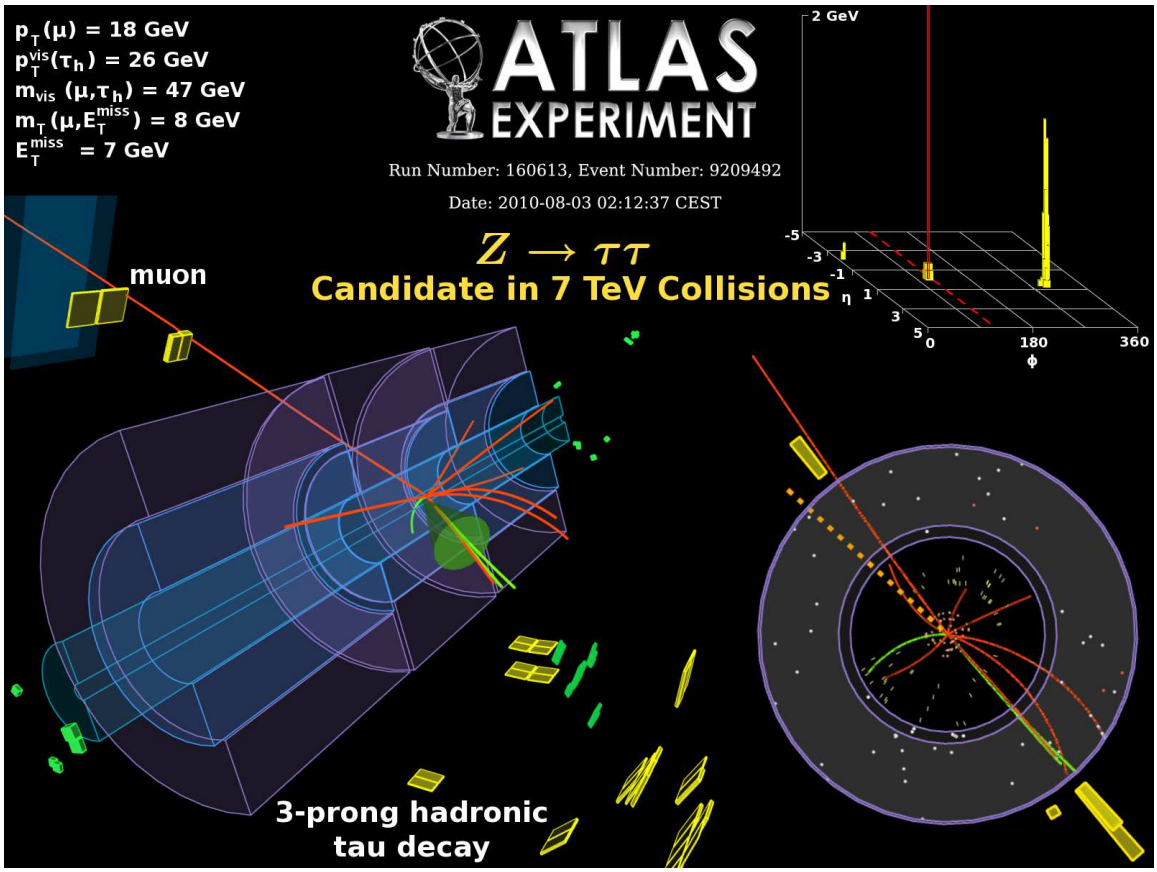

Figure 6.9: A $Z \rightarrow \tau_\mu \tau_h$ candidate event collected at $\sqrt{s}$ = 7 TeV on August 3^{rd} 2010. One τ lepton decays muonically and the other hadronically with 3 charged tracks.

Chapter 7

Vector Boson Fusion $H \rightarrow \tau_\ell \tau_h$

7.1 Cuts Based Analysis

In the low range of possible Higgs boson masses, $M_H < 130$ GeV, one of the most important search channels for the Standard Model Higgs boson is the Vector Boson Fusion (VBF) production of Higgs to two τ leptons. As discussed in section 2.3.2 the two forward jets from VBF production are a useful discriminator against background. The main backgrounds to this signal are from QCD multijets, W + jets and Z + jets, where the Z decays to pair of electrons, muons or τ leptons. The prospects for this channel were fully evaluated by an analysis which was designed and optimised for $\sqrt{s} = 14$ TeV [108].

ATLAS has a procedure known as an "acceptance challenge" which each member of an analysis group is required to complete to ensure uniformity in the application of the cuts and corrections, which was completed successfully and is documented here. It was performed for the VBF Higgs $\rightarrow \tau\tau$ analysis; at the time it was believed that the centre of mass energy of the LHC during Autumn 2010 would be $\sqrt{s} = 10$ TeV. Therefore the analysis discussed here was designed using Monte Carlo simulation produced using the HERWIG generator [83] at $\sqrt{s}$ =10 TeV.

7.1.1 Object Selection

7.1.1.1 Electrons

Electrons were selected if they had $p_T > 10$ GeV and passed the "medium" identification level with no isolation criteria included; instead an isolation requirement that less than 10% of the

E_T of each electron fell within an isolation cone of $\Delta R = 0.2$ around the electron was applied.

7.1.1.2 Muons

Muons were required to have $p_T > 8$ GeV, those selected were reconstructed using the combined method where a muon spectrometer standalone track was extrapolated to the interaction point and matched to an inner detector track and quality requirements were placed on the matching. The muon was required to be the best matched candidate in the case where multiple inner detector tracks were present, and to have $\chi^2 < 100$ on the matching and $\chi^2 < 500$ on the fitting. Requirements were made on the isolation of the muon, less than 10% of the E_T of the muon was expected to fall in an isolation cone of $\Delta R < 0.2$.

7.1.1.3 τ leptons

The hadronically decaying τ leptons were required to have $p_T > 20$ GeV, 1 or 3 tracks, integer charge, of value ± 1, and to pass the cuts-based identification level of "medium" [109] as well as the dedicated electron veto, described in section 3.3.4.3.

7.1.1.4 Jets

The jets were reconstructed from topoclusters [59] using a cone algorithm [58] with a radius of $\Delta R = 0.4$, they were required to have $p_T > 20$ GeV and $|\eta| < 4.8$.

7.1.1.5 Overlap Removal

Muons, electrons, τ leptons and jets can all be reconstructed using the same energy deposits since the algorithms are not exclusive. The most accurate object reconstruction and identification belongs to the muons, then the electrons, then the τ leptons and finally the jets, thus a hierarchy is created; objects which overlapped within a cone of $\Delta R = 0.2$ were removed in order of reliability. For example if an electron overlapped with a muon, the electron was removed.

7.1.2 Event Selection

Each of the event level cuts was studied in the course of the 14 TeV analysis [108], for this analysis proposal the same criteria were used, however the p_T thresholds were lowered to reflect the reduction in the centre of mass energy.

7.1.2.1 Trigger Requirement

The event selection required that a single lepton trigger was passed: in the electron channel the trigger was EF_e12_medium; for the muon channel the trigger was EF_mu10. Since the p_T of a lepton resulting from a τ lepton decay is low compared with that of leptons from direct decays of bosons, the ideal trigger threshold is low, approximately 10 GeV, however this is optimistic because the rates increase with decreasing p_T.

7.1.2.2 Lepton Requirements

If the electron trigger was passed, then the electrons in the event were required to have $p_T > 15$ GeV and similarly if the muon trigger was passed, then the muons were required to have $p_T > 15$ GeV. This ensured that the lepton which passed the trigger had a p_T high enough to not be affected by the lower efficiencies incurred on the turn-on curve for the trigger at values of p_T close to the trigger threshold.

In order to reject the background from $Z \to \ell\ell$ it was necessary to reject events which had two or more reconstructed and identified leptons of any flavour.

The τ lepton was required to pass "tight" level identification [109] and to have opposite charge to the selected lepton.

7.1.2.3 Missing Transverse Energy

When the τ leptons decay they produce neutrinos alongside the visible decay products, which are either a light lepton (an electron or muon) or charged and neutral mesons. These neutrinos

are undetected and form the missing transverse energy of the event. By requiring $E_T^{\text{miss}} > 20$ GeV it was possible to discriminate against events where no neutrinos were present such as $Z \to \ell\ell$.

7.1.2.4 Transverse Mass

The quantity of transverse mass was defined in section 5.5.2; for the discrimination it affords against W + jets events a cut of $M_T < 30$ GeV was applied.

7.1.2.5 Collinear Approximation

Since the τ leptons are typically highly boosted when they decay, the decay products tend to be collimated; by assuming that the neutrinos are collinear to the visible decay products it becomes possible to reconstruct the invariant mass of a pair of τ leptons, $M_{\tau\tau}$.

The unknown quantity in the system is the proportion of the τ lepton's energy which is carried away by the neutrinos. For the hadronically decaying τ lepton this fraction is denoted x_h and for the leptonically decaying τ lepton, x_l. Using the x and y components of the measured E_T^{miss}, and using the assumption that the sum of the neutrinos' energy is the E_T^{miss} it is possible to calculate x_h and x_l as long as the two τ leptons are not produced back to back. To avoid events where this is the case a restriction was placed on the azimuthal angular distribution of the two τ leptons: $|\Delta\phi_{\tau\tau}| < 0.9$. In order to avoid unphysical solutions due to the mis-measurement of E_T^{miss} the fractions of τ momentum were restricted to $0 \leqslant x_{h,l} \leqslant 1$. The invariant mass is given by:

$$M_{\tau\tau} = \frac{M_{l,h}}{\sqrt{x_l x_h}} = \sqrt{2(E_h + E_{\nu h})(E_l + E_{\nu l})(1 - \cos\theta_{lh})} \tag{7.1}$$

where $M_{l,h}$ is the invariant mass of the visible decay products from the lepton and hadron and E_h represents the energy of the visible decay products of the hadronic decay, similarly E_l the energy of the visible lepton, $E_{\nu h}$ is the energy of the neutrino from the hadronic τ lepton decay and $E_{\nu l}$ is the sum of the energies of the neutrinos from the leptonic τ decay. θ_{lh} is the angle between the visible lepton and the reconstructed τ lepton.

A window cut was placed on this mass variable centred on the expected Higgs boson mass for this sample, $M_H = 120$ GeV, of 105 GeV $< M_{\tau\tau} <$ 135 GeV.

7.1.2.6 Vector Boson Fusion Specific Cuts

In a VBF event there are two high momenta jets, typically high in $|\eta|$ and in opposite hemispheres of the detector. Due to colour coherence between them there is suppressed QCD radiation in the central region. This is shown in figure 7.1 where the η of the first and second highest momentum jets is shown compared to two important backgrounds, $Z \rightarrow \mu\mu$ + jets and $t\bar{t} \rightarrow \mu\mu$ + jets, these plots are produced using 14 TeV Monte Carlo [108]. Identifying these two jets provides a good indicator of a VBF signal. This was done by requiring at least two jets, with the leading jet (highest-p_T) to have $p_T > 20$ GeV; then that the two highest-p_T jets be in opposite hemispheres, by $\eta_{j_1} \times \eta_{j_2} < 0$, with a separation of $(\Delta\eta)_{j_{1,2}} > 3.6$. To ensure that the correct two jets were selected a di-jet mass cut was imposed of $M_{jj} > 500$ GeV as this reflects that the jets are high in energy and well separated. The distribution of the difference in pseudorapidity between the two jets and their invariant mass is shown in figure 7.2 compared to two main backgrounds, all produced at $\sqrt{s} = 14$ TeV [108]. Since the Higgs decay was expected in the central region, two requirements were used, that the τ lepton, and the lepton, should lie between the jets: $\min(\eta_{j_1}, \eta_{j_2}) < \eta_\tau$ and $\eta_l < \max(\eta_{j_1}, \eta_{j_2})$. As no additional QCD activity is expected in this central region a central jet veto was employed; if any other jet in the event had $|\eta| < 3.2$ the event was discarded.

7.1.3 Results

7.1.3.1 10 TeV Validation Analysis

The result of the application of each cut is shown in table 7.1. This illustrates which were the tightest cuts and the overall level of efficiency of the signal selection which can be expected using such a complex set of event level cuts.

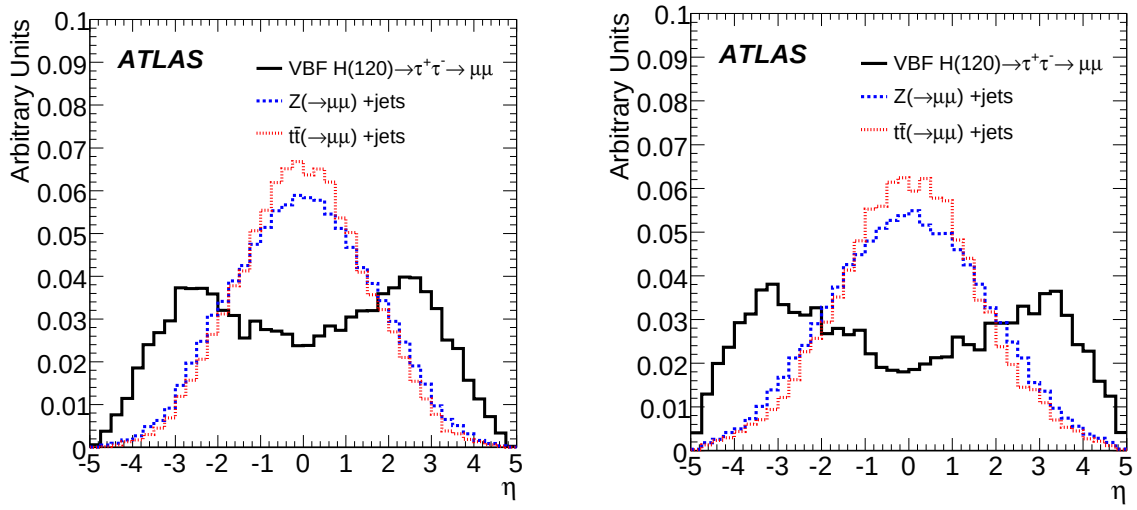

(a) (b)

Figure 7.1: η of the highest p_T (a) and second highest p_T (b) jets for VBF $H \to \tau\tau \to \mu\mu$ at a Higgs mass of 120 GeV, $t\bar{t} \to WW \to \mu\mu$ and $Z \to \mu\mu$ + n jets. Only p_T cuts were applied to jets. Monte Carlo produced at $\sqrt{s}$ =14 TeV [108].

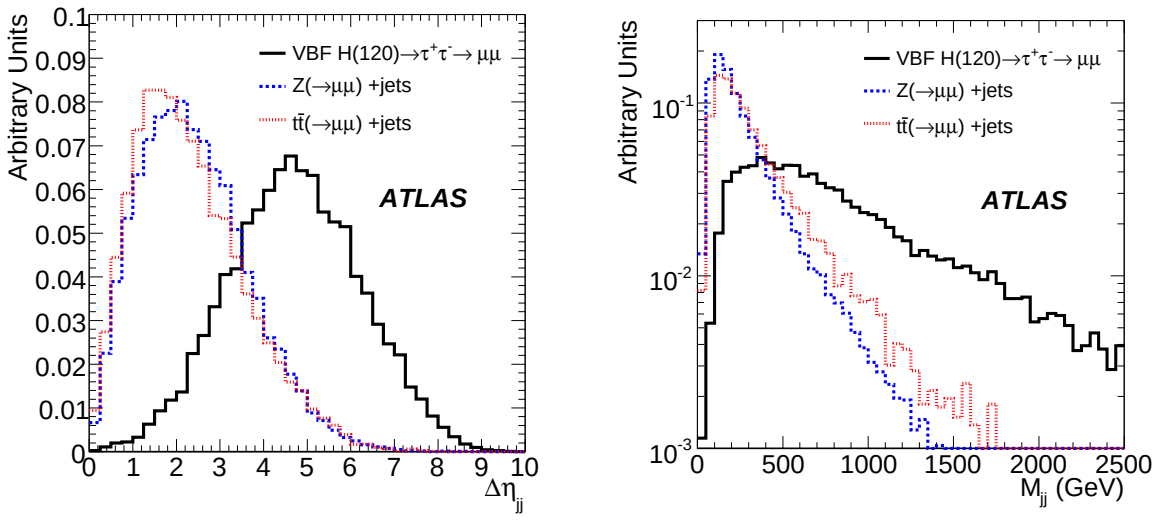

(a) (b)

Figure 7.2: $\Delta\eta$ between VBF jets (a) and invariant-mass distributions of VBF jets (b) in VBF $H \to \tau\tau \to \mu\mu$ events at a Higgs mass of 120 GeV, $t\bar{t} \to WW \to \mu\mu$ and $Z \to \mu\mu$ + n jets. A requirement $\eta_1 \times \eta_2 \geqslant 0$ is used in addition to the cuts on jet p_T. Monte Carlo produced at $\sqrt{s}$ =14 TeV [108].

As is shown in table 7.1 only ∼1% of signal events passed such stringent selection requirements. This analysis could potentially benefit from a more elaborate analysis technique which could preserve these signal events while still providing adequate rejection against the main

Cut	Total	Electron channel		Muon channel	
		Number	[%]	Number	[%]
Start	49954	49954	100.0	49954	100.0
Trigger Passed	32191	14701	29.4	15802	31.6
Di-lepton Veto	22197	10630	21.3	11567	23.2
Tight τ	5781	2766	5.5	3015	6.0
Missing Transverse Energy	4539	2180	4.4	2359	4.7
Transverse Mass	3394	1667	3.3	1727	3.5
Collinear Approximation	1970	968	1.9	1002	2.0
Tight Jet Requirement	1557	770	1.5	787	1.6
Forward Jet Requirement	1258	629	1.3	629	1.3
Centrality Requirement	1115	570	1.1	545	1.1
Jet Separation	889	447	0.9	442	0.9
Di-jet Mass	711	357	0.7	354	0.7
Central Jet Veto	621	319	0.6	302	0.6
Mass Window	499	258	0.5	241	0.5

Table 7.1: Number of events passing each cut in the VBF $H \to \tau_\ell \tau_h$ ($M_H = 120$ GeV) simulated signal sample.

backgrounds and the remainder of this chapter discusses this possibility by means of a Matrix Element analysis.

7.1.3.2 14 TeV Full Analysis

Since the validation analysis concerns only the signal selection, to give an indication of the sensitivity of the analysis and the power of the cuts with respect to background a summary of the results from the full analysis at 14 TeV is included here. A summary of the cuts and their values is given below and in table 7.2 the cross-sections for the signal and the evaluated backgrounds are included at each stage in the cut flow, the background estimations techniques used to obtain these predictions are described fully in the main publication [108].

- Trigger: Electron trigger 22 GeV threshold with isolation or muon trigger 20 GeV threshold
- Trigger lepton: At least one lepton with p_T greater or equal to the corresponding trigger threshold
- Di-lepton Veto: Exactly one identified lepton
- τ Candidate: Exactly one identified τ lepton with opposite charge to the lepton

	VBF $H \to \tau\tau$	$Z \to \tau\tau$ + jets ($\geqslant 1$)		$t\bar{t}$	$Z \to \ell\ell$ + jets	$W \to \ell\nu$ + jets	diboson
		QCD	EWK		($\geqslant 1$)	($\geqslant 1$)	$WW/WZ/ZZ$
Cross-section (fb)	309.1	168.4×10^3	1693	833×10^3	768.6×10^3	8649×10^3	174.1×10^3
Trigger	57.2(1)	$51.5(1) \times 10^3$	230(1)	$209.8(2) \times 10^3$	$633.8(4) \times 10^3$	$4411(9) \times 10^3$	$32.0(1) \times 10^3$
Trigger Lepton	49.5(1)	$42.7(1) \times 10^3$	190(1)	$179.1(2) \times 10^3$	$588.0(4) \times 10^3$	$3815(9) \times 10^3$	$28.0(1) \times 10^3$
Di-lepton Veto	43.4((1)	$38.4(1) \times 10^3$	171(1)	$156.4(2) \times 10^3$	$216.5(4) \times 10^3$	$3811(9) \times 10^3$	$23.7(1) \times 10^3$
τ Candidate	8.02(7)	3062(42)	19.3(4)	5224(56)	20250(156)	32537(1012)	704(30)
$E_T^{\text{miss}} \geqslant 30$ GeV	4.96(5)	850(20)	12.1(3)	4251(50)	468(26)	21001(801)	474(26)
Collinear Approximation	3.34(5)	514(15)	7.8(2)	606(19)	17(3)	324(46)	32(6)
Transverse Mass	2.46(4)	415(13)	6.5(2)	176(10)	11(2)	67(18)	14(3)
Jet Multiplicity	2.02(4)	235(7)	6.0(2)	162(9)	8(1)	49(11)	7(1)
Forward Jets	1.52(3)	40(3)	2.3(1)	32(4)	1.3(6)	2.9(3)	3(1)
Jet Kinematics	0.82(2)	2.7(1)	0.72(6)	1.8(1)	0.10(1)	0.7(1)	0.06(1)
Central Jet Veto	0.72(2)	1.2(1)	0.49(5)	0.25(4)	0.047(6)	0.43(6)	0.02(1)
Mass Window	0.61(2)	0.11(2)	0.04(1)	0.012(5)	0.008(1)	0.020(6)	0.001(1)

Table 7.2: Cross-section after each cut in the VBF $H \to \tau\tau$ ($M_H = 120$ GeV) simulated signal sample and the $Z \to \tau\tau$ + jets, $t\bar{t}$, $Z \to \ell\ell$ + jets, $W \to \ell\nu$ + jets and diboson backgrounds (fb) [108]. The statistical uncertainty on the last figure due to the limited Monte Carlo statistics is given in brackets.

- $E_T^{\text{miss}} \geqslant 30$ GeV
- Collinear Approximation: $0 \leqslant x_l \leqslant 0.75$, $0 \leqslant x_h \leqslant 1$, and $(\cos\Delta\phi)_{l,h} \geqslant$ -0.9
- $m_T \leqslant 30$ GeV
- Jet Multiplicity: At least one jet with $p_T \geqslant 40$ GeV and at least one additional jet with $p_T \geqslant 20$ GeV
- Forward Jets: In opposite hemispheres $\eta_{j_1} \times \eta_{j_2} \leqslant 0$, with tau centrality $\min(\eta_{j_1}, \eta_{j_2}) < \eta_\tau$ and $\eta_l < \max(\eta_{j_1}, \eta_{j_2})$ for the two highest p_T jets
- Jet Kinematics: $\Delta\eta_{jj} \geqslant 4.4$ and di-jet mass $m_{jj} \geqslant 700$ GeV for two forward jets
- Central Jet Veto: The event is rejected if there are any additional jets with $p_T \geqslant 20$ GeV in $|\eta| \leqslant 3.2$
- Mass Window: m_H -15 GeV $\leqslant m_{\tau\tau} \leqslant m_H$ + 15 GeV around the test Higgs mass of $m_H = 120$ GeV

7.2 The Matrix Element Analysis Method

The Matrix Element method is a complex analysis technique differing from a straight-forward cuts based analysis primarily by the direct inclusion of the full Matrix Element cross-section calculation of the process. This calculation is convoluted with detector resolution functions to produce a likelihood function based on the measured quantities. This technique was originally developed at CDF and D0 to minimise statistical uncertainties [110–113]. It has since been used to make an accurate measurement of the top quark mass and to discover electroweak single top production [114–118]. There are two ways in which the matrix element can be used and benefited from; the first is to calculate an event likelihood function, which encapsulates all of the kinematic information. Instead of applying a raft of kinematic cuts which can greatly reduce the size of the event sample using a variable based on this event likelihood function allows the maximum power of the events because each event is included with a weight effectively. The

second method is to calculate a sample likelihood, this can then be fitted and simultaneously enables the user to measure theoretical parameters associated with the process or experimental parameters associated with detector resolution, for example jet energy scales [119], thereby reducing the systematic uncertainties.

The sample likelihood ($\mathscr{L}_{sample}$) is related to the event likelihood ($\mathscr{L}_{evt}$) by:

$$\mathscr{L}_{sample}(\{\vec{x}_i\};\vec{\alpha},\vec{\beta},\vec{f}) = \prod_{i=1}^{N} \mathscr{L}_{evt}(\vec{x}_i;\vec{\alpha},\vec{\beta},\vec{f}) \tag{7.2}$$

where $\vec{x}$ are the n measured particle quantities of event i, $\vec{\alpha}$ are the theoretical parameters of the process, $\vec{\beta}$ are the experimental parameters of the detector and $\vec{f}$ are the fractions that each possible process contributes to the event sample, where N is the number of events. By minimising $-\ln \mathscr{L}_{sample}$ the parameters $\vec{\alpha}$, $\vec{\beta}$ and $\vec{f}$ are determined.

The analysis method proposed here uses $\mathscr{L}_{evt}$ to build a discriminant, where $\mathscr{L}_{evt}$ is defined as:

$$\mathscr{L}_{evt}(\vec{x};\vec{\alpha},\vec{\beta},\vec{f}) = \sum_{P} f_P \mathscr{L}_P(\vec{x};\vec{\alpha},\vec{\beta}) \tag{7.3}$$

where $\mathscr{L}_{evt}$ is a sum of the likelihoods for each process which could contribute to the event, weighted by f_P, the fraction of total events that the process represents and summed over P which is the number of processes which could give rise to the event. The likelihood for a given process, P, to yield the observed event given the theoretical and experimental parameters $\vec{\alpha}$ and $\vec{\beta}$, is given by:

$$\mathscr{L}_P(\vec{x};\vec{\alpha},\vec{\beta})d^n x = \frac{d\sigma_P(\vec{x};\vec{\alpha},\vec{\beta})}{\sigma_P^{obs}(\vec{\alpha},\vec{\beta})} \tag{7.4}$$

where $d\sigma_P$ is the differential cross-section for the event measured in the detector with parameters $\vec{x}$ and this is normalised by dividing by the total observed cross-section for the events seen in the detector, σ_P^{obs}. The differential cross-section for two incoming protons, p_1 and p_2, to yield the measured event $\vec{x}$, takes into account the detector resolution functions $W(\vec{x},\vec{y};\vec{\beta})$, known as the transfer functions, which describe the detector response to the input final state particles,

given by $\vec{y}$, to be measured as $\vec{x}$; it is defined as:

$$d\sigma_P(p_1, p_2 \to \vec{x}; \vec{\alpha}, \vec{\beta}) = \int_y d\sigma_P(p_1, p_2 \to \vec{y}; \vec{\alpha}) W(\vec{x}, \vec{y}; \vec{\beta}) dy \tag{7.5}$$

where $d\sigma_P(p_1, p_2 \to \vec{y}; \vec{\alpha})$ is the differential cross-section for two incoming protons to give the final state particles $\vec{y}$. This cross-section is obtained using the formula:

$$d\sigma_P(p_1, p_2 \to \vec{y}; \vec{\alpha}) = \int_{x_1 x_2} dx_1 dx_2 \sum_{a_1 a_2} f^{a_1}_{PDF}(x_1) f^{a_2}_{PDF}(x_2) d\sigma_P(a_1, a_2 \to \vec{y}; \vec{\alpha}) \tag{7.6}$$

The differential cross-section $d\sigma_P(p_1, p_2 \to \vec{y}; \vec{\alpha})$ is proportional to the differential cross-section for two quarks, a_1 and a_2, to produce the final state particles $\vec{y}$. The calculation uses the parton density functions for the different quarks, summed over all possible flavours and integrated over the fractions of momenta that the quarks carry from their parent proton, x_1 and x_2.

Finally the differential cross-section for two incoming quarks to produce the final state particles $\vec{y}$ is given by:

$$d\sigma_P(a_1, a_2 \to \vec{y}; \vec{\alpha}) = \frac{(2\pi)^4 |\mathcal{M}_P(a_1, a_2 \to \vec{y}; \vec{\alpha})|^2}{x_1 x_2} d\Phi_{n_f} \tag{7.7}$$

where $\mathcal{M}_P$ is the matrix element for the hard process and $d\Phi_{nf}$ gives the phase space for the number of final state particles n_f given by the four momenta $\vec{y}$.

7.3 Matrix Element Analysis

The proposal for how to make use of the Matrix Element technique in this VBF Higgs analysis is to create a new variable based on the event likelihood, this variable is the likelihood ratio:

$$LR = \frac{\mathscr{L}_{signal}}{\mathscr{L}_{background}} \tag{7.8}$$

where LR is the Likelihood Ratio, $\mathscr{L}_{signal}$ represents the likelihood that the event is of signal type and similarly $\mathscr{L}_{background}$ represents the likelihood that the event is of the background type.

Since the likelihood depends on the differential cross-section given in equation 7.5 this differential cross-section needs to be calculated for both the signal and background processes. The Matrix Element technique is particularly useful in discriminating against backgrounds found to be irreducible using kinematic cuts only, so for the purpose of this calculation let us assume the background intended to discriminate against is $Z \rightarrow \tau\tau$ + jets. Since the final state will be the same for both processes the only difference in the calculation comes from the Matrix Element.

7.3.1 Calculating the Matrix Element

It is not necessary to calculate the Matrix Element manually for this calculation; it is possible to use a Matrix Element generator, for example MadGraph [120] to produce code to calculate this Matrix Element during event generation. At the same time MadGraph also generates the value of the total cross-section for each possible subprocess, which is used for the normalisation.

7.3.2 Calculating the Signal Likelihood

To be able to perform the calculation of the signal likelihood let us begin from equation 7.5. The measured particles are two τ leptons, τ_ℓ and τ_h, and two jets, j_1 and j_2, with the measured properties $\vec{x}$ in the detector. The final state particles from the Matrix Element calculation which give rise to the measured particles are two τ leptons, τ_1 and τ_2, and two quarks, q_1 and q_2, with the properties $\vec{y}$.

The initial protons colliding are named p_1 and p_2, whereas the individual quarks which collide are labelled a_1 and a_2.

The detector response is described by a transfer function; the formula describing the total transfer function for this process incorporates a transfer function for each type of final state

particle, in this case jets and τ leptons. This formula is given as:

$$\begin{aligned} W(\vec{x},\vec{y};\vec{\beta}) &= \sum_{i=1}^{n_{comb}} \prod_{t=1}^{n_\tau} \delta^2(\vec{u}^{rec}_{\tau_{\ell,h}} - \vec{u}^{mat}_{\tau'}) W_\tau(E^{rec}_\ell / E^{mat}_{\tau'}) \times \\ & \qquad \prod_{j=1}^{n_j} \delta^2(\vec{u}^{rec}_j - \vec{u}^{mat}_{q'}) W_{jet}(E^{rec}_j, E^{mat}_{q'}, \phi^{mat}_{q'}; S_\phi) \end{aligned} \tag{7.9}$$

where the $\vec{u}$ are the unit vectors of the momentum of each particle, either reconstructed particles (rec), the τ lepton, $\tau_{\ell,h}$, or jet, j, or Matrix Element level particles (mat), the τ lepton, τ', or quark, q'. Similarly E is the energy of each of these particles; S_ϕ is the jet energy scale which is dependent on $\phi_{q'}$, the flavour of the Matrix Element level quark giving rise to the jet. The number of possible assignments of Matrix Element level particles (mat) to reconstructed particles (rec) is known as the number of combinations, n_{comb}. The transfer function given in equation 7.9 describes the assumption that the direction of the momenta of both the τ leptons and both the jets is well measured. The calculation of the form of a transfer function is described in more detail in section 7.5.

In order to continue the calculation, the differential cross-section detailed in equation 7.7 needs to be evaluated, in order to do this it is necessary to expand the density of states factor, $d\Phi_{n_f}$ for this particular final state. It is given by:

$$\begin{aligned} d\Phi_{nf} &= \delta^4(a_1 + a_2 - \tau_1 - \tau_2 - q_1 - q_2) \\ & \quad \times \frac{d^3\vec{P_{\tau_1}}}{(2\pi)^3 2E_{\tau_1}} \times \frac{d^3\vec{P_{\tau_2}}}{(2\pi)^3 2E_{\tau_2}} \times \frac{d^3\vec{P_{q_1}}}{(2\pi)^3 2E_{q_1}} \times \frac{d^3\vec{P_{q_2}}}{(2\pi)^3 2E_{q_2}} \end{aligned} \tag{7.10}$$

Since there are 6 particles involved in this interaction, each represented by a 4 momentum, there are 24 quantities needed to fully describe an event of this type. For any unknown variable it is necessary to perform a numerical integration over its values; this is time consuming and computationally intensive. Therefore it is best to simplify the solution as much as possible by introducing assumptions and constraints.

The first assumption is that the incoming quarks have no transverse component to their momentum, this removes 4 unknowns. By using the equation $E^2 = P^2 + m^2$, where the as-

sumption is that $m_{q,j} = 0$ and m_τ is 1.777 GeV one additional degree of freedom per particle is constrained. Each delta function imposes a constraint and eliminates an unknown quantity; there are 12 in total from both the $d\Phi_{nf}$ factor and the transfer function, shown in equation 7.10 and equation 7.9 respectively. This leaves only two unknown quantities; using a variable transformation these can be chosen to be any two variables, here the two variables chosen are E_{τ_1} and E_{τ_2}. Ideally a good choice is a variable which has a peaked distribution as this best enables the integration to converge when using a numerical integration package such as VEGAS [121, 122]. To summarise, the steps required to evaluate equation 7.5 are:

- Use the values of integration variables and the solutions to obtain all particle momenta
- Evaluate the Jacobian determinant for the variable transformation
- Use the MadGraph code to evaluate the Matrix Element and multiply it by f_{PDF} for each incoming quark, summing over all possible flavours
- Calculate the transfer function for each final state particle
- Repeat all of the above steps for each possible combination of quark - jet assignments in the final state

7.4 Example Results

A simplified example of the use of the variable Likelihood Ratio was carried out. Since each subprocess has a different Matrix Element and the calculation must be performed separately for each, the first simplification was to choose a process with a small number of subprocesses as an illustrative example. Here the process $pp \to Z \to \tau\tau$ was chosen due to the lack of additional permutations of quark flavour in the final state. The background process should have the same objects in the final state hence $pp \to \gamma/H \to \tau\tau$ was chosen, generated by requiring a $\tau\tau$ final state with no Z boson allowed in the intermediate state. The mass of the Higgs boson was set to 120 GeV. Since these samples are well separated in invariant mass it should demonstrate that the Matrix Element method is correctly implemented. Both samples were generated using

MadGraph at 14 TeV centre-of-mass energy.

The next simplification was that before the stage where the integration was implemented, the likelihoods for signal and background were evaluated exactly using the full momenta information for all particles from the generated events.

Therefore this simplified example in fact shows a perfect case where all particles are matched correctly to their 'reconstructed' counterparts, which are all measured perfectly.

Figure 7.3(a) shows the signal likelihood evaluated on a signal sample strongly peaking at 1 and figure 7.3(b) shows the signal likelihood evaluated on a background sample strongly peaking at 0. This illustrates the possible discrimination that can be achieved. With the inclusion of the transfer functions, simulated Monte Carlo passed through a detector simulation and the integration these peaks will become less sharp but will still be well separated and this is where the method becomes more powerful.

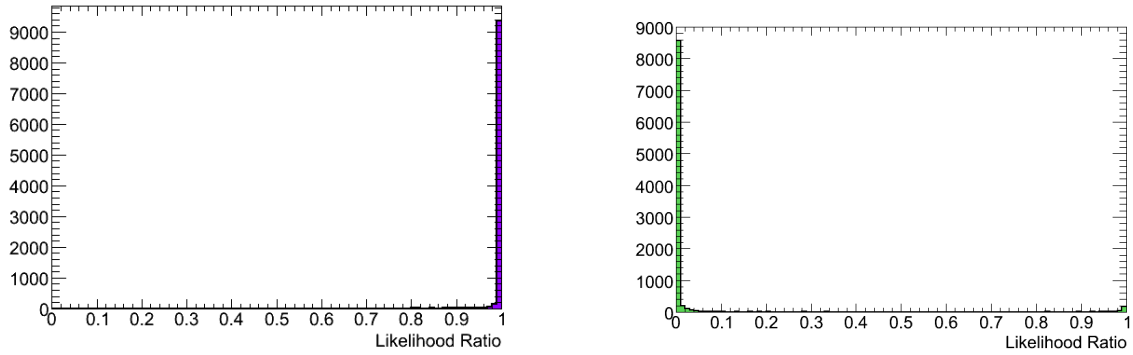

(a) (b)

Figure 7.3: Likelihood Ratio evaluated on a signal sample (a) and a background sample (b).

7.5 Transfer Functions

The transfer functions describe the probability density of the final state particles with momenta $\vec{y}$ to be reconstructed in the detector with the properties $\vec{x}$. This parametrisation speeds up and simplifies the calculation to make it manageable. The detector response is different for each type of particle observed in the detector, such as electrons, muons, τ leptons and jets.

The determination of transfer functions for jets was well described at D0 [123], so here let us discuss calculating the transfer functions for τ leptons and the associated difficulties.

The Matrix Element generators available do not contain descriptions of τ lepton decays; while it is possible to interface with TAUOLA [84] to generate samples containing decayed τ leptons it is not possible to generate the Matrix Element for them. Therefore the decay of the τ leptons and the energy carried away by the neutrinos needs to be accounted for in the transfer functions instead.

Instead of the gaussian peak one would expect for measuring the resolution of the energy measurement for the electrons or muons, an asymmetric tail is introduced as a result of including the neutrino energy. This shape can be seen from the left image in figure 7.4 and figure 7.5.

The τ transfer functions must be calculated separately for the decays to electrons, muons and one or three charged mesons to account for the different detector response to each particle. The resolution functions were shown to be dependent on the energy of τ lepton and its value of η; these dependencies are shown in figure 7.4 and figure 7.5, alongside the distribution against ϕ where no dependence is seen.

To calculate the transfer functions a sample of simulated $W \rightarrow \tau\nu$ events was used. The transfer functions are functions of ΔE, which is given by:

$$\Delta E = E_{truth} - E_{reco} \tag{7.11}$$

where E_{truth} is the energy of the truth level τ lepton before decay and E_{reco} is the reconstructed energy of the visible particle, either the lepton or the reconstructed hadronically decaying τ lepton.

Some basic preselection quality criteria were imposed, which were based on the the Benchmark analysis for $Z \rightarrow \tau\tau$ at $\sqrt{s} = 14$ TeV [124].

Truth τ leptons and all reconstructed objects were required to have $|\eta| < 2.5$ and $p_T > 10$ GeV. Reconstructed electrons had to pass “medium” selection criteria; muons were to be recon-

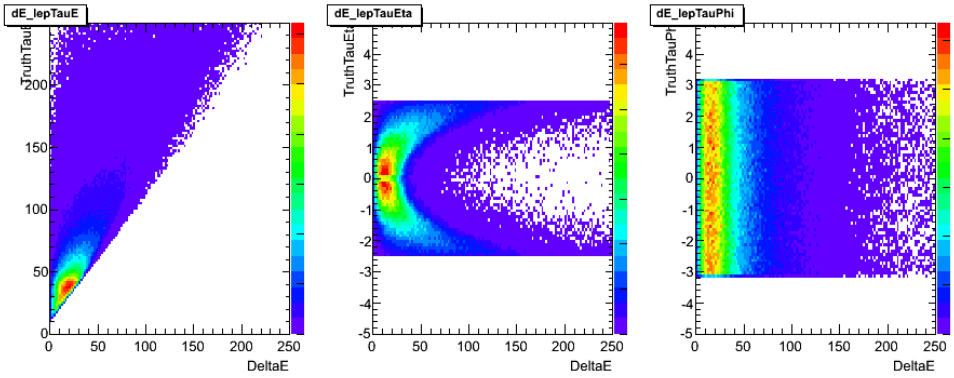

Figure 7.4: The dependence of ΔE [GeV] on E [GeV] (left), η (centre) and ϕ (right) for the case where the τ decays leptonically. The large tail extending to higher values of ΔE on the left plot is caused by the inclusion of the neutrinos in the transfer function. This dependence plus the dependence on η illustrates the need for the transfer function to be binned in E and η.

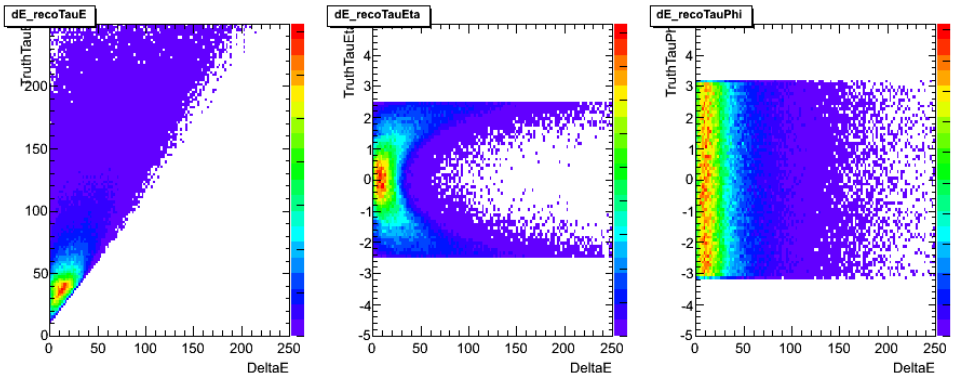

Figure 7.5: The dependence of ΔE [GeV] on E [GeV] (left), η (centre) and ϕ (right) for the case where the τ decays hadronically. The large tail extending to higher values of ΔE on the left plot is caused by the inclusion of the neutrino in the transfer function. This dependence plus the dependence on η illustrates the need for the transfer function to be binned in E and η

structed as combined, with the Muon Spectrometer track matched to an Inner Detector track and the best match selected. Hadronically decaying τ leptons were required to pass “medium” level selection cuts and the dedicated electron veto. The reconstructed object was matched within $\Delta R < 0.4$ to the truth τ lepton.

7.6 Summary and Outlook

The Vector Boson Fusion produced Higgs boson decaying to two τ leptons search channel is an important addition to those that have already been used in the early data searches at the ATLAS detector [36]. The two high-p_T jets and the lack of jet activity between them leads to a signal which can be distinguished from a multijet background.

The analysis level cuts used for this discrimination as well as those used to reject other common background were introduced as chosen for an analysis at a 10 TeV centre-of-mass energy. While they offer clear rejection (as illustrated in the full analysis proposal at 14 TeV [108]) their efficiency is low; this could be improved through the use of a multivariate method.

One of the irreducible backgrounds in this channel is the $Z \rightarrow \tau\tau$ + jets. The Matrix Element method here could prove an effective tool; convoluting the calculated Matrix Element for a process with detector resolution functions to produce a likelihood variable. This variable by its nature encapsulates all of the kinematic information about a process.

The calculation and how it could be performed in this channel was discussed. A simple example in practice was used to illustrate the power of the method in distinguishing between two different processes with the same final state. Finally the practicalities of creating the required τ detector resolution functions were detailed and examples given.

This technique could be used to increase sensitivity in this channel and the examples show that many of the tools required to perform this analysis are already available.

The possibility of developing a multivariate analysis focussed on the VBF Higgs production mode is a longer term goal. At this stage in data taking the statistics are still too low to focus on the VBF Higgs production. Since $gg \rightarrow H\tau_\ell\tau_h$ has a cross-section 10 times higher than that of $VBF\,H \rightarrow \tau_\ell\tau_h$ both modes are being studied. Currently a cuts based analysis, re-optimised for data taking at a centre-of-mass energy of 7 TeV, is being performed on the 2011 dataset.

Chapter 8

Conclusion

The theory of the Standard Model (SM) was developed during the second half of the 20^{th} century and has been highly successful at explaining the observed particle reactions. It describes all of the fundamental particles observed and the three fundamental forces which govern their interactions. An overview of this theory and an insight into its development was given; a description was also included of the Higgs mechanism, proposed to answer one of the important questions the SM has not so far answered: how the particles acquire their masses.

In the SM the masses of the massive gauge bosons are not explained, nor are the masses of the fermions. The inclusion of the Higgs mechanism in the SM generates the required masses but also a neutral Higgs boson. The Higgs boson has been searched for directly at the LEP accelerator, the Tevatron, and most recently the LHC but has not yet been observed. The current limits from these direct experimental searches mean that the mass of the Standard Model Higgs boson must be $M_H > 114.4$ GeV according to LEP [31], $M_H < 156$ or $M_H > 177$ GeV according to the Tevatron [35], and $M_H < 141$ or $M_H > 476$ GeV according to the LHC combined results [38] from the ATLAS and CMS experiments.

The ATLAS detector at the LHC, used to collect data for this thesis, is one of the two experiments at the LHC designed as a general purpose detector to search for the Higgs boson and beyond the Standard Model physics. Since the spectrum of physics aims is broad there were many different specifications and design considerations placed on the ATLAS detector. A description of the ATLAS detector and the many subsystems which constitute this large, complex piece of apparatus was given. An overview of the range of techniques used to identify each type of particle or physics object was included. The trigger designed to identify hadronically decaying τ leptons was described and an early study of performance was shown. This study

highlighted the difficulties of identifying τ objects in an environment such as the LHC, where additional activity is often present due to the high instantaneous luminosity.

Since the successful start of the data taking period at the record-breaking new high centre-of-mass energy of 7 TeV at the LHC a number of measurements of Standard Model processes have been performed. Each of these interesting measurements combine to show how well the ATLAS detector is performing and how accurately the detector operation, physics reconstruction, and identification are understood.

In this thesis the measurement of the cross-section of the $Z \rightarrow \tau_\ell \tau_h$ process was presented. This channel is particularly useful to commission many aspects of the $H \rightarrow \tau_\ell \tau_h$ analysis. The events were selected by an optimised cut-flow; the backgrounds to this process, the $Z \rightarrow \ell\ell$, $\bar{t}t$ and diboson processes were estimated using Monte Carlo and the $W \rightarrow \ell\nu$ predictions were normalised to data. For the multijet background a method to estimate this using data was developed. This method took advantage of two uncorrelated variables, the isolation requirements on the electron or muon lepton and the product of the electric charge of this lepton with the hadronically decayed τ candidate. These two variables were used to create a matrix of four exclusive regions to perform the estimation. This method was optimised, its robustness tested and a full study of the uncertainty associated with this method was performed. For the signal and each background process a study of each of the systematic uncertainties was conducted, from both theoretical and experimental sources. The cross-section was measured in two channels, one with the leptonically decaying τ lepton decaying to a muon + neutrinos and the other with it decaying to an electron + neutrinos.

Each channel was corrected for its branching ratio and the two total cross-sections that were obtained are $\sigma(Z \rightarrow \tau\tau, m_{inv}$ 66 - 116 GeV) = 857.6 $\pm$ 81.4(stat.) $\pm$ 132.5(syst.) $\pm$ 30.19(lumi.) $\pm$ 2.8(theo.) pb for the muon channel and $\sigma(Z \rightarrow \tau\tau, m_{inv}$ 66 - 116 GeV) = 1142 $\pm$ 135.5(stat.) $\pm$ 206.2(syst.) $\pm$ 40.19(lumi.) $\pm$ 3.6(theo.) pb for the electron channel, where the invariant mass of the Z boson is between 66 and 116 GeV. These measurements agree within uncertainties with the ATLAS measurement of the cross-section of the $Z \rightarrow \ell\ell$ process

(where $\ell = e, \mu$) [100] and with the CMS measurement of the $Z \to \tau\tau$ process [107].

In order to effectively search for the Higgs boson at the LHC and to study its properties if it is found, the ATLAS experiment aims to use as many channels as possible. Some channels are more suited to earlier searches than others due to their higher sensitivity, this is illustrated by the inclusion of only six channels in one of the early released exclusion limits by the ATLAS collaboration [33]. As the LHC continues to operate it is important not only to include more channels but also to gain the maximum sensitivity possible in each channel. As measurements such as that of the cross-section of the $Z \to \tau_\ell \tau_h$ process confirm that the reconstruction and identification of the electrons, muons, τ leptons and E_T^{miss} is performing well and is understood it becomes possible to consider employing multivariate techniques.

The channel where the Higgs boson is produced by Vector Boson Fusion and decays to two τ leptons was discussed. A cuts-based analysis performed on Monte Carlo simulation at a centre-of-mass energy of 10 TeV served to introduce the variables currently employed to reject backgrounds for this channel and to highlight the low signal efficiency for them. The benefits of a Matrix Element analysis were discussed and a discriminating variable based on this technique was defined. An example analysis was used to illustrate that tools are already available to begin developing this analysis.

Bibliography

[1] K. Nakamura et al. Review of particle physics. *J. Phys.*, G37:075021, 2010.

[2] Q. R. Ahmad et al. Measurement of the rate of $\nu_e + d \rightarrow p + p + e^-$ interactions produced by B-8 solar neutrinos at the Sudbury Neutrino Observatory. *Phys.Rev.Lett.*, 87:071301, 2001, nucl-ex/0106015.

[3] K. Eguchi et al. First results from KamLAND: Evidence for reactor anti- neutrino disappearance. *Phys. Rev. Lett.*, 90:021802, 2003.

[4] F. Halzen and A. D. Martin. *Quarks and Leptons: An Introductory Course in Modern Particle Physics: Chapter 1*. John Wiley & Sons, 1984.

[5] D.D. Ryutov. Using Plasma Physics to Weigh the Photon. *Plasma Phys.Control.Fusion*, 49:B429, 2007.

[6] R. K. Ellis, W. J. Stirling, and B. R. Webber. QCD and Collider Physics. *Camb.Monogr.Part.Phys.Nucl.Phys.Cosmol.*, 8:1–435, 1996.

[7] G. Arnison et al. Experimental observation of isolated large transverse energy electrons with associated missing energy at $\sqrt{s}$ = 540 GeV. *Phys. Lett.*, B122:103–116, 1983.

[8] G. Arnison et al. Experimental observation of lepton pairs of invariant mass around 95 GeV/c^2 at the CERN SPS collider. *Phys. Lett.*, B126:398–410, 1983.

[9] M. Banner et al. Observation of single isolated electrons of high transverse momentum in events with missing transverse energy at the CERN anti-p p collider. *Phys. Lett.*, B122: 476–485, 1983.

[10] P. Bagnaia et al. Evidence for $Z^0 \rightarrow e^+e^-$ at the CERN $\bar{p}p$ collider. *Phys. Lett.*, B129: 130–140, 1983.

[11] S. L. Glashow. Partial Symmetries of Weak Interactions. *Nucl.Phys.*, 22:579–588, 1961.

[12] S. Weinberg. A Model of Leptons. *Phys.Rev.Lett.*, 19:1264–1266, 1967.

[13] A. Salam. Weak and Electromagnetic Interactions. In N. Svartholm, editor, *Elementary Particle Theory*.

[14] C. Yang and R. L. Mills. Conservation of Isotopic Spin and Isotopic Gauge Invariance. *Phys.Rev.*, 96:191–195, 1954.

[15] P. W. Higgs. Broken Symmetries and the Masses of Gauge Bosons. *Phys.Rev.Lett.*, 13: 508–509, 1964.

[16] P. W. Higgs. Spontaneous Symmetry Breakdown without Massless Bosons. *Phys.Rev.*, 145:1156–1163, 1966.

[17] F. Englert and R. Brout. Broken Symmetry and the Mass of Gauge Vector Mesons. *Phys.Rev.Lett.*, 13:321–322, 1964.

[18] T. W. B. Kibble. Symmetry breaking in nonAbelian gauge theories. *Phys.Rev.*, 155: 1554–1561, 1967.

[19] G. S. Guralnik, C. R. Hagen, and T. W. B. Kibble. Global Conservation Laws and Massless Particles. *Phys. Rev. Lett.*, 13:585–587, Nov 1964.

[20] M. Gell-Mann. The interpretation of the new particles as displaced charge multiplets. *Il Nuovo Cimento (1955-1965)*, 4:848–866, 1956.

[21] Y. Nambu. Axial vector current conservation in weak interactions. *Phys.Rev.Lett.*, 4: 380–382, 1960.

[22] Y. Nambu and G. Jona-Lasinio. Dynamical Model of Elementary Particles Based on an Analogy with Superconductivity. 1. *Phys.Rev.*, 122:345–358, 1961.

[23] Y. Nambu and G. Jona-Lasinio. Dynamical Model of Elementary Particles based on an Analogy with Superconductivity. II. *Phys.Rev.*, 124:246–254, 1961.

[24] J. Goldstone. Field Theories with Superconductor Solutions. *Nuovo Cim.*, 19:154–164, 1961.

[25] J. Goldstone, A. Salam, and S. Weinberg. Broken Symmetries. *Phys.Rev.*, 127:965–970, 1962.

[26] N. Cabibbo. Unitary Symmetry and Leptonic Decays. *Phys.Rev.Lett.*, 10:531–533, 1963.

[27] M. Kobayashi and T. Maskawa. CP Violation in the Renormalizable Theory of Weak Interaction. *Prog.Theor.Phys.*, 49:652–657, 1973.

[28] S. Dittmaier et al. Handbook of LHC Higgs Cross Sections: 1. Inclusive Observables, 2011, hep-ph/1101.0593.

[29] A. Djouadi. The Anatomy of electro-weak symmetry breaking. I: The Higgs boson in the standard model. *Phys.Rept.*, 457:1–216, 2008.

[30] M. Baak et al. Updated Status of the Global Electroweak Fit and Constraints on New Physics. 2011, hep-ph/1107.0975.

[31] LEP Working Group for Higgs boson searches, ALEPH, DELPHI, L3 and OPAL Collaborations. Search for the standard model Higgs boson at LEP. *Phys.Lett.*, B565:61–75, 2003.

[32] The CDF and D0 Collaborations. Combined CDF and D0 Upper Limits on Standard Model Higgs-Boson Production with up to 6.7 fb^{-1} of Data. 2010, hep-ex/1007.4587.

[33] The ATLAS Collaboration. Limits on the production of the Standard Model Higgs Boson in pp collisions at $\sqrt{s} = 7$ TeV with the ATLAS detector. *Eur.Phys.J.*, C71:1728, 2011.

[34] The CMS Collaboration. Measurement of W+W- Production and Search for the Higgs Boson in pp Collisions at $\sqrt{s}$ = 7 TeV. *Phys.Lett.*, B699:25–47, 2011.

[35] The CDF, D0 Collaborations, the Tevatron New Phenomena, and Higgs Working Group. Combined CDF and D0 Upper Limits on Standard Model Higgs Boson Production with up to 8.6 fb^{-1} of Data. 2011, hep-ex/1107.5518.

[36] The ATLAS Collaboration. Update of the Combination of Higgs Boson Searches in pp Collisions at $\sqrt{s}$ = 7 TeV with the ATLAS Experiment at the LHC. ATLAS Conference Note: ATLAS-CONF-2011-135, Sep 2011.

[37] The CMS Collaboration. Search for standard model Higgs boson in pp collisions at $\sqrt{s}$ = 7 TeV and integrated luminosity up to 1.7 fb^{-1}. Aug 2011.

[38] The ATLAS and CMS Collaborations. Combined Standard Model Higgs Boson Searches with up to 2.3 fb^{-1} of pp Collisions at $\sqrt{s} = 7$ TeV at the LHC. ATLAS Conference Note: ATLAS-CONF-2011-157, Nov 2011.

[39] L. Evans and P. Bryant. LHC Machine. *JINST*, 3:S08001, 2008.

[40] The ALICE Collaboration. The ALICE experiment at the CERN LHC. *JINST*, 3:S08002, 2008.

[41] The ATLAS Collaboration. The ATLAS Experiment at the CERN Large Hadron Collider. *JINST*, 3:S08003, 2008.

[42] The CMS Collaboration. The CMS Experiment at the CERN LHC. *JINST*, 3:S08004, 2008.

[43] The LHCb Collaboration. The LHCb Detector at the LHC. *JINST*, 3:S08005, 2008.

[44] LHC Commissioning with Beam. http://lhc-commissioning.web.cern.ch/lhc-commissioning/ (Feb 2012).

[45] The ATLAS Collaboration. Reconstruction, Energy Calibration, and Identification of Hadronically Decaying Tau Leptons in the ATLAS detector. ATLAS Conference Note: ATLAS-CONF-2011-077, Apr 2011.

[46] B. Heinemann. ATLAS Public Luminosity Results. https://twiki.cern.ch/twiki/bin/view/AtlasPublic/LuminosityPublicResults Twiki showing pp collisions in 2010 (July 2011).

[47] The ATLAS Collaboration. Luminosity Determination in pp Collisions at $\sqrt{s} = 7$ TeV Using the ATLAS Detector at the LHC, 2011.

[48] The ATLAS Collaboration. Updated Luminosity Determination in pp Collisions at $\sqrt{s}$ = 7 TeV using the ATLAS Detector. ATLAS Note: ATLAS-CONF-2011-011, March 2011.

[49] J. Boyd, B. Heinemann and E. Torrence. Luminosity and Run Statistics Plots for 2010 Beam Data. https://twiki.cern.ch/twiki/bin/view/AtlasPublic/RunStatsPublicResults2010 Twiki showing pp collisions in 2010 (July 2011).

[50] T. LeCompte, R. Bartoldus. ATLAS Detector Status Twiki. https://twiki.cern.ch/twiki/bin/view/AtlasPublic/ApprovedPlotsATLASDetector (May 2011).

[51] Yamamoto, A. and others. The ATLAS central solenoid. *Nucl. Instrum. Meth.*, A584:5, 2008.

[52] A. Yamamoto and others. Progress in ATLAS Central Solenoid Magnet. *IEEE T. Appl. Supercond.*, 10:353, 2000.

[53] The ATLAS Collaboration. ATLAS Pixel Detector Electronics and Sensors. *JINST*, 3: P07007, 2008.

[54] Ahmad, A. and others. The silicon microstrip sensors of the ATLAS semiconductor tracker. *Nucl. Instrum. Meth.*, A578:98, 2007.

[55] The ATLAS Collaboration. The ATLAS Transition Radiation Tracker (TRT) proportional drift tube: design and performance. *JINST*, 3:P02013, 2008.

[56] The ATLAS Collaboration. Performance of Primary Vertex Reconstruction in Proton-Proton Collisions at $\sqrt{s}$ =7 TeV in the ATLAS Experiment. ATLAS Conference Note: ATLAS-CONF-2010-069, Jul 2010.

[57] S. Ask et al. The ATLAS central level-1 trigger logic and TTC system. *JINST*, 3:P08002, 2008.

[58] The ATLAS Collaboration. Expected Performance of the ATLAS Experiment: Detector, Trigger and Physics. CERN-OPEN-2008-020, 2009.

[59] W. Lampl et al. Calorimeter Clustering Algorithms : Description and Performance. ATLAS Note: ATL-LARG-PUB-2008-002, Apr 2008.

[60] M. Aharrouche et al. Supporting Document for egamma Paper: Electron Efficiency measurements using ATLAS 2010 data at $\sqrt{s}$ = 7 TeV. ATLAS Note: ATL-COM-PHYS-2011-322, Apr 2011.

[61] S. Hassini and others. A muon identification and combined reconstruction procedure for the ATLAS detector at the LHC using the (Muonboy, STACO, MuTag) reconstruction packages. *NIM*, A572:77–79, 2007.

[62] Th. Lagouri and others. A Muon Identification and Combined Reconstruction Procedure for the ATLAS Detector at the LHC at CERN. *IEEE Trans. Nucl. Sci.*, 51:3030–3033, 2004.

[63] The ATLAS Collaboration. Measurement of Inclusive Jet and Dijet Cross-sections in Proton-Proton Collisions at 7 TeV Centre-of-Mass Energy with the ATLAS Detector. *Eur. Phys. J.*, C71:1512, 2011.

[64] C. Boddy et al. Measurement of $Z \to \tau\tau$ production cross-section in proton-proton collisions at $\sqrt{s}$ = 7 TeV with the ATLAS detector. ATLAS Note: ATLAS-COM-PHYS-2011-416, May 2011.

[65] M. Cacciari and G. P. Salam. Dispelling the N^3 myth for the k_t jet-finder. *Phys.Lett.*, B641:57–61, 2006.

[66] M. Cacciari, G. P. Salam, and G. Soyez. FastJet. http://fastjet.fr/.

[67] The ATLAS Collaboration. Jet energy scale and its systematic uncertainty for jets produced in proton-proton collisions at $\sqrt{s}$ = 7 TeV and measured with the ATLAS Detector. ATLAS Conference Note: ATLAS-CONF-2010-056, Sept 2010.

[68] The ATLAS Collaboration. Performance of the missing transverse energy reconstruction and calibration in proton-proton collisions at a center-of-mass energy of 7 tev with the atlas detector, Jul 2010.

[69] The ATLAS Collaboration. Performance of the ATLAS tau trigger in pp collisions at $\sqrt{s}$ = 900 GeV. ATLAS Conference Note: ATLAS-CONF-2010-021, Jul 2010.

[70] The ATLAS Collaboration. Performance of the ATLAS tau trigger in pp collisions at $\sqrt{s}$ = 7 TeV. ATLAS Conference Note: ATLAS-CONF-2010-090, Oct 2010.

[71] S. Frixione and B. R. Webber. Matching NLO QCD computations and parton shower simulations. *JHEP*, 0206:029, 2002.

[72] K. Benslama et al. Tau identification using the TauDiscriminant package. ATLAS Note: ATL-COM-PHYS-2008-212, Nov 2008.

[73] M. Dam, P. Jez, P. Kadlecik, and S. Xella. Optimization of Tau Trigger Selection and Pileup Effects. ATLAS Note: ATL-DAQ-INT-2010-008, Jul 2010.

[74] The ATLAS Collaboration. Measurement of the $Z \to \tau\tau$ Cross Section with the ATLAS Detector. *Phys.Rev.*, D84:112006, 2011.

[75] The ATLAS Collaboration. Observation of $z \to \tau_h\tau_\ell$ decays with the atlas detector. ATLAS Conference Note: ATLAS-CONF-2011-010, Feb 2011.

[76] M. Baak et al. Data Quality Status Flags and Good Run Lists for Physics Analysis in ATLAS. ATLAS Note: ATL-COM-GEN-2009-015, Mar 2009.

[77] https://atlas-datasummary.cern.ch/lumicalc.

[78] The ATLAS Collaboration. Updated Luminosity Determination in pp Collisions at $\sqrt{s}$ =7 TeV using the ATLAS Detector. ATLAS Conference Note: ATLAS-CONF-2011-011, Mar 2011.

[79] The ATLAS Collaboration. Charged particle multiplicities in pp interactions at $\sqrt{s}$ = 0.9 and 7 TeV in a diffractive limited phase-space measured with the ATLAS detector at the LHC and new PYTHIA6 tune. ATLAS Conference Note: ATLAS-CONF-2010-031, Jul 2010.

[80] S. Agostinelli et al. GEANT4: A simulation toolkit. *Nucl. Instrum. Meth.*, A506:250, 2003.

[81] T. Sjostrand, S. Mrenna, and P. Skands. PYTHIA 6.4 physics and manual. *JHEP*, 05: 026, 2006.

[82] S. Frixione and B. R. Webber. Matching NLO QCD computations and parton shower simulations. *JHEP*, 0206:029, 2002.

[83] G. Corcella et al. HERWIG 6.5. *JHEP*, 0101:010, 2001.

[84] S. Jadach, Z. Was, R. Decker, and J. H. Kühn. The τ Decay Library TAUOLA, Version 2.4. *Comput. Phys. Commun.*, 76:361–380, Feb 1993.

[85] P. Golonka and Z. Was. PHOTOS Monte Carlo: A Precision Tool for QED Corrections in Z and W Decays. *Eur.Phys.J.*, C45:97–107, 2006.

[86] The ATLAS Collaboration. Measurement of the $W \to l\nu$ and $Z/\gamma* \to ll$ production cross sections in proton-proton collisions at $\sqrt{s} = 7$ TeV with the ATLAS detector. *JHEP*, 1012:060, 2010.

[87] S. Catani et al. Vector boson production at hadron colliders: a fully exclusive QCD calculation at NNLO. *Phys. Rev. Lett.*, 103:082001, 2009.

[88] J. Butterworth et al. Single Boson and Diboson Production Cross Sections in pp Collisions at $\sqrt{s} = 7$ TeV. ATLAS Note: ATL-COM-PHYS-2010-695, Aug 2010.

[89] The ATLAS Collaboration. Data-Quality Requirements and Event Cleaning for Jets and Missing Transverse Energy Reconstruction with the ATLAS Detector in Proton-Proton Collisions at a Centre-of-Mass Energy of $\sqrt{s} = 7$ TeV. ATLAS Conference Note: ATLAS-CONF-2010-038, Jul 2010.

[90] T. Carli and others. Jet Cleaning and Efficiencies Rel 16. https://indico.cern.ch/getFile.py/access?contribId=1&resId=0&materialId=slides&confId=117497 Jet/E_T^{miss} performance meeting (Feb 2011).

[91] J. Keung. Jet Cleaning: Timing Cut. https://indico.cern.ch/getFile.py/access?contribId=1&resId=0&materialId=slides&confId=117502 Jet/E_T^{miss} performance meeting (Mar. 2011).

[92] The ATLAS Collaboration. Tau Reconstruction and Identification Performance in ATLAS. ATLAS Conference Note: ATLAS-CONF-2010-086, Oct 2010.

[93] R. Reece and H. H. Williams. A Selection Strategy for Z to tau tau to hadron muon with the First 100 pb^{-1} from ATLAS. ATLAS Note: ATL-COM-PHYS-2009-235, May 2009.

[94] A. Sherstnev and R. S. Thorne. Parton Distributions for LO Generators. *Eur. Phys. J.*, C55:553, 2008.

[95] C. Bertella et al. Studies of particle flow using calorimeter clusters in pp collisions at 900 GeV and 7 TeV with the ATLAS detector at the LHC. ATLAS Note: ATL-COM-PHYS-2010-440, Jun 2010.

[96] The ATLAS Collaboration. In-situ pseudo-rapidity inter-calibration to evaluate jet energy scale uncertainty and calorimeter performance in the forward region. ATLAS Conference Note: ATLAS-CONF-2010-055, Jun 2010.

[97] O. Arnaez and D. Froidevaux. Recommendations for electron efficiencies. https://twiki.cern.ch/twiki/bin/view/AtlasProtected/EfficiencyMeasurements Twiki from egamma working group (Feb 2011).

[98] The ATLAS Collaboration. Muon reconstruction efficiency in reprocessed 2010 LHC proton-proton collision data recorded with the ATLAS detector. ATLAS Conference Note: ATLAS-CONF-2011-063, Apr 2011.

[99] S. Bedikian et al. Determination of the Electron-Tau Mis-identification Probability with a Tag-and-Probe Method. ATLAS Note: ATL-COM-PHYS-2011-188, Feb 2011.

[100] The ATLAS Collaboration. A measurement of the total $W^{\pm}$ and Z/γ^* cross sections in the e and μ decay channels and of their ratios in pp collisions at $\sqrt{s}$ = 7 TeV with the ATLAS detector. ATLAS Conference Note: ATLAS-CONF-2011-041, Mar 2011.

[101] M. Aharrouche et al. $W \to e\nu$ and $Z \to ee$ cross-section measurement in proton-proton collisions at $\sqrt{s} = 7$ TeV with the ATLAS Detector. ATLAS Note: ATL-COM-PHYS-2010-701, Oct 2010.

[102] The ATLAS Collaboration. A combined measurement of the top quark pair production cross-section using dilepton and single-lepton final states. ATLAS Conference Note: ATLAS-CONF-2011-040, Mar 2011.

[103] P. M. Nadolsky et al. Implications of CTEQ global analysis for collider observables. *Phys. Rev.*, D78:013004, 2008.

[104] The H1 and ZEUS Collaborations. Combined Measurement and QCD Analysis of the Inclusive ep Scattering Cross Sections at HERA. *JHEP*, 1001:109, 2010.

[105] T. Gleisberg et al. Event generation with SHERPA 1.1. *JHEP*, 02:007, 2009.

[106] The ATLAS Collaboration. Measurement of the $W \to \ell\nu$ and $Z/\gamma^* \to \ell\ell$ Production Cross-sections in Proton-Proton Collisions at $\sqrt{s} = 7$ TeV with the ATLAS detector. *JHEP*, 1012:060, 2010.

[107] The CMS Collaboration. Measurement of the Inclusive Z Cross Section via Decays to Tau Pairs in pp Collisions at $\sqrt{s}$ = 7 TeV. *JHEP*, 1108:117, 2011.

[108] The ATLAS Collaboration. Search for the Standard Model Higgs Boson produced via Vector Boson Fusion Production Process in the Di-Tau Channels. CERN-OPEN-2008-020, 2009.

[109] A. Christov et al. Performance of the tau reconstruction algorithm with release 15.3.1.6 and MC08 data. ATLAS Note: ATL-COM-PHYS-2010-878, Oct 2010.

[110] The D0 Collaboration. A precision measurement of the mass of the top quark. *Nature*, 429:638–642, 2004.

[111] The D0 Collaboration. Helicity of the W boson in lepton + jets $t\bar{t}$ events. *Phys.Lett.*, B617:1–10, 2005.

[112] K. Kondo. Dynamical likelihood method for reconstruction of events with missing momentum. 2: Mass spectra for $2 \to 2$ processes. *J.Phys.Soc.Jap.*, 60:836–844, 1991.

[113] R. H. Dalitz and G. R. Goldstein. The Decay and polarization properties of the top quark. *Phys.Rev.*, D45:1531–1543, 1992.

[114] The CDF Collaboration. Precise measurement of the top quark mass in the lepton+jets topology at CDF II. *Phys.Rev.Lett.*, 99:182002, 2007.

[115] The CDF Collaboration. Measurement of the top quark mass with dilepton events selected using neuroevolution at CDF. *Phys.Rev.Lett.*, 102:152001, 2009.

[116] The D0 Collaboration. Precise measurement of the top quark mass from lepton+jets events at D0. *Phys.Rev.Lett.*, 101:182001, 2008.

[117] The D0 Collaboration. Observation of Single Top Quark Production. *Phys.Rev.Lett.*, 103:092001, 2009.

[118] The CDF Collaboration. Observation of Single Top Quark Production and Measurement of |Vtb| with CDF. *Phys.Rev.*, D82:112005, 2010.

[119] F. Fiedler, A. Grohsjean, P. Haefner, and P. Schieferdecker. The Matrix Element Method and its Application in Measurements of the Top Quark Mass. *Nucl.Instrum.Meth.*, A624: 203–218, 2010.

[120] J. Alwall et al. MadGraph/MadEvent V4: The New Web Generation. *JHEP*, 09:028, 2007.

[121] G. P. Lepage. A new algorithm for adaptive multidimensional integration. *Journal of Computational Physics*, 27(2):192–203, 1978.

[122] G. P. Lepage. VEGAS: An Adaptive Multidimensional Integration Program. *Cornell Preprint CLNS*, 1980.

[123] The D0 Collaboration. Measurement of the top quark mass in the lepton+jets final state with the matrix element method. *Phys.Rev.*, D74:092005, 2006.

[124] P. Bechtle et al. Benchmark Analysis for Z to tau tau to lepton hadron with the First 100 pb^{-1}. ATLAS Note: ATL-COM-PHYS-2010-105, Feb 2010.